Hardware Solutions for Quantitative Dentomaxillofacial X-ray Imaging

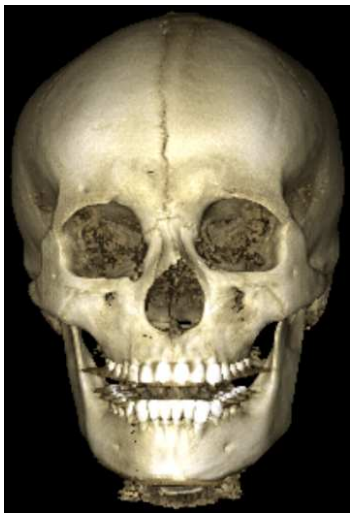

Villeseveri Somerkivi

Doctoral Thesis
Chair of Biomedical Physics
School of Natural Sciences
Technical University of Munich
2025

Technische Universität München
TUM School of Natural Sciences

Hardware Solutions for Quantitative Dentomaxillofacial X-ray Imaging

Villeseveri Somerkivi

Vollständiger Abdruck der von der TUM School of Natural Sciences der Technischen Universität München zur Erlangung eines

Doktors der Naturwissenschaften (Dr. rer. nat.)

genehmigten Dissertation.

Vorsitz: Prof. Dr. Ulrich Gerland

Prüfende der Dissertation:

1. Prof. Dr. Franz Pfeiffer
2. Prof. Dr. Jan J. Wilkens

Die Dissertation wurde am 16.10.2025 bei der Technischen Universität München eingereicht und durch die TUM School of Natural Sciences am 18.11.2025 angenommen.

Abstract

Dentomaxillofacial imaging has a long history and has advanced significantly in the past 30 years. Contributing factors have been the introduction of digital X-ray detectors, most notably flat-panel detectors. Modern dentomaxillofacial imaging offers many tools to dentists and dental surgeons in diagnostic and interventional radiology. Photon counting detectors were previously introduced in particle physics applications and have since been making their way into medical imaging, where they can also be used for spectral imaging. However, the spectral applications in dentomaxillofacial imaging have thus far been limited. While the progress in dentomaxillofacial imaging has been significant, some challenges remain. For the radiographic modalities, obtaining quantitative information regarding the underlying anatomy has not been possible so far without increasing the dose or complicating the workflow. Cone beam CT does yield quantitative information. However, especially larger objects suffer from increased levels of scattered radiation, reducing the accuracy of the observed attenuation values. In this work, we demonstrate an algorithm framework to obtain quantitative data using a prototype spectral panoramic imaging system. The results are cross-verified using a simulation framework for generating synthetic spectral panoramic images from CT and cone beam CT data. We also demonstrate using a number of phantoms that the prototype system yields consistent bone mineral density values with a reference system. In another line of work, we demonstrate how a 2D anti-scatter grid improves the stability of the attenuation signal and image contrast when fitted to a standard dental cone beam CT scanner. Although the concept was successfully demonstrated, further work is needed to establish its clinical relevance in vivo.

Zusammenfassung

Die dentomaxillofaziale Bildgebung hat eine lange Geschichte und sich in den letzten 30 Jahren erheblich weiterentwickelt. Zu den beitragenden Faktoren zählt die Einführung digitaler Röntgendetektoren, insbesondere der Flachbilddetektoren. Die moderne dentomaxillofaziale Bildgebung bietet Zahnärzten und Kieferchirurgen zahlreiche Werkzeuge in der diagnostischen und interventionellen Radiologie. Photonenzählende Detektoren wurden ursprünglich in der Teilchenphysik eingesetzt und finden inzwischen auch Anwendung in der medizinischen Bildgebung, wo sie ebenfalls für die spektrale Bildgebung genutzt werden können. Allerdings sind die spektralen Anwendungen in der dentomaxillofazialen Bildgebung bisher begrenzt. Trotz der bedeutenden Fortschritte bestehen weiterhin einige Herausforderungen. Bei radiografischen Verfahren war es bislang nicht möglich, quantitative Informationen über die zugrunde liegende Anatomie zu erhalten, ohne die Strahlendosis zu erhöhen oder den Arbeitsablauf zu verkomplizieren. Die digitale Volumentomographie (Cone Beam CT) liefert zwar quantitative Daten, jedoch leiden insbesondere größere Objekte unter erhöhter Streustrahlung, was die Aussagekraft der gemessenen Abschwächungswerte mindert. Wir stellen ein algorithmisches Framework vor, das quantitative Daten mithilfe eines spektralen Panorama-Prototyps gewinnt. Die Ergebnisse werden durch ein Simulationsframework überprüft, das synthetische spektrale Panoramaaufnahmen aus CT- und Cone Beam CT-Daten erzeugt. Zudem zeigen wir anhand mehrerer Phantome, dass das Prototypsystem konsistente Werte der Knochendichte im Vergleich zu einem Referenzsystem liefert. In einem weiteren Projekt zeigen wir, wie ein zweidimensionales Streustrahlenraster die Konsistenz der Abschwächung und den Kontrast verbessert, wenn es in einen Standard-Dental-Cone-Beam-CT-Scanner integriert wird.Obwohl das Konzept erfolgreich demonstriert wurde, sind weitere Arbeiten erforderlich, um die klinische Relevanz in vivo zu bestätigen.

Acknowledgements

This thesis would not have been realized in its current shape and form without **Thorsten Sellerer**, whom I first met in front of the overcrowded Café de la Place in Geneva, May 2019. Our collaboration slowly evolved into a full PhD from my side. Over this period, Thorsten taught me many things about spectral imaging, scientific writing, and many other things.

My supervisor, **Franz Pfeiffer**, has been important in enabling things from the university side and for his scientific experience. From the company side, **Vesa Varjonen** has done important work on enabling the co-operation and arranging resources. Additionally, I am grateful to the company's senior management for their support of this project. The company staff (especially **Ari**, **Juha**, and **Kusti**) have also been helpful in helping with the experimental work at Helsinki.

Needless to say, all of my co-authors have been vital in realizing the research and writing the papers. Additionally, this thesis has been proofread by: **Alex**, **Ari**, **Daniel**, **Touko**, and **Thorsten**.

An acknowledgement is also due for other candidates (especially **Daniel**, **Jakob**, **Johannes**, and **Kirsten**) and the staff (especially **Klaus**, **Nelly**, and **Martin**) at TUM for being helpful and friendly.

People who have not contributed directly towards my doctoral project but have had an important role in my life during the project should also be acknowledged: friends and family.

Contents

1 Introduction

Dentomaxillofacial X-ray imaging has advanced significantly in the past 30 years. In the context of extraoral imaging, digital sensors have replaced film in panoramic and cephalometric imaging, while flat panel sensors have enabled dental cone beam computed tomography (CBCT) to become common in dental clinics as well. Digitalization of the detectors has enabled, inter alia, CBCT, and digital post processing of previously film based images, such as panoramic imaging. [1, 2, 3]

Scatter and cone beam artefacts are typical image quality degrading factors in CBCT imaging. Beam hardening is an issue with all polychromatic X-ray imaging. Together, these artefacts impose challenges on some aspect of CBCT usage [4].

Panoramic imaging is a widely used imaging modality in dentomaxillofacial imaging [5]. The modality is used to obtain a low-dose radiographic overview of the teeth, mandible, and maxilla [6]. The scatter contamination is not as bad as in CBCT due to the smaller simultaneously exposed area.

Photon counting X-ray detectors were introduced in the late 80's and early '90s. The detectors were first developed at CERN for particle physics applications and have since been making their way to clinical X-ray imaging as well. The advantages over conventional (energy-integrating) detectors include the blocking of electronic noise, increased spatial resolution, and the possibility of doing spectral imaging with a single sensor layer and detector. [7]

Attempts have been made to correct scatter using radiography anti-scatter grids and software. 1D-grids offer a moderate improvement in high scatter environments but yield worse results than without the grid if the scatter signal is lower than the primary signal [8]. Monte Carlo simulation-based corrections have had some success in improving soft tissue contrast [4]. Ideally, the secondary noise introduced by scatter should also be modeled [9]. These Monte Carlo simulation-based approaches require an iterative process to solve and are, therefore, time-consuming.

In summary, quantitative information has been challenging to obtain in dentomaxillofacial imaging thus far. The principal problems could be addressed with the advancement of hardware technology in detectors and antiscatter grids. If the new hardware is able to provide quantitative information, then the subsequent question is whether this information can be used for solving clinically relevant challenges.

Panoramic imaging makes a good starting point for photon counting research in the context of dental imaging, as the active area required in panoramic imaging is small. In contrast, both the cost and technical complexity of a photon-counting flat panel detector for CBCT make this field of research challenging. To the author's knowledge, large active area photon counting flat panels are not readily available for purchase at the time of this writing.

This thesis contains the theoretical basis and the author's experimental contribution for enabling new applications in dentomaxillofacial of X-ray imaging using novel hardware. Chapter 2 contains fundamentals of X-ray physics, hardware (e.g., tubes and detectors), and related algorithms. Chapter 3 contains a short overview of the applications of dental X-ray imaging.

The experimental work of the thesis is divided as follows: Chapter 4 deals with how to do material decomposition on a panoramic system and some preliminary results. Chapter 5 describes a simulation framework for obtaining panoramic images from CT. Chapter 6 discusses obtaining bone mineral density measurements using the experimental panoramic system. Finally, Chapter 7 presents the results of a 2D tungsten grid fitted on a dental CBCT system.

2 X-ray imaging fundamentals

The purpose of this section is to provide the fundamental theoretical background of the experimental work. We start with the fundamentals of the generation of X-rays and their interaction with matter. Building on the fundamentals of physics, we then discuss X-ray detection. The next topic is a selection of phenomena observed in X-ray imaging and how they can be utilized in spectral imaging. Finally, image reconstruction is discussed.

2.1 X-ray generation

The most common way to generate X-rays is using an X-ray tube. In clinical X-ray imaging, X-rays are still primarily produced by conventional X-ray tubes, although cold emission tubes have seen some limited use [10]. An X-ray tube works by having a potential difference between the anode and the cathode (the tube voltage, kVp). Figure 1 shows a schematic of an X-ray tube. The cathode, typically in the form of a tungsten filament, has to be heated for electrons to be emitted towards the cathode in a vacuum. Bremmstrahlung (German for braking radiation) occurs when the electrons enter the electrical field of an atom of the anode. Characteristic X-rays are also generated, although less frequently than bremmstrahlung (c.f. the blue graph of Fig. 10 for an example of the spectrum).

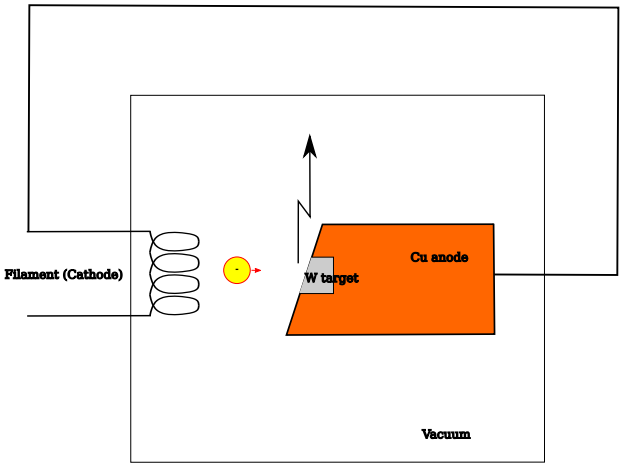

Figure 1: Simplified diagram of a conventional hot emission X-ray tube. A potential is applied in vacuum between anode and cathode. Electrons hit the tungsten target and generate X-rays. The anode can be stationary or rotating.

The bremsstrahlung radiation intensity for having a photon of energy E and electron energy T in a solid state matter (such as an X-ray tube anode) is:

$$I_{ph}(T) = \frac{\rho N}{A} \int_{T_0}^{T_E} Q \left(\frac{\mathrm{d}T}{\mathrm{d}x} \right)^{-1} \mathrm{d}T \quad , \tag{2.1}$$

where N is Avogadro's number, ρ is the density of the anode material, A is the atomic weight and Q is the differential X-ray energy intensity, and $\mathrm{d}T/\mathrm{d}x$ is the collision stopping power, which can be calculated according to the Bethe Formula [11, 12]. The integral goes from the binding energy of the electron T_0 to the photon energy $T = E$. There is no reason to continue the integral further, as

the electron would not have enough energy to produce a photon of energy E anymore. In numerical methods, the quantity Q can be approximated using a polynomial for easier calculations [11]. $\mathrm{d}T/\mathrm{d}x$ values are tabulated e.g. in the NIST ESTAR database [13].

Aside from bremsstrahlung, characteristic peaks are generally also part of the spectrum. A characteristic X-ray is emitted when a K-shell binding electron of the anode material (e.g. tungsten) is excited to vacuum potential. An upper shell electron fills the vacancy and releases the excess energy as an X-ray. This phenomenon will be discussed in more detail in the subsequent subsection.

The anode is either stationary or rotating. The cooling is applied via either air or a liquid. Anode rotation and liquid cooling enable more power to be used but add more complexity to the tube. Anode rotation allows an order of magnitude higher tube currents than in the case of a stationary anode [10] (approximately 10 vs 100 mA in CBCT context).

The thermal emission is inefficient, with roughly 1 % of the electrical current converted to X-rays and the rest to heat. Furthermore, about 99 % of the X-ray radiation is stopped in the lead shielding of the tube, as the emission is isotropic and only the radiation directed towards the region of interest can be allowed out [10]. Thus, only approximately 0.01 % of the used electrical current can be used for the imaging.

For comprehensive modeling of the X-ray attenuation in the tube, the absorption of the X-rays in the tube material, autofiltration, and the focal spot size should also be modeled. Autofiltration can modeled using eq. 2.4 in subsection 2.2.1.

To model the emission of X-ray quanta from an X-ray tube, a binomial distribution can be used:

$$P(X = k) = \binom{n}{k} p^k (1-p)^{n-k}, \tag{2.2}$$

where p is the emission probability of an individual quantum, n is the total number of interaction events, and k is the number of emitted photons, i.e., successful trials. When n approaches ∞, p approaches zero so that $np = k$, where k is greater than 0, then the Poisson distribution can be derived (see e.g. [14] for the complete derivation):

$$P(X = k; \lambda) = \frac{e^{-\lambda}\lambda^k}{k!} \quad , \tag{2.3}$$

where λ is the mean of the distribution. X-ray absorption will be discussed in the next section, but it should be pointed out that the binomial and Poisson distribution govern incident spectrum absorption at the detector (e.g. I_0 in eq. 2.4) similarly to the emission presented here.

2.2 X-ray interaction with matter

In the scope of X-ray imaging, the relevant modes of X-ray interaction with matter are the photoelectric effect, inelastic scattering, and elastic scattering. The pair production and the photonuclear effect only occur at the MeV range [15].

2.2.1 Attenuation

The Beer-Lambert law is commonly used to model X-ray attenuation in a medium. For an input spectrum $I_0(E)$, the transmitted spectrum $I(E)$ is:

$$I(E) = I_0(E) e^{-t(\mu_{\mathrm{pe}}(E) + \mu_{\mathrm{c}}(E) + \mu_{\mathrm{r}}(E))}, \tag{2.4}$$

where the μ are the energy-dependent linear attenuation coefficients (LACs), pe for photoelectric, c for Compton, and r for Rayleigh, while t is the thickness of the attenuator material. The pair

production and the photonuclear effect only occur for energies >1 MeV, i.e. they are not relevant for medical X-ray energies (approximately 20 – 140 keV). During a filtered back projection of single energy CT, eq. 2.4 is typically assumed to be independent of energy. This will be discussed in more detail in sections 2.4 and 2.5. Figure 2 shows a set of LAC plots of materials present in dental imaging. For medical X-ray energies, it is observed that the LACs are not independent of energy.

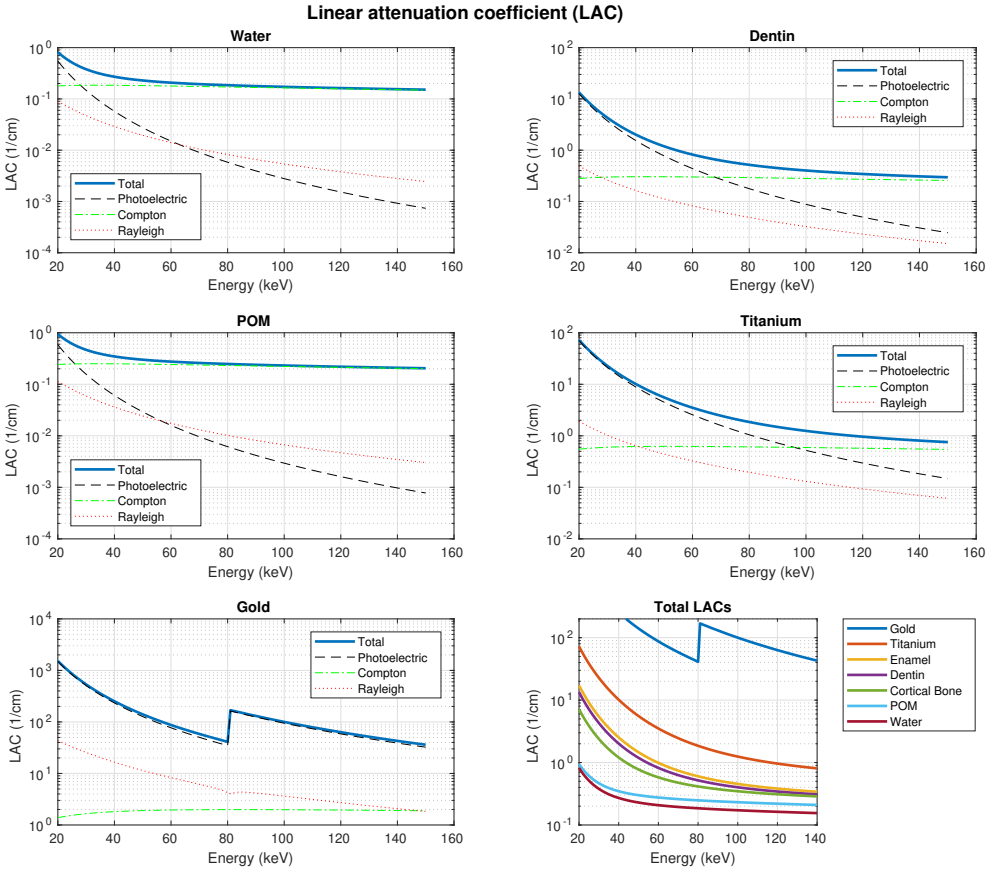

Figure 2: Linear attenuation coefficients of different materials and interaction mechanisms. The Compton component dominates for the atomic number, soft tissue like materials water and POM. For hard tissue-like materials such as dentin and titanium, the photoelectric component dominates for low energies but is gradually replaced by the Compton component. For a high atomic number, such as gold, the photoelectric component dominates the whole X-ray energy range. For gold, an increase in the attenuation at 80 keV is observable due to the K-edge. From the total linear attenuation coefficient comparison, it is observable that higher effective atomic number materials cause much higher attenuation. POM is slightly more attenuating than water due to its higher density. Both the Rayleigh and the photoelectric components decrease strongly as a function of energy, while the Compton component only decreases slightly or even increases in the low energy range.

2.2.2 Photoelectric effect

The photoelectric effect occurs when a photon is absorbed by an electron in the shell of an atom. During this process, the entire energy of the photon is transferred to the electron, resulting in its excitation and release from the shell. The electron is typically from the inner shells (K or L), as these shells have the highest probability of interacting with the photon at the X-ray energies. Thereby, the photon must have a larger energy than the binding energy of the electron to be able to free the electron. The photoelectron then typically releases the excess energy in the neighborhood. Subsequently, another electron from an upper shell falls to fill the vacancy left behind by the photoelectron. The secondary electron releases a fluorescence photon with an energy equivalent to the difference between the binding energy of origin and destination shells. The released energy can also be deposited locally via the Auger effect. [15]

The relation of the photoelectric component of the LAC follows approximately the following relation [16]:

$$\mu_{\mathrm{pe}} \propto \frac{Z^4}{E^{3.5}}, \tag{2.5}$$

where Z is the effective atomic number and E is the energy of the (X-ray) photon. This approximation yields an error $< 0.55\%$) [17]. Thus, the photoelectric effect increases strongly for heavier elements, and decreases rapidly for increasing photon energies. The reason for the sharp increase of the phototoelectic effect a function of energy is the increasing shell binding energy of the heavier elements.

Shell binding energies are presented in Fig. 3. The values are extracted from the evaluated photon data library (EPDL) 97[18]. For approximately $Z > 50$, the K-shell binding energy begins to overlap with the medical X-ray energy range. Photons having lower energy than the shell binding energy are unable to interact with the shell. This causes a sharp increase in the X-ray attenuation when the binding energy is exceeded, as discussed in more detail in section 2.2.1, cf. Fig. 2.

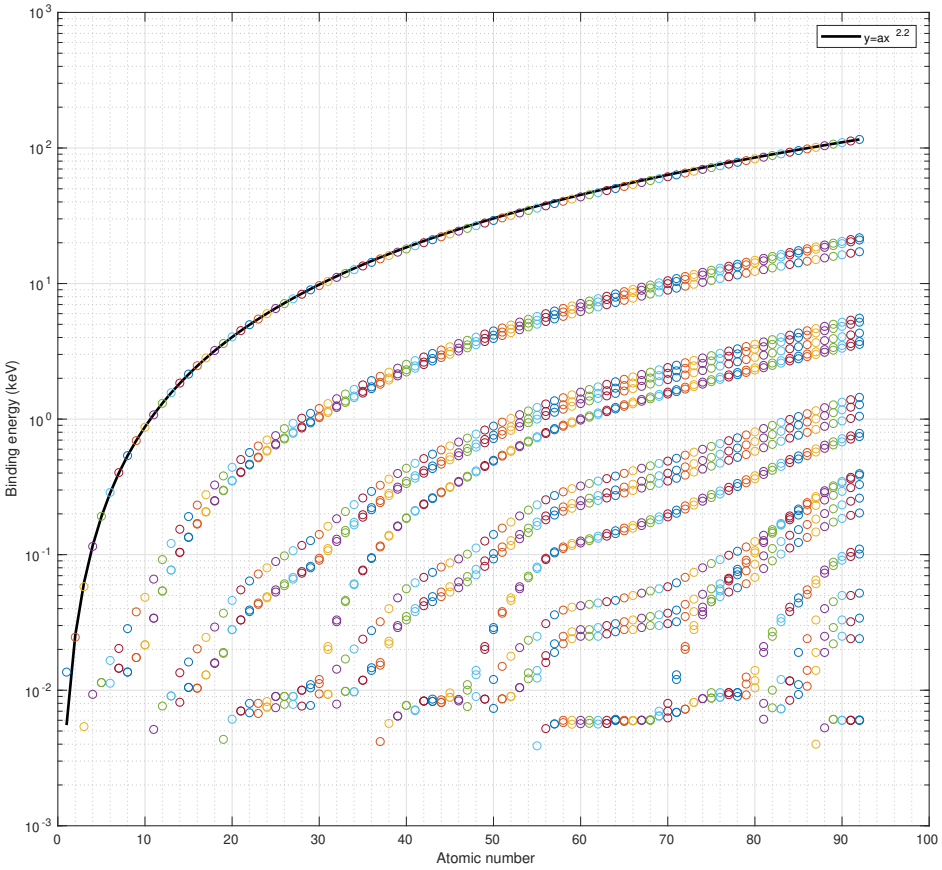

Figure 3: Shell binding energies for atomic numbers 1 – 92. A polynomial is scaled to match K-shell binding energies which is the uppermost series of circles. Shells of a single element are represented by the same circle color.

2.2.3 Inelastic (Compton) scattering

Compton scattering, also called inelastic scattering, refers to an event where a photon deposits some of its energy to an electron while continuing to exist and traveling through the material. The incident photon with the initial energy E changes its direction by an angle θ while giving some of its energy to the electron. The energy of the photon after the event is:

$$E' = \frac{E}{1 + \frac{E}{m_e c^2}(1 - \cos\theta)}\,, \tag{2.6}$$

where m_e is the mass of the electron and c is the speed of light.

The distribution of the scattering angles for a free electron in vacuum and at rest is defined by

the Klein-Nishina formula [19]:

$$\frac{\mathrm{d}\sigma_{\mathrm{KN}}}{\mathrm{d}\Omega} = \frac{r_{\mathrm{e}}^2}{2}\left(\frac{E'}{E}\right)^2\left(\frac{E'}{E} + \frac{E}{E'} - \sin^2\theta\right) \tag{2.7}$$

where r_{e} is the classical electron radius. Figure 4 shows a distribution of eq. 2.7 for different X-ray energies.

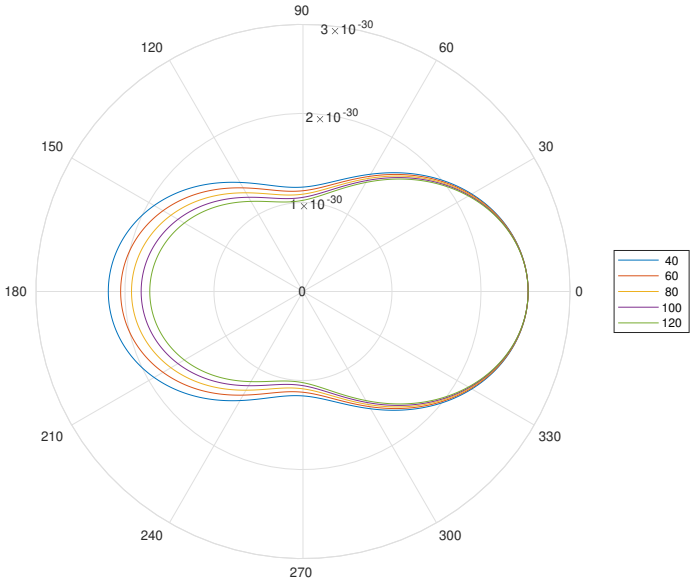

Figure 4: The Klein-Nishina differential scattering cross-section polar plots for 40 – 120 keV photons. The radial axis is the output of eq. 2.7 with the unit in m^2/sr. The angular axis is Compton angle in degrees. Note how the plot is more symmetric for lower photon energies, while higher photon energies are skewed towards forward scattering.

If the electron is not free, i.e. is part of a material, or has an initial momentum then the Klein-Nishina formula (eq. 2.7) is no longer completely valid. If the electron is bound, then Compton scattering can only occur if enough energy is deposited to free the electron. Thus, the Klein-Nishina formula is no longer accurate, especially for lower energy X-ray photons. The impact of the bound electron can be modeled with the Waller-Hartree model [20]:

$$\frac{\mathrm{d}\sigma_{\mathrm{WH}}}{\mathrm{d}\Omega} = \frac{\mathrm{d}\sigma_{\mathrm{KN}}}{\mathrm{d}\Omega} S_{WH}(q_c)\,, \tag{2.8}$$

where the momentum transfer for Compton line is given by:

$$q_c(\theta) = \frac{1}{c}\sqrt{E^2 + E'^2 - 2EE'\cos\theta}\,. \tag{2.9}$$

$S_{WH}(q_c)$ is a monotonously increasing function from $S_{WH}(0) = 0$ to $S_{WH}(\infty) = Z$ [21]. The values of q_c as a function of θ are shown in Fig. 5.

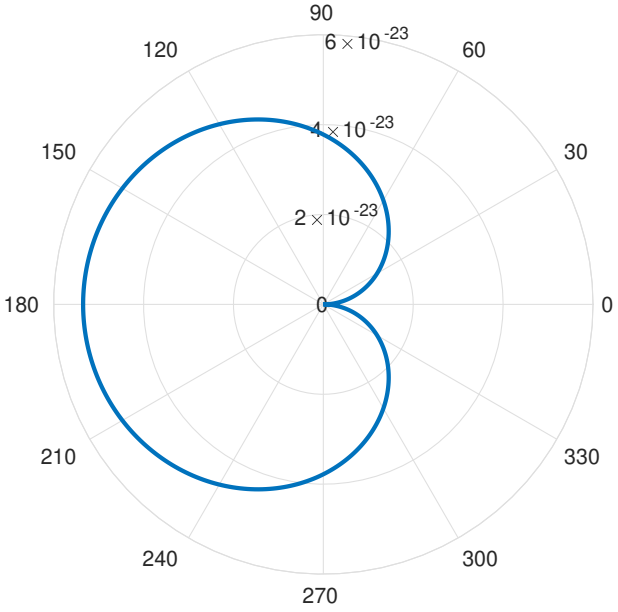

Figure 5: The momentum transfer polar plot for a 50 keV photon interacting with a bound electron. The radial axis is the output of eq. 2.9 with the unit in kgm/s. While small angles are favored in the vacuum case (Fig. 4), here large angles are favored, with small angles being close to 0. The implication is that the energy shift has to be large enough to free an electron from a shell.

If the electron has an initial momentum, this also affects the scattering distribution in the form of Doppler broadening. If there is a distribution of initial momenta, then this distribution is effectively convoluted with the Compton spectrum. There are analytical expressions to account for the Doppler broadening [22]. It should be noted however, that some popular mass attenuation tables such as the NIST XCOM [23] and the EPDL 97 [18] as well as some popular Monte Carlo simulation tools such as PENELOPE [22] have the bounding energy modeled but not the Doppler broadening.

Total cross-section can be obtained (e.g. from eq. 2.7 or 2.8) by integrating over the angle:

$$\sigma_{\text{tot}} = \int_{-2\pi}^{2\pi} \frac{\mathrm{d}\sigma}{\mathrm{d}\Omega} \mathrm{d}(\cos\theta) \quad . \tag{2.10}$$

Further, the total cross-sections (c.f. eq. 2.10) can be converted to mass-attenuation coefficients using:

$$\frac{\mu}{\rho} = \frac{\sigma_{\text{tot}}}{uA}, \tag{2.11}$$

where ρ is the mass density of the material. u is the atomic mass unit ($1.6605402 \times 10^{-24}$ g) and A is the relative atomic mass [23].

2.2.4 Elastic (Rayleigh) scattering

Elastic, or Rayleigh scattering, refers to the process where the angle of the photon is changed, but the energy remains the same. The differential cross-section for elastic scattering is:

$$\frac{\mathrm{d}\sigma_{\text{R}}}{\mathrm{d}\Omega} = \frac{\mathrm{d}\sigma_{\text{T}}}{\mathrm{d}\Omega} \left(F(q, Z)\right)^2 \quad , \tag{2.12}$$

where the Thomson cross-section is:

$$\frac{\mathrm{d}\sigma_{\mathrm{T}}}{\mathrm{d}\Omega} = r_{\mathrm{e}}^2 \frac{1+\cos^2\theta}{2} \quad . \tag{2.13}$$

Figure 6 shown the angular distribution for eq. 2.13.

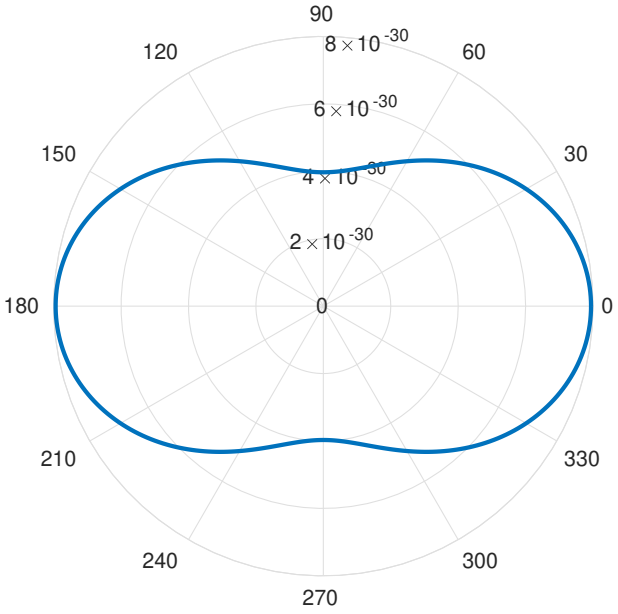

Figure 6: Thomson scattering angular distribution using eq. 2.13. The unit of the radial axis is kgm/s. The shape of the distribution resembles the Klein-Nishina plot (Fig. 4) but is symmetric.

For X-ray energies, the form of the momentum transfer q is close to zero, reducing the form factor to [22]:

$$F(0, Z) = Z \, . \tag{2.14}$$

Thus the total cross-section (using eq. 2.10) correlates approximately as:

$$\sigma_{\mathrm{R}}(E, Z) \propto \frac{Z^2}{E^2}. \tag{2.15}$$

although the correlation can vary depending on the energy range [22]. It should be noted that the elastic scattering is always dependent on the material and cannot be considered in a vacuum case like inelastic scattering can.

Eq. 2.12 is accurate only when the $E \gg$ the K-shell binding energy. If this condition is not satisfied, an additional correction term called the anomalous scattering factor needs to be introduced to accurately model the abrupt changes in the form factor around the electron shells [18].

2.3 X-ray detection

Modern X-ray detectors can be classified according to their signal formation and electronic processing. Direct conversion detectors convert incoming photons directly into electrical charge. Indirect conversion detectors use scintillators to convert the arriving X-ray photons to lower energy photons,

e.g., visible light, and then detect the visible light by converting visible light photons into electrical charge, i.e., electron-hole pairs. Photon-counting electronics are able to process each detected photon individually. In contrast, energy-integrating electronics output the total sum of deposited charge within one integration (readout) cycle.

Indirect conversion, energy-integrating detectors have been the primary detectors in clinical X-ray imaging in recent decades. This configuration is relatively easy to manufacture and robust to operate [24]. Large area digital flat panels became commercially available in the late 90's [25].

In the indirect conversion process, the X-rays are absorbed by an electrically insulating (i.e., a material with a large band gap) and optically transparent or translucent material. The charges are converted to optical photons by an activation center, which is an impurity creating a recombination center within the band gap of the insulator. This recombination center enables the emission of secondary optical (typically visible) light photons. Depending on the type of the insulator, the charge can be dominated by either free charge carriers or excitons. A schematic example is shown in Fig. 7 (a).

Important properties of scintillators include light yield, decay time, afterglow, microstructure, self-absorption. Light yield (unit, e.g., photons/keV) indicates how much light per unit of deposited energy is released. The decay time is the exponential time constant of the signal decay in the scintillation. The decay time ranges from ns to ms for typical scintillators in medical imaging. There are scintillators having an afterglow of seconds to minutes in other applications [26]. Afterglow means the residual remaining signal after the proper signal decay, which is typically caused by charge carriers being released from deep traps [26]. The microstructure can be, for example, granular, in which case the scintillator can be called a screen, structured (e.g., columnar), or garnet. Self-absorption limits the overall efficiency of the detector and imposes a maximum limit to the scintillator thickness (e.g. $<$1 cm) [27].

Some of the more commonly used scintillators include CsI:Tl, $CdWO_4$, and Gs_2S_2O:Ce (Gadox), with ":" indicating the activator element. CsI:Tl has a high light yield and can be directly deposited on top of a photodiode. The direction deposition can be used to obtain a columnar structure in the scintillator. The columnar structure causes total internal reflection for some of the photons that would have traveled a considerable distance laterally. Less light spreading enables better spatial resolution, making the scintillator suitable for CBCT [28]. Gadox, on the other hand, has a short decay time [26], making the scintillator suitable for high frame rate applications, such as helical CT.

The light photons emitted by a scintillator need to be detected and converted into electrical charge. This process is handled by a photodetector, which is usually silicon, either in an amorphous, thin film, or monocrystalline form arranged in a pixel matrix. Hydrogenated amorphous silicon, active matrix thin film transistor (a-Si:H AMATFT) is an example of an amorphous silicon detector. a-Si:H AMATFT enables cheap manufacturing of large active area flat panels combined with CsI:Tl scintillator. The purpose of hydrogen in amorphous silicon is to prevent the recombination of charge carriers through the many crystal defects. The downside is that a-Si:H AMATFTs suffer from image lag, which is the equivalent of afterglow in the photodetector. The impact of lag in modern flat panels on the reconstructed image quality is small [4], but can have a significant image quality impact in certain conditions of medical imaging. Crystalline CMOS (complementary metal oxide silicon) is another type of photodetector. The upsides of the CMOS photodetectors are that they are fast and have low noise. On the other hand, scaling CMOS for large areas is not as straightforward as with amorphous silicon and is mainly connected to costly process steps. Additionally, depending on the application, avalanche photodiodes (APD), single-photon APDs (SPAD), and photoconductors can be used for optical photon detection. It should be noted that SPADs are photon counting rather than energy integrating. [29]

Energy-integrating detectors are able to accurately measure high photon fluxes. It has to be

ensured that the digital part is not saturated. However, energy-integrating detectors start to fall off with tiny radiation signals when the noise of the detector is equal to or greater than the accumulated signal. [30]

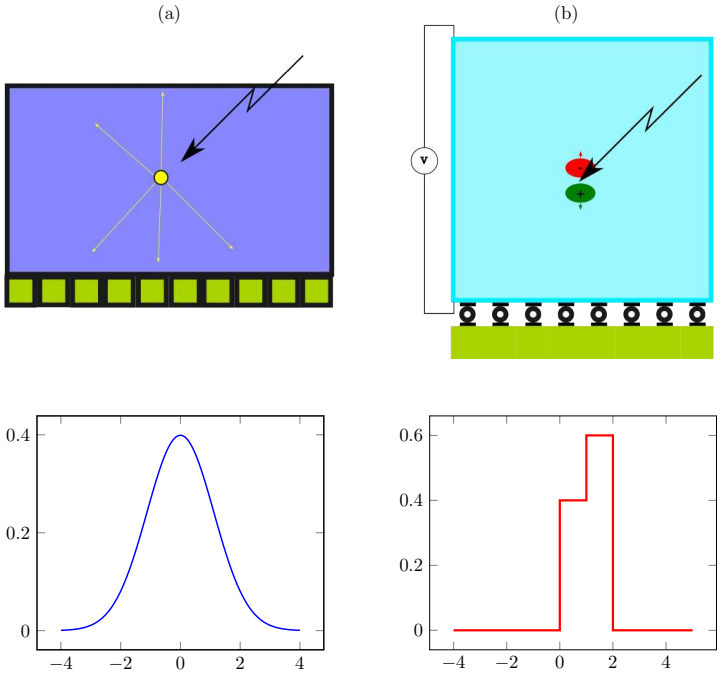

Figure 7: Top Row: Indirect (a) and direct conversion (b) detection schemes. An incoming X-ray is first converted to optical photons in a thicker scintillator on top. The optical light photons reaching the pixels of the bottom photodetector layer are converted into an electrical signal. In direct conversion, a semiconductor, usually having a high Z, absorbs an incoming X-ray photon, creating electron-hole pairs. The applied bias (v) causes, in this case, the holes to travel through the pixelated anode and the electrons toward the cathode. Holes generate a signal in the underlying electronics after traveling through the bump bonds (black). **Bottom Row:** Induced signal in each detection scheme. In thicker scintillators, light could traverse considerably before reaching a pixel. On the other hand, the electrical charge is not spread out as much in direct conversion. Note that the plots are for illustrative purposes, i.e., are not simulations or measurements.

Photon counting, direct conversion detectors (PCDs) typically utilize a semiconductor detector layer to convert arriving X-rays directly into electrical charge. PCDs are making their way to clinical X-ray imaging [31, 32, 33, 34]. PCDs are typically realized in hybridized detector design, meaning the sensor layer and the electronics are made out of two different materials and bump bonded together to form a detector. An example is shown in Fig. 7 (b).

A simplified block diagram of photon counting, direct conversion analog electronics is shown in Fig. 8. Input charges of different sizes can be measured if the application-specific integrated circuit (ASIC) has more than one discriminator per pixel, enabling single-acquisition spectral imaging.

Having a small pixelated anode with regard to the height of the detector (as in Fig. 7) means that the input charge will resemble a Dirac impulse (small pixel effect). The preamplifier will convert this Dirac impulse to a voltage step. The pulse shaper will then convert this voltage to a semi-gaussian current, which will be compared against a reference current in a discriminator. If the shaper's output current exceeds the reference current, the counter will be incremented by one. [35]

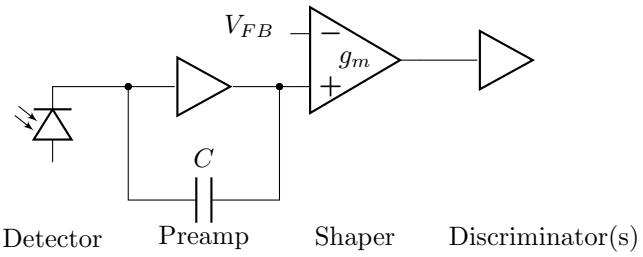

Figure 8: Simplified block diagram of photon counting electronics using Medipix-like notations: C for preamplifier feedback capacitance, g_m for gain mode, and V_{FB} for shaper feedback voltage [36].

There are several forms of non-idealities in the signal formation process. These non-idealities cause degradation of the detector's spectral response. The non-idealities can be divided into phenomena taking place in the sensor layer and the ASIC response.

In the sensor layer, charge trapping, charge sharing, and X-ray fluorescence are prominent non-idealities:

Electrical charge is sometimes trapped in the impurities of the semiconductor. The trapping causes some charge of the signal to be lost and can also interfere with future signals. The trapping can be short or long term, depending on the type of the trap. Long-term charge-trapping can lead to detector polarization. Polarization typically refers to the accumulation of charge filling the deep acceptor levers within the bandgap. Polarization is observed typically in Schottky-type CdTe detectors (i.e., where one of the metallization layers forms a diode with the semiconductor) as one charge carrier injection is limited [37, 38]. In the case of Schottky CdTe, holes are gradually released by deep acceptor levels. The hole vacancies start to nullify the bias within the detector. The perturbed electric field yields inferior change transport and energy resolution. Polarization can be reversed by resetting the bias [39]. Alternatively, ohmic contacts can be used, which makes the polarization slower. On the other hand, ohmic CdTe sensors have higher leakage current.

Charge sharing is caused by the expanding charge cloud spreading over multiple pixels. Both diffusion and Coulomb repulsion contribute to the charge cloud spreading. The initial charge cloud size is around 10 µm [40] after the photoelectron has given away most of its energy in the neighborhood. The charge transport in the direction of the x-axis within the time interval Δt can be calculated as a sum of charge carrier drift along the electric field and diffusion:

$$\Delta x = \Delta x_{\text{drift}} + \Delta x_{\text{diffusion}}, \tag{2.16}$$

which are respectively calculated as:

$$\Delta x = \mu_{cg} E_x \Delta t + \sqrt{6 D \Delta t}, \tag{2.17}$$

where μ_{cg} is the charge carrier mobility, E is the electric field, and D is the diffusion coefficient [41]. Y and z components can be calculated accordingly.

The probability of charge trapping within a time interval can be calculated using

$$P = 1 - e^{\Delta t/\tau_{\text{trapping}}} \tag{2.18}$$

where τ is the trapping time [42, 40].

X-ray fluorescence refers to the emission of a secondary photon after being absorbed by K-shell is especially harmful in high-Z semiconductors (such as CdTe) having a small pixel size. Photoelectric interaction is dominating energy transfer in CdTe for medical X-ray energies. K-fluorescence happens with 88 % probability in the case of photoelectric absorption in CdTe. The mean free paths of Cd and Te K_α-fluorescence X-rays are 110 µm and 60 µm, respectively. The mean free path of Te K_α X-ray (27.47 keV) is lower since it is above the Cd K-edge of 23.17 keV [18]. It is possible that the fluorescence ray originating from the Te shell is absorbed by the K-shell of Cd and then emitted again. It is possible that the fluorescence X-ray escapes the detector or travels to another pixel, in which case the energy information and count information are corrupted.

Photon-counting electronics are subject to non-idealities as well. Notably, the non-idealities include pulse pile-up and ballistic deficit, both associated with the preamplifier dead time, and threshold instability.

In the case of small pixels, the preamplifier processes incoming Dirac-like impulses from the detector (c.f. Fig. 8). The time it takes the preamplifier to process one charge is called dead time. If another charge arrives before the dead time has elapsed, pulse pile-up occurs. This means that the tail of the previous signal is summed with the next signal, and together, they appear as a partial sum of the signals which worsens the energy resolution. The dead time for modern ASIC is the range of tens to hundreds to nanoseconds. Considering that the corresponding pixel sizes are in the range of 50-500 µm, the maximum count rates are in the range of tens to hundreds of Mcps/mm^2 (million counts per second). [7]

The photon counting ASIC photon flux response can be modeled using either paralyzable or non-paralyazable model. The paralyzable model is:

$$R_{\text{obs}} = R_{\text{true}} \cdot e^{-R_{\text{true}} \cdot \tau}, \tag{2.19}$$

where R_{obs} is the observed count rate, R_{true} is actual incident flux and τ is dead time. This model is normally observed in the electronics unless special measures are taken to prevent the paralysis. As the flux increases, there is a maximum observed count rate, after which the count rate starts to decrease again as the analog signal remains more and more over the threshold. [27]

The non-paralyazable model is:

$$R_{\text{obs}} = \frac{R_{\text{true}}}{1 + R_{\text{true}} \cdot \tau}. \tag{2.20}$$

In this case, the detector is always ready to be triggered again after the dead time has elapsed. [27]

The dead time can be adjusted in many ASICs. For example, in Medipix ASICs the dead time can be adjusted by using the preamplifier feedback capacitance [35]. However, if signal integration time (proportional to dead time) is too low, a ballistic deficit will occur. A ballistic deficit means that part of the signal is omitted from the integration process, again resulting in a worse energy resolution.

While pile-up limits the maximum flux that photon counting detectors are able to resolve, the detectors have no minimum limit of detectability. This is in contrast to energy-integrating detectors, where the situation is reversed, as discussed earlier. [30]

Special ASIC designs can be used to reduce the effect of charge sharing and X-ray fluorescence in high-Z, small-pitch sensors. The most common scheme is analog charge summing [43, 7]. This

works by comparing the preamplifier signal of neighboring pixels and summing the signal back to one pixel if more than one preamplifiers see a signal within a short time interval. On the other hand, such features increase the dead time as the effective pixel size, and thus, the photon flux increases as the physical pixel size remains the same. Furthermore, the electronics require additional time to reconstruct the signal. Attempts have been made to minimize the increased dead time by introducing a faster shaper for the signal reconstruction node, as opposed to the individual pixels [44].

Direct conversion, energy integrating detectors have seen use in dental panoramic and cephalometric imaging sensors [45] and mammography [46]. This combination enables high a DQE and MTF while only requiring simple read-out electronics. This combination offers excellent image quality [47] with a relatively easy-to-manufacture solution.

Indirect conversion, photon counting detectors have only been used in research setups. The scintillator is required to be really fast to avoid ballistic deficit in the electronics, and the problem of light dispersion remains. However, the pulse shape is intrinsically Gaussian (as opposed to a Dirac impulse from a direct conversion detector), meaning that a pulse shaper is not required for such a detector [48].

2.4 Spectral X-ray imaging basics

The core principle of identifying the materials in X-ray attenuation is that there are at least two different spectra detected. This can be achieved using a detector (c.f. subsection 2.3), or by exposing the same detector to different spectra. The LACs of materials are energy-dependent and different materials have different rates of change, as discussed in Fig. 2.

There are five main approaches to realize spectral X-ray imaging:

1. Dual source, dual detector
2. Single source with rapid kVp switching, single detector
3. Single source, spectral detector (either multiple layers of scintillators with independent read-outs or photon counting sensor with multiple thresholds)
4. Single source with a split filter, single detector
5. Single source, single detector, two sequential scans

According to a helical dual-energy CT review article by HW Goo and JM Goo [49], the 1st approach offers the best spectral resolution, with the 2nd yielding 35%, the 3rd 22-45%, and the 5th 70% (data not available for the 4th) of normalized CNR with matched dose. Regarding temporal resolution, the 2nd and the 3rd approaches introduce a little time difference between high and low energy data. The 1st approach has a temporal offset of less than 100 ms, while the 4th approach has an offset of less than 300 ms. For the 5th approach, the offset depends on the scan time but is likely the highest. Comparing the spectral resolution of a photon counting system against dual-energy CT (DECT) is not straightforward, as the energy resolution depends on several factors, including the pixel size and electronics, as explained in the previous section. System complexity and cost are additional factors. For example, a dual source, dual detector system is more complex to manufacture and synchronization is more challenging than in a single source, single detector system. However, a quantitative comparison is not easy, since vendors don't typically publish the pricing information.

2.4.1 Basis material approximation

It can be demonstrated that using any two low Z materials (named a and b here) as basis materials, other low Z materials can be expressed as a linear combination of the two basis materials in the clinical X-ray energy range [50], allowing a small error. This yields:

$$\mu(E) \simeq t_{\mathrm{a}}\mu_{\mathrm{a}}(E) + t_{\mathrm{b}}\mu_{\mathrm{b}}(E) \; . \tag{2.21}$$

The combination of basis material thicknesses best representing the material to be represented is optimized as in [51]. If the basis materials are assumed to be polyoxymethylene (POM) and titanium, and the errors are calculated for typical materials present in the dentomaxillofacial region: cancellous bone, cortical bone, enamel, and dentin. The elemental compositions for the bony structures are from [52], while enamel and dentin compositions are from [53]. The LACs can then be calculated with the help of [23]. The errors are shown in Fig. 9.

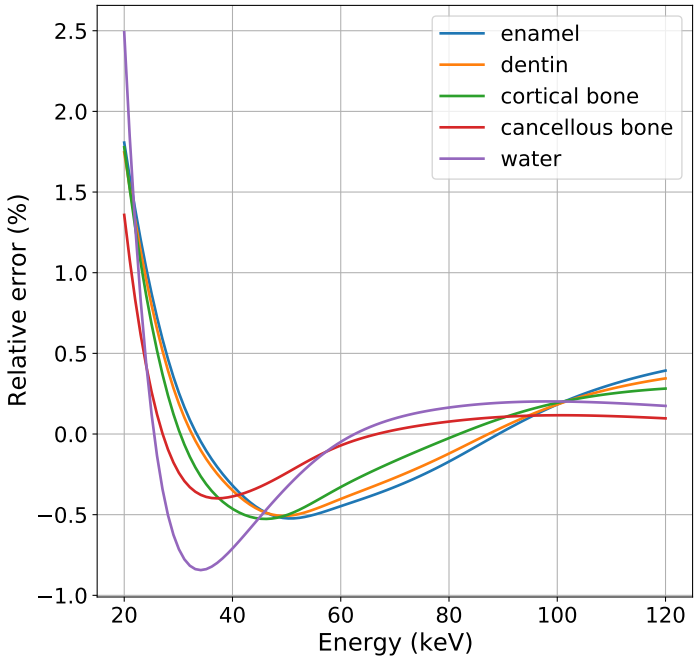

Figure 9: Errors of the basis material approximation assuming Ti and POM as basis materials for selected dental materials in the clinical X-ray energy range.

In case the K-edge of the material is within the energy range of the effective source spectrum (c.f. Fig. 2), then eq. 2.21 requires an additional term, which usually is the case for elements $Z >$ 40 whose K-edge binding energy exceeds 20 keV. In the clinical context, high Z materials could be present in the form of contrast agents such as iodine or metal implants.

2.4.2 Beam hardening

Equation 2.4 and Fig. 2 demonstrated that X-ray attenuation in a medium is energy dependent. If the input radiation is monoenergetic, the energy dependence is not an issue, and the attention will be linear. However, X-ray tubes are not monoenergetic, primarily due to bremsstrahlung. For the

most part, low-energy photons will be attenuated more than high-energy photons. Figure 10 shows a 100 kVp (spectrum generated using [11]) spectrum with 0.5 mm Cu filter before and after 15 cm water and 1 cm cortical bone (LACs from [23]).

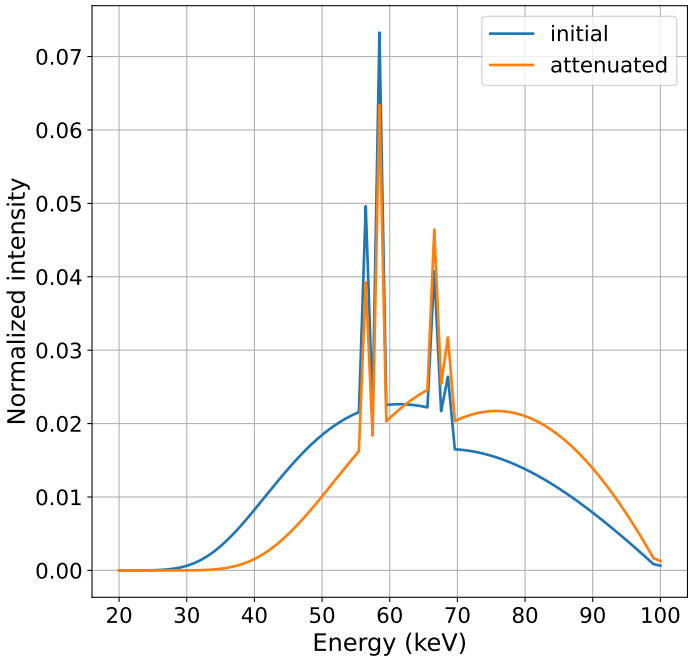

Figure 10: Spectrum shape change after an attenuation of 15 cm of water and 1 cm cortical bone, i.e., after a human head. Plots have been normalized to have a sum of 1. 2.7 % of the radiation is transmitted. The detector was not taken into account.

In the example case shown in Fig. 10, the effective energy goes from 64 to 70 keV. For this energy change, the LAC of cortical bone decreases by 5.6 % and water by 2.2 %, i.e., the attenuation is not linear. This can be especially harmful in CT, as uncorrected beam hardening leads to cupping and streaking. The artifacts can be mitigated if the non-linearity is corrected [54], although scatter correction might also be required, depending on the field of view [4].

2.4.3 Parameter estimation

An estimator is a method for estimating a single or a set of unknown parameters (usually named θ of a population based on a random sample of observations $\vec{y}$). In the context of X-ray imaging, a simple example is given by finding the line-integral length of material A in (c.f. eq. 2.4) using the transmission measurement y and the flatfield measurement b for pixel p:

$$A_p = -\ln\left(\frac{y_p}{b_p}\right) , \tag{2.22}$$

assuming a single energy measurement of a single material with $\mu = 1$.

If the problem is more complex and the result cannot be directly calculated, i.e., a closed-form solution does not exist, then a maximum likelihood estimation (MLE) can be conducted. MLE requires the probability density function of the observations and their dependency on the unknown

parameters, e.g., a forward model of the detected number of photons as a function of the line-integral length. The likelihood function $\boldsymbol{L}$ is maximized to find a set of parameters that are most probable given the forward model $\lambda(A)$ and observed data:

$$A_{opt} = \arg\max\{\boldsymbol{L}\lambda(A)\} \quad . \tag{2.23}$$

For example, in the case of Poisson distribution, the likelihood function becomes:

$$\boldsymbol{L}(\lambda(A); \vec{y}) = \prod_{i=1}^{n} \frac{\lambda(A)^{y_i}}{y_i!} e^{-\lambda(A)} \ . \tag{2.24}$$

The function is evaluated for different values of $\lambda(A)$ to find the value of A providing the highest likelihood given observed values of y_i. In this case, there would be several transmission measurements i of the same object in the same pixel. Poisson distribution is observed, e.g., in photon counting X-ray detectors. Computationally, it is more efficient to calculate the negative log-likelihood, which still will have the minimum at the same place as the maxima of the likelihood function:

$$\mathcal{L}(\lambda(A); y) = \sum_{i=1}^{n} [y_i \ln(\lambda(A)) - \lambda(A) - \ln(y_i!)] \quad . \tag{2.25}$$

Alternatively, suppose the estimated parameters have independent measurement errors, are normally distributed, and have a constant standard deviation. In that case, it can be shown that a least squares fit is the same as the maximum likelihood estimate [55]:

$$A_{opt} = \arg\min \sum_{i=1}^{n} (y_i - \hat{y_i})^2 \quad , \tag{2.26}$$

where $\hat{y_i}$ is the expected value of measurement y_i. The input signal of an energy-integrating detector could be estimated using this equation, as the detection process is directly proportional to the number of secondary quanta, which for commonly used scintillators is Gaussian.

Prior information can be incorporated into the MLE using a penalty term $\boldsymbol{P}$. The strength of the penalty is controlled by r:

$$A_{opt} = \arg\min\{-\mathcal{L}(A) + r\boldsymbol{P}\} \quad . \tag{2.27}$$

This version can be understood as a Bayesian maximum a posteriori estimate. In the context of X-ray imaging, the purpose of the penalty term is typically to enforce a degree of smoothness into an image, assuming that there are correlations in the anatomy across the neighboring pixels or voxels. Examples of the penalty include the linear Huber smoothness:

$$\boldsymbol{P}(A) = \sum_{i=1}^{n} \sum_{k=1}^{K} (x_i - x_k), \tag{2.28}$$

and the quadratic total variation [56]:

$$\boldsymbol{P}(A) = \sqrt{\sum_{i=1}^{n} \sum_{k=1}^{K} (x_i - x_k)^2}, \tag{2.29}$$

where i is the pixel or voxel index and K is the number of neighboring pixels or voxels. For example, 2D image pixel has 4 direct neighbors, while a 3D volume voxel has 6. It is possible to

introduce a minimum cutoff to these calculations, i.e., that differences below the minimum threshold are not counted towards the sum, in order to avoid over-smoothing.

In the context of probability theory, Jensen's inequality for convex functions, such as the exponential ($\theta(y) = e^y$), is:

$$\boldsymbol{E}\left[\theta(y)\right] \geq \theta(\boldsymbol{E}[y]) \quad , \tag{2.30}$$

where $\boldsymbol{E}$ marks the expected value [57]. It is desirable for the negative log-likelihood (e.g. eq. 2.25) to be convex. Depending on the function being minimized, there might be some local minima despite the function being generally convex. The calibration of the spectral forward models with real-world data is such a case. The calibration will be discussed in detail in the first experimental chapters. Even if the estimator is unbiased for noiseless and low noise inputs (equality in eq. 2.30), bias appears (inequality in eq. 2.30) at some higher noise level. In X-ray imaging, this means that MLE overestimates the line-integrals [58] at low photon statistics. In spectral X-ray imaging, two material decomposition, one basis material is overestimated while the other is underestimated [59] at low photon statistics.

2.4.4 Material decomposition

Material decomposition aims to use two or more spectral measurements to obtain information on the material(s) being measured. The attenuation coefficient is a function of energy (c.f. eq. 2.4). One interpretation is that the amount of different beam hardening is different at different energies. Generally speaking, higher atomic number elements have higher photoelectric cross sections, which decrease faster as a function of energy (compare plots in Fig. 2). Thus, the difference in beam hardening will be greater.

Material decomposition can be carried out directly for the projection data or the reconstructed images. Theoretically, projection domain decomposition correctly accounts for beam hardening, while this relationship is more complex for image domain decomposition. This work focuses on projection domain decomposition with the exception of simplified monoenergetic image domain decomposition presented in later sections.

Projection domain decomposition attempts to model the X-ray spectrum to predict the spectral change as a function of the input spectrum and the attenuator materials. The model can either attempt to explicitly model the input spectrum and the spectral response of the detector(s) or use a surrogate function to indirectly model the attenuation.

The first paper on DECT imaging was published by Alvarez and Macovski [60] in 1976, only three years after Hounsfield introduced CT [61]. DECT became commercially popular around the turn of the millennium [62]. Schlomka and coworkers at Philips introduced the first photon counting CT (PCCT) in 2008 [63] with a projection domain decomposition algorithm. The first in vivo human images were acquired using a Siemens system in 2016 [31]. Assuming two basis materials A_1 and A_2, the expectation value of observed counts using the Schlomka model for bin k is:

$$\lambda_k(A_1, A_2) = \sum_{E=1}^{\infty} I(E)D(E)S_k(E)e^{-A_1\mu_1(E)-A_2\mu_2(E)}, \tag{2.31}$$

where $I(E)$, $D(E)$, and $S_k(E)$ are the input spectrum, detector absorption efficiency, and the bin spectral response as functions of energy, respectively. The experimental calibration utilizes bin sweeps of different monoenergetic sources (e.g. at a synchrotron). The number of free parameters is reduced by assuming Gaussian photo, fluorescence, and escape peaks with a continuous background.

The Schlomka parameterized model has some drawbacks. The model requires a monoenergetic source for calibration. Such a source might not be readily available in laboratories. Furthermore, the model is numerically heavy to evaluate. These problems can be mitigated by using a surrogate spectrum for decomposition. The surrogate spectrum approach does not try to model the spectrum or the spectral response directly; instead, this approach uses a small number of elementary functions to model the non-linear relation of increasing attention of one or more materials against the observed number of counts.

Examples of surrogate spectrum forward models include the polynomial and the polychromatic Beer-Lambert models. The polynomial model is discussed in more detail in section 4. The polychromatic Beer-Lambert model is:

$$\hat{y}_i(A_{i1}, A_{i2}) = \sum_{f=1}^{F} B_{fi}\exp(-G_{fi}\left(A_{i1}f_1(E) + A_{i2}f_2(E)\right)), \tag{2.32}$$

where $\hat{y}_i$ is the observed number of counts for pixel i, B_{fi} and G_{fi} are f:th fit parameters, and $f(E)$ are the energy dependent attenuation functions [64]. F is in the range of 2-4 (1 would be equal to normal flatfield correction) i.e. $\ll$ than the kVp (80-150 in CT) in e.q. 2.31.

The spectrum can also estimated directly through transmission measurements using the maximum likelihood, expectation-maximization algorithm [65, 66].

A more advanced version of the Schlomka parameterized model has also been introduced [67]. This version incorporates an analytic Fourier model to incorporate pulse pileup into the forward model.

2.5 Image reconstruction basics

This subsection is based on the book [41] unless otherwise stated.

A function can be called a *good function* if the function is differentiable everywhere for an arbitrary number of times and all of its derivatives go to zero faster than $|x|^{-N}$ when $x \to \pm\infty$. The Gaussian function is an example of a good function. A *fairly good function* has the same properties, except the latter condition is only true for some, but not all N. All polynomials are fairly good functions.

The 1D Dirac delta function $\delta(r)$, where r is a scalar value, e.g. the magnitude of an nD vector, is a function that is defined everywhere but non-zero only at the origin. Now, consider rotating 2D vector $\mathbf{r}$ with a unit vector $\hat{\mathbf{n}}$. In this case, the function $\delta(\mathbf{r}\cdot\hat{\mathbf{n}})$ is nonzero for as long as scalar product is $\mathbf{r}\cdot\hat{\mathbf{n}} = 0$. An offset p can be applied to move the nonzero values away from the origin: $\delta(\mathbf{r}\cdot\hat{\mathbf{n}} - p)$ perpendicularly to $\hat{\mathbf{n}}$. To obtain the line mass of a function $f(\mathbf{r})$ from an angle ϕ using rotated Cartesian coordinates (x', y') :

$$\lambda(p,\phi) = \int_0^\infty d^2r f(\mathbf{r})\delta(\mathbf{r}\cdot\hat{\mathbf{n}} - p) = \int_{-\infty}^{\infty} dx' \int_{-\infty}^{\infty} dy' f_{rot}\left(x'y'\right)\delta\left(x' - p\right) = \int_{-\infty}^{\infty} dy' f_{rot}\left(p, y'\right), \tag{2.33}$$

where $f_{rot}\left(x', y'\right)$ is a Cartesian presentation of $\mathbf{r}$ with the x' being parallel to $\hat{\mathbf{n}}$ such that $\mathbf{r}\cdot\hat{\mathbf{n}} = x'$.

This is known as the **Radon transformation** and can be used to obtain a 1D projection (p) in angle ϕ from a 2D function (image) $f(\mathbf{r})$. The function $f(\mathbf{r})$ should be assumed to be good to for mathematical well-behavadness. It should be noted here that the simplified case of parallel beam geometry is assumed for simplicity. The same core principle applies to real-world cases such as CBCT [68], and helical CT [69]. The Radon transformation is the starting point of the reconstruction. The radon transform can be expressed in the the operator form as:

$$\lambda(p,\phi) = \boldsymbol{\mathcal{R}}_2(f(\boldsymbol{r})). \tag{2.34}$$

If one were to take the the 1D Fourier transform of a 1D projection (i.e. the output of e.q. 2.33) is:

$$\begin{aligned}\Lambda(\nu,\phi) = \left[\mathcal{F}_1\lambda(p,\phi)\right](\nu) = \int_{-\infty}^{\infty} dp \exp(-2\pi i\nu p) \int_0^{\infty} d^2r f(\mathbf{r})\delta(p-\mathbf{r}\cdot\hat{\mathbf{n}}) \\ = \int_0^{\infty} d^2r f(\mathbf{r}) \int_{-\infty}^{\infty} dp \exp(-2\pi i\nu p)\delta(p-\mathbf{r}\cdot\hat{\mathbf{n}}) = \int_0^{\infty} d^2r f(\mathbf{r}) \exp(-2\pi i\mathbf{r}\cdot\hat{\mathbf{n}}\nu).\end{aligned} \tag{2.35}$$

The final integral is equivalent to the 2D Fourier transform (of the original object), but with the vector $\hat{\mathbf{n}}\nu$ replacing the spatial frequency ρ. In the operator form, this can be summed as

$$\boldsymbol{\mathcal{F}}_2 = \boldsymbol{\mathcal{F}}_1\boldsymbol{\mathcal{R}}_2. \tag{2.36}$$

This is also known as the **Fourier slice theorem**, or central slice theorem. E.q. 2.36 states that taking a two-dimensional Fourier transform of the function $f(\boldsymbol{r})$ is equivalent to first taking the two-dimensional radon transform and then the one-dimensional Fourier transform.

The inverse 2D dimensional Radon transform can be obtained from eq. 2.36 to get:

$$\boldsymbol{\mathcal{R}}_2^{-1} = \boldsymbol{\mathcal{F}}_2^{-1}\boldsymbol{\mathcal{F}}_1. \tag{2.37}$$

This equation enables one to obtain the original object from transmission measurements (i.e., to reconstruct the object by **backprojecting** the projections). As per [41]: "the 1D Fourier transform of the projection $\lambda(p,\phi)$ is equal to the 2D transform of the original function $f(\mathbf{r})$ evaluated along a line through the origin of the Fourier plane." Backprojecting at different angles yields lines passing through the origin at different angles in the 2D Fourier space. As the lines always pass through the origin, the lower frequencies will be more densely sampled than the higher frequencies. Carrying the backprojection as such will result in a blurry image [14]. To more correctly reconstruct the original object, a filter in the frequency domain (e.g., $|\nu|$) needs to be applied. When working with noisy data, it should be noted that the noise is present on all frequencies, but the anatomically relevant information is mainly on the lower frequencies. Thus, in real-world applications, the filter might balance the sharpness and noise properties.

To cover the whole function $\mathcal{F}_2^{-1}$, the integral shall be over ν and ϕ. It is desirable to express the integral over $0 \leq \phi < \pi$ and $-\infty \leq \nu < \infty$, as this enables the reconstruction to be carried out using half of a rotation rather than a full rotation. This requires $d^2\rho = |\nu|d\nu d\phi$ as the area element must be positive. With the filter applied, e.q. 2.37 can be unrolled to:

$$\begin{aligned}\left[\mathcal{F}_2^{-1}\mathcal{F}_1\boldsymbol{\lambda}\right](\mathbf{r}) &= \int_0^{\pi} d\phi \int_{-\infty}^{\infty} |\nu| d\nu \exp(2\pi i\mathbf{r}\cdot\hat{\mathbf{n}}\nu) \int_{-\infty}^{\infty} dp\lambda(p,\phi)\exp(-2\pi i\nu p) \\ &= \int_0^{\pi} d\phi \int_{-\infty}^{\infty} d\nu \exp(2\pi i\mathbf{r}\cdot\hat{\mathbf{n}}\nu)|\nu|\Lambda(\nu,\phi),\end{aligned} \tag{2.38}$$

which is also called the **filtered backprojection**.

Nyquist sampling criterion can be applied to the filtered backprojection. If applied in the form of projections to pixels, an approximate limit is:

$$N_{proj} > \frac{\pi}{2}N_{pix}, \tag{2.39}$$

where N_{proj} is the total number of projections used for the reconstruction and N_{pix} is the number of detector pixels in the direction of the scanning movement. A lesser number of projections will lead to aliasing artifacts [70].

2.6 X-ray rejection (anti-scatter) grids

Scatter contamination is a well-known problem in medical X-ray imaging, especially if the detector has a large two-dimensional active area, such as CBCT. Scatter artefacts include loss of contrast, HU-value inconstancy, and cupping [4].

Both hardware and software-based scatter corrections exist. Hardware correction has been traditionally implemented in the form of 1D- radiography grids (grid pitch in 10^{-5} m range) and larger 2D-grids for helical CT (grid pitch in 10^{-3} m range. 1D here refers to the lamella only being in one direction, with a filler material in between. Software-based corrections should ideally correct for the secondary Poisson noise introduced by the scattered radiation, which is not straightforward, as the subtraction of the scatter signal affects the variance of the input frames [9].

Previously, 2D-grid manufacturing has been realized by semiconductor processing, e.g., by etching holes to a silicon wafer, casting the holes with lead, and removing the silicon [71, 72, 73]. Such an approach has been adequate for the modular detector systems of helical CTs, but the manufacturing process, i.e., the size of the wafer, puts an upper limit on the grid size. Additionally, this approach yields a geometric efficiency of 50 to 80 % [74]. 1D-grids only compensate for the lost primary signal when the scatter-to-primary ratio exceeds 1 [8]. This number is even larger for some geometries and lower kVps.

Due to recent advancements in additive manufacturing, especially tungsten powder laser sintering (also called laser powder bed fusion) being able to produce wall thicknesses in the 10^{-4} m range, 2D-grids with similar pitches to the semiconductor processed 2D grids (grid pitch 10^{-3} m) [75] have become available at larger areas (up to 20x20 cm^2). The relative density of the walls has been reported to be close to unity [76]. As this is a self-supporting structure, no filler material is required, unlike in the 1D grids.

3 Applications of dentomaxillofacial X-ray imaging

Dentomaxillofacial X-ray imaging is a common imaging modality used in hospitals and dental practices. The clinical frequency of dental X-ray images is several times higher than the clinical frequency of CT examinations worldwide [5].

Dentomaxillofacial X-ray imaging consists of dentomaxillofacial radiography and cone beam computed tomography (CBCT). Dentomaxillofacial radiography is further divided into intraoral and extraoral (panoramic) radiography.

3.1 Intraoral radiography

Intraoral radiography is used when a very high-resolution image of a small area is desired. The X-ray detector is placed inside the patient's mouth in intraoral radiography, as the name suggests. Intraoral imaging was done historically with film and nowadays using a photostimulable phosphor plate or a digital sensor.

There are three main techniques of capturing an intraoral X-ray image: parallel, bisecting, and bitewing. The technique is chosen based on the patient's anatomy and the indication for imaging [77].

In the parallel technique, the detector is placed parallel to the long axis of the teeth (c.f. Fig. 11 (a)). The parallel technique is used when a view of both the pulps and the crowns of one or a few adjacent teeth is desired [77]. The technique is used when a high-resolution view of the periapical region of a single tooth is desired or when planning dental procedures such as a bridge or implant [77].

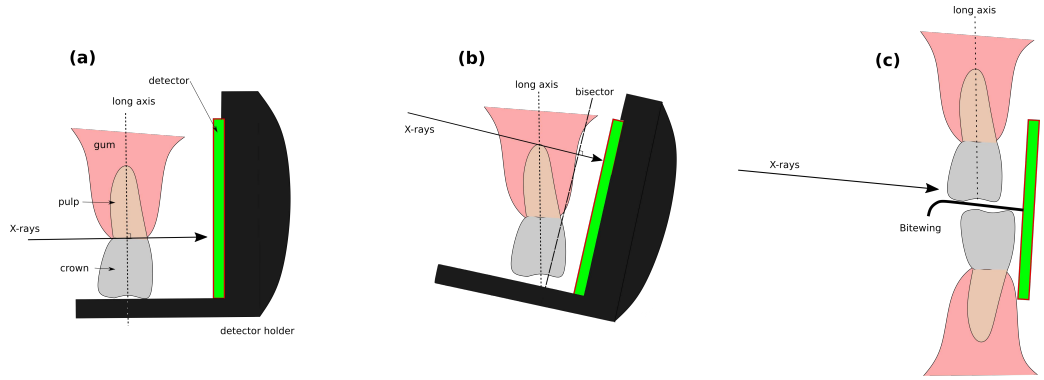

Figure 11: The parallel (a), bisecting (b), and bitewing techniques. The arrows indicate the X-ray direction, but the whole detector is typically exposed.

The patient's mouth might be cramped in a way that makes using the parallel technique impossible. In this case, the bisecting technique is used instead (Fig. 11 (b)). In the bisecting technique, the X-ray detector is positioned as close as possible to the tooth, and an imaginary line bisects the angle formed by the long axis of the tooth and the plane of the detector [77]. The X-ray beam travels perpendicular to this bisector.

The bitewing technique is used to capture the crowns of upper and lower teeth in a single image. It provides a clear view of the contact areas between adjacent teeth, making it valuable for assessing the interdental area for changes, such as caries (cavities). (Fig. 11 (c)). In this technique, the X-ray detector is placed between the upper and lower teeth so that it covers the crowns of both arches.

3.2 Panoramic radiography

Panoramic radiography (also called orthopantomograph) is a low-dose [78], entry-level examination and provides an overview of the dental arch, i.e., the crowns, pulps, gum, mandible, and maxilla. Similarly to intraoral imaging, panoramic imaging is very widely used globally [5]. Panoramic imaging displays the location of the inferior alveolar nerves and maxillary sinuses, which are relevant during many operations [79].

Figure 12 shows the panoramic principle of operation. The core principle is that the detector and the tube rotate around the patient so that the dental arch is always perpendicular to the ray path. The details of the method will be discussed further in the subsequent experimental chapters.

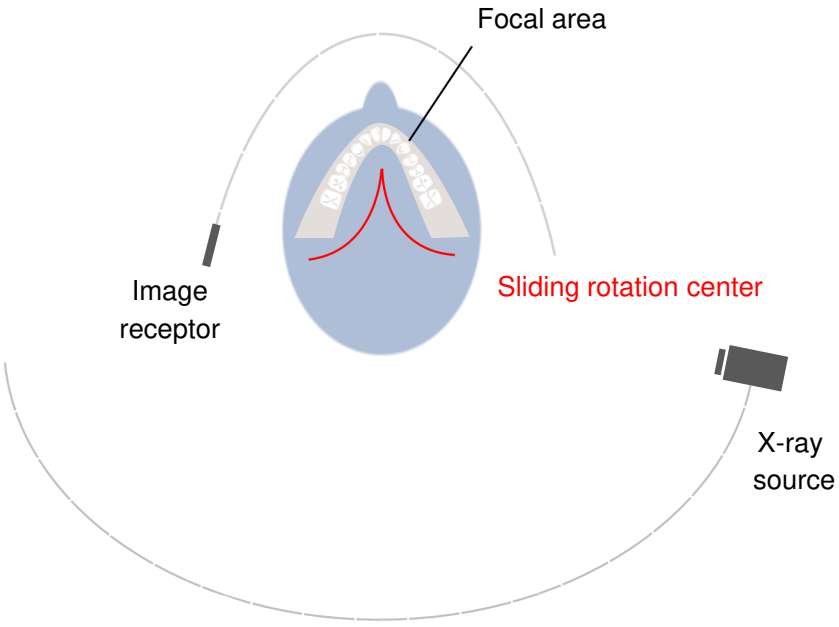

Figure 12: The working principle of panoramic imaging. Shown are the trajectories of the image receptor and the X-ray source. The position of these two decides the focal area (also called the sharp layer) and the rotation center, which in this case is sliding. The focal area aligns with the teeth. [Adapted from [80]]

The Frankfort plane is the line passing through the porion (the superior point of the external auditory meatus) and the caudal point in the bony orbita [81]. During panoramic imaging, the Frankfort plane should be horizontal [79]. The occlusal plane passes between the crowns of the teeth [79]. The occlusal plane should be tilted forward during panoramic imaging [79]. This results in a smile-like appearance for teeth, as posterior teeth appear higher with respect to the anterior teeth. The two planes are highlighted on a cephalometric X-ray image of the MIDA model [52] in Fig. 13.

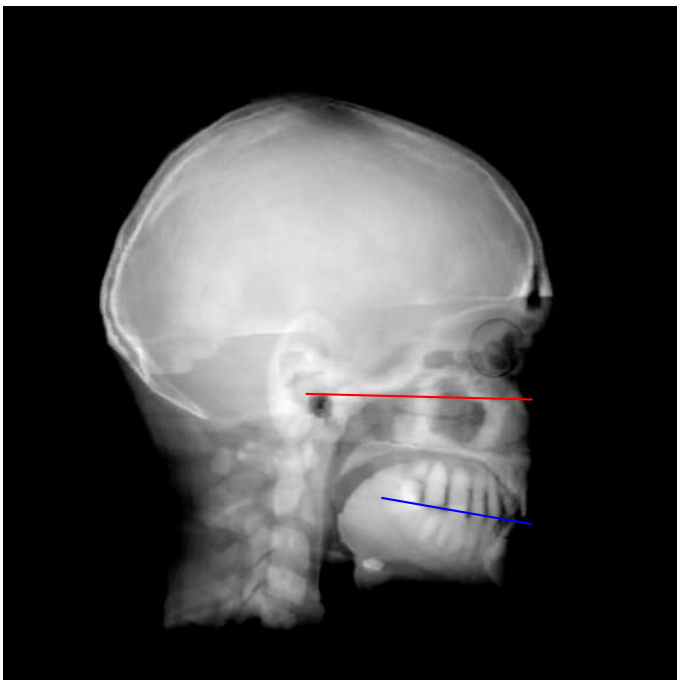

Figure 13: The Frankfort plane is highlighted using a red line. The occlusal plane is highlighted using a blue line.

Panoramic imaging systems have been reported to have a spatial resolution in the sharp layer up to 3.19 lp/mm (linepairs/millimeter) [82], while one experiment claimed as high as 5 lp/mm [83]. In contrast, CBCT systems have been reported to have a maximum resolution of 2.8 lp/mm [84]. It should be stressed that the panoramic imaging only has high resolution within a sharp layer while everything outside is blurry, while in CBCT the resolution is more constant within the imaged volume. The thickness of the sharp layer in the anterior region can range from 6 mm [79] to 17 mm [83], while the thickness in the posterior region ranges from 12 mm [79] to 44 mm [83]. Additionally, modern systems are able to computationally form multiple sharp layers and create a compound image by selecting the most relevant features from each sharp layer [85].

Panoramic imaging is sensitive to patient placement as the sharp layer is relatively small and some of the anatomical features overlap. The patient is either standing or sitting and biting a bite block. The purpose of the bite block is to ensure that the anterior teeth are at the correct position [85]. Nevertheless, positioning errors are common [79]. A study with N = 315 found that only 20% [86] are clinically excellent, e.g. have no positioning errors. Nevertheless, 70% of the images were clinically acceptable and only 10% were rejected. The rejection rates have been found to vary greatly in dental imaging (including panoramic imaging), depending on the age of patients, experience of operators, and systems themselves [87]. For studies with N $>$ 100, the rejection rates varied between 5.6 – 34% for intraoral imaging, 3.3 – 14% for extraoral radiography and 1.6 – 6.4% for CBCT [87].

The most common positioning errors are head rotations, failure to press the tongue against the palate, or not removing jewelry before the imaging [86]. The possible head rotations are shown in Fig. 14, which shows a 3D rendered bone image of an anthropomorphic head phantom (phantom in chapter 5). The 3D rendering was generated using the Planmeca Romexis software (Planmeca

Oy, Helsinki, Finland). Nodding refers to moving the chin upwards or downwards, rolling, moving the head sideways, and tilting, moving the top of the head to one side while the bottom side moves towards the other side [79].

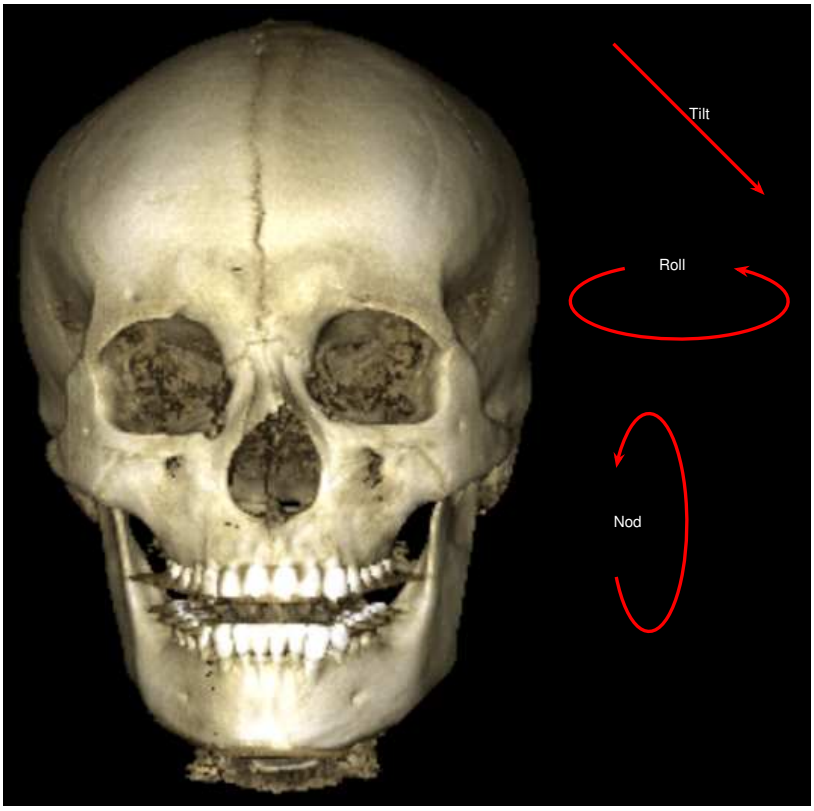

Figure 14: Positioning errors during panoramic imaging.

3.3 Cone beam computed tomography

CBCT became widely available around the turn of the millennium when amorphous silicon flat panel detectors became commercially available [88]. In dentomaxillofacial imaging, an affordable and low floor space requiring imaging system with high resolution is desirable [88]. The working principle is shown in fig. 15. For most applications, a single rotation around the patient is sufficient. In a CBCT exposure, there typically is no movement perpendicular to the axial plane, as opposed to spiral CT [89].

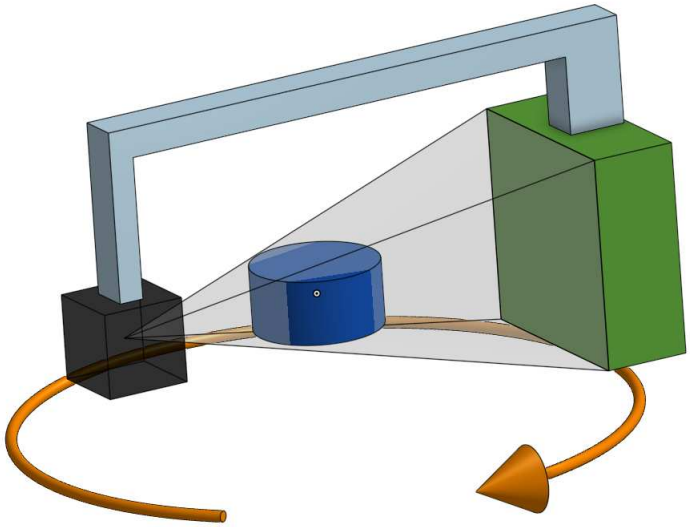

Figure 15: CBCT imaging principle. The tube (black cube) and the detector (green rectangular cuboid) rotate around an object (blue cylinder). X-ray beam (gray transparent pyramid) passes through the object.

A CBCT system with a large field of view (FOV) is subject to a considerable amount of scatter [8]. The scatter to primary can exceed 1 [8]. Scatter degrades HU value accuracy as well as the contrast-to-noise ratio and blurs the spatial resolution. In most cases, this not an issue, as in dentomaxillofacial imaging a high resolution image of the bony tissue is the most crucial [88].

CBCT is used, when a superimposed radiographic view of the dentomaxillofacial area is not sufficient [1]. Such cases are, e.g., surgical planning and follow-up for oral and maxillofacial operations, orthodontic treatment planning, airway and sinus assessment, and periodontal disease detection [90].

Before a surgical operation can start, the bone structure and volume, sinus and nerve canal locations, and the alveolar ridge have to be assessed. Depending on the anatomy, radiography might not be sufficient, and a CBCT image is required [3]. Airway assessment is typically required when planning an orthognathic surgery for obstructive sleep apnea [91]. In challenging endodontics cases, the pre-treatment assessment or follow-up sometimes requires CBCT [92].

CBCT is used in many cases of oral and maxillofacial surgery: in diagnosis, planning or follow-ups. CBCT is regularly used in implant and orthognathic surgery planning (c.f. Fig. 16) and follow-ups. Diagnosis of benign and malignant cysts and tumors has been found to have a greater efficacy using CBCT than with panoramic radiography. Sometimes, a 3D view of the root canals, the nerves, or the inferior alveolar (mandibular) canal is required during surgery planning to ensure that the operation can be carried out safely. Some fractures, such as vertical root fracture or complex jaw fractures are more reliably diagnosed with CBCT. [93]

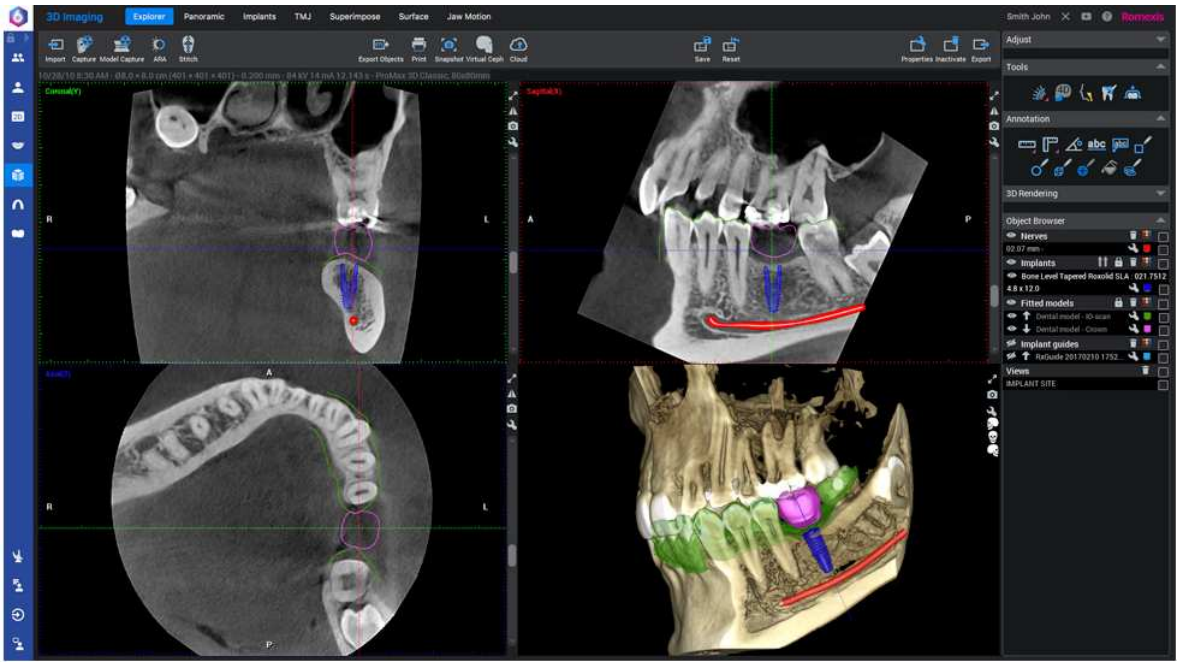

Figure 16: Implant planning in Planmeca Romexis software. Shown are the three anatomical planes of a CBCT image and a 3D render. The mandibular nerve is shown in red, the surgical guide in green, the crown of the implant in purple, and the screw in blue. Figure courtesy of Planmeca Oy, Helsinki, Finland.

In the field of orthodontics, CBCT is usually required for the diagnosis or treatment planning of impacted teeth, cleft lip or palate, and orthognathic surgery planning and follow-up [94]. Additionally, CBCT is used in the following cases if the clinician considers the benefits to outweigh the risks of obtaining a 3D image: supernumerary teeth, root resorption, evaluating alveolar boundary conditions before using temporary anchorage devices, and assessing the temporomandibular joint degeneration [94].

4 Spectral photon counting for panoramic dental imaging

In this chapter, an algorithm for realizing spectral panoramic imaging using a photon counting detector is presented. Spectral calibration and material decomposition (see chapter 2.4 and Methods within this section) are adapted for the low count environment of panoramic imaging. Specifically, the polynomial model is used as it can account for scatter contamination better than physics-based models, such as the polychromatic model. This chapter discusses the feasibility of the results primarily from a qualitative and experimental perspective.

The text and figures have been published as:

- V Somerkivi, et al. Spectral photon counting for panoramic dental imaging. Biomedical Physics & Engineering Express, vol. 9, no. 3. 2023.

Slight modifications have been made to incorporate the text and figures better into this doctoral thesis.

4.1 Introduction

Panoramic is a useful, low-dose imaging modality for dental radiography [78]. One way to generate a panoramic image is by summing partially overlapping frames together [95]. The shift from one frame to the next is determined by the movement and rotation of the imaging system. Panoramic imaging provides an overall view of the maxilla, the mandible, and the teeth while being able to show many lesions in this area [77]. Panoramic imaging has also been used for detecting caries [96], periodontitis [97], and maxillary sinusitis [98]. However, for all these conditions the intra or extra observer agreement in diagnosis is not optimal. One reason for sub-optimal diagnostic accuracy is the superimposition of soft and hard tissues in this imaging modality. This could eventually be overcome by recently developed spectral x-ray imaging approaches [99, 59, 100, 101]. These approaches have demonstrated superior diagnostic capability by employing material decomposition approaches based on spectral detection and the ability to detect features that would remain hidden in a conventional image.

One challenge, however, is that for panoramic imaging, the photon statistics for an individual frame are very low. In other words, they have a very low number of average counts per frame and thus suffer from bias. This implies that the pre-existing spectral projection domain algorithms, e.g. [102, 103, 59, 64], cannot be directly applied to panoramic imaging data, as applying these algorithms to very low photon statistics observed in panoramic imaging would introduce statistical bias [59]. The decomposition is a nonlinear operation and the noise is propagated through the decomposition, leading to an amplified noise in the output of the decomposition [104].

One way to do spectral panoramic x-ray imaging is to calculate the ratio of bins during imaging and compare that ratio to one obtained from reference phantom scan [105, 106]. However, the output of this algorithm is one unitless number i.e. not a line-integral of two or more basis materials as e.g. by an algorithm used for spectral angiography [59]. Furthermore, this algorithm does not thoroughly address the spectral responses of individual detector pixels.

In this paper, we present a first quantitative material decomposition algorithm for panoramic imaging. We show how to adapt an existing material decomposition algorithm to address the requirements of panoramic imaging. The results of the decomposition are two basis material panoramic images. The performance of this algorithm is demonstrated in an experimental setup using an anthropomorphic head phantom.

4.2 Methods

4.2.1 Material decomposition

The concept of using low-order polynomials to model line-integrals in spectral x-ray imaging was first demonstrated by Cardinal and Fenster [107]. In their work, the decomposition for two spectral measurements and materials was done by having the basis material line-integrals (A_i^0, A_i^1) for detector pixel i as a function of the low and high energy log-signals (l_i^l, l_i^h) and parameters determined in calibration ($\vec{d}_0$, $\vec{d}_1$):

$$A_i^0 = P(l_i^l, l_i^h; \vec{d}_0), \quad A_i^1 = P(l_i^l, l_i^h; \vec{d}_1). \tag{4.1}$$

This kind of formulation enables a fast and accurate decomposition in the case where there are the same number of basis materials and spectral measurements by simply evaluating these functions at the log-signals of the measurements. However, it is not possible to incorporate any kind of regularization for this closed-form solution.

If a maximum likelihood (ML) estimation is desired, then the inverted relation [59] can be used. Here, the expected number of counts $\hat{y}_i^s$ for pixel i and spectral measurement s is defined as:

$$\hat{y}_i^s = b_i^s e^{-\hat{l}_i^s}, \ \hat{l}_i^s = P_i^s(A_i; c_{is}), \ A_i = (A_i^0, ..., A_i^n)^T, \tag{4.2}$$

where b_i^s is the flatfield signal for pixel i and spectral measurement s. The polynomial model P_i^s used in this study assumes two basis materials:

$$\begin{aligned} P_i^s &= \frac{N}{D} \\ N &= c_0 + c_1 A_i^0 + c_2 A_i^1 + c_3 (A_i^0)^2 + c_4 (A_i^1)^2 + c_5 A_i^0 A_i^1 \\ D &= 1 + c_6 A_i^0 + c_7 A_i^1, \end{aligned} \tag{4.3}$$

where c (pixel and spectral measurement subscripts dropped for simplicity) are the fit coefficients.

Initially, a least-squares fit to the calibration measurements is carried out to find the fit parameters c_{is}:

$$c_{is} = \text{argmin} \sum_{k=1}^{K} w_k (l_{ik}^s - P(A_{ik}; c_{is}))^2, \tag{4.4}$$

where l_{ik}^s are linearized calibration measurements, A_{ik} are the line-integrals, and w_k the weights with k being the calibration measurement index. The weights are assigned according to the standard deviation of the corresponding calibration measurement. During calibration, the line-integrals (i.e. thicknesses) of the materials are obtained by measuring these values from the physical calibration phantom.

Following the forward model calibration (eq. 4.4), a maximum likelihood decomposition is carried out to find the combination of basis materials thicknesses A_i maximizing the likelihood given the spectral measurements. Assuming that the spectral measurements follow independent Poisson statistics, it is computationally more efficient to minimize the corresponding negative log-likelihood:

$$\mathcal{A}_i = \text{argmin} - \mathcal{L}_i(A_i) = \sum_{s=1}^{S} \hat{y}_i^s(A_i) - y_i^s \ln(\hat{y}_i^s(A_i)). \tag{4.5}$$

In eq. 4.5, the expected number of counts are a function of the basis material line-integrals. This enables maximum likelihood estimation of the line-integrals.

Generating the basis material images (eq. 4.5) leads to noise amplification and a degradation of contrast to noise ratio. Both of these problems can be remedied by denoising which takes into account the anti-correlated noise in basis material images.

The penalized log-likelihood function $\phi(\boldsymbol{A})$ is:

$$\begin{aligned}\phi(\boldsymbol{A},\tilde{\alpha}) &= -\mathcal{L}(\boldsymbol{A}) + \lambda\mathcal{R}(\boldsymbol{A},\tilde{\alpha}) \\ -\mathcal{L}(A) &= \sum_{i=1}^{N_t}\sum_{s=1}^{S} \hat{y}_i^s(A_i) - y_i^s \ln(\hat{y}_i^s(A_i)) \\ \mathcal{R}(\boldsymbol{A},\tilde{\alpha}) &= \sum_{q=1}^{N_p} ||(E_q\boldsymbol{A})\boldsymbol{\varphi}_q{}^T - \boldsymbol{D}\boldsymbol{\alpha}_q||_F^2 + v||\boldsymbol{\alpha}_q||_{\text{row}-0},\end{aligned} \tag{4.6}$$

where $-\mathcal{L}(A)$ is the sum of negative log-likelihoods over all pixels and spectral measurements. $\mathcal{R}(\boldsymbol{A})$ is the regularization term which is responsible for the denoising. q denotes patch index. Dictionary $\boldsymbol{D}$ contains a large number of small, high-quality images of typical structures of relevant anatomy. These small images in a dictionary are called atoms. The image to be denoised is divided into small patches, which are still larger than atoms. The idea is then to find a sparse linear combination $\boldsymbol{\alpha}_q$ of atoms that represent the image patch $E_q\boldsymbol{A}$ to be denoised. $\boldsymbol{\alpha}_q$ and $\boldsymbol{A}$ are each optimized in turn so that one is optimized while the other remains constant. $\boldsymbol{\varphi}_q$ is the whitening transformation matrix converting $E_q\boldsymbol{A}$ to new bases so that the noise is uncorrelated across the spectral channels. $||\ ||_F^2$ is the Frobenius norm while $||\ ||_{\text{row}-0}$ counts the number of nonzero rows. The in depth definition of all parameters and operators is in [59].

4.2.2 Panoramic imaging

In panoramic imaging the imaging system follows an elliptical trajectory around the patient so that the detector is on the front of the patient and the tube is on the back. The panoramic image is formed by summing partially overlapping frames together along this trajectory [108]. Figure 12 shows a working principle of panoramic imaging. The sharp layer typically aligns with the dental arch. Everything outside the sharp layer gets blurred while the details in the sharp layer remain visible. Additionally, it is important that one ray path crosses the dental arch only once (so that the teeth don't overlap) and that the path is roughly perpendicular to the arch. The process of generating the panoramic image is sometimes called reconstruction even though no backprojection is done, as opposed to computed tomography [77].

Post processing is typically applied after the panoramic image has been formed. Typically, the purpose of this post processing is to remove noise and adjust brightness and contrast so that more details are visible in single window level setting. [109]

4.2.3 Experimental measurement

Phantom An anthropomorphic head phantom (Erler-Zimmer GmbH, Lauf, Germany) was used in this study as seen in fig. 17. The phantom features a realistically attenuating skull, a dental bridge and a dental implant all encapsulated in plastic. These kinds of phantoms are used in dental x-ray unit production quality assurance among other things.

Experimental setup A DC-Vela photon counting detector (Varex Imaging Corporation, Salt Lake City, USA) was fitted to a Planmeca Promax Mid imaging unit (Planmeca Oy, Helsinki, Finland) as shown in fig. 17. The detector has two adjustable energy thresholds, a charge-sharing correction, a 0.75 mm thick CdTe sensor layer and a maximum frame rate of 300 fps when using two thresholds.

Table 1: Calibration Material Thicknesses. The thicknesses were chosen so that the line-integrals observed in an actual panoramic image would be densely sampled and to limit the number of pixels having line-integrals thicker than the maximum calibration thicknesses would be small.

Basis material	Thickness
POM	[0 6 8 10 12 14] cm
Ti	[0.0 1.0 2.1 3.1 4.1 6.1] mm

The dimensions of the sensor are 64 (width) pixels by 1541 (height) pixels and the detector has a pixel size of 100 µm. The adapter holding the sensor was designed so that the source-to-image distance (SID) and the imaging geometry is the same as in Planmeca's standard imaging units.

The panoramic reconstruction was carried out using Planmeca's proprietary back end software. The same back end software is used in Planmeca's commercially available units.

Acquisition Parameters

Prior to the phantom measurement, 36 calibration measurements with different thicknesses of titanium and polyoxymethylene (POM) were performed. The thicknesses are listed in table 1. Titanium and POM were chosen for basis materials as their attenuation profiles (i.e. effective atomic number and density) [18] are close to those of dentin [53] and soft tissue [23], respectively. The latter pair reflects tissue types typical to jaw and lower head.

Acquisition Parameters are shown in table 2. The dose-area product (DAP) was measured with KermaX Plus IDP 120-131 HS sensor (IBA Dosimetry GmbH, Schwarzenbruck, Germany). According to a 2019 diagnostic reference study [110], the mean DAP of 21 panoramic imaging units for adult patients was 74.1 mGy(cm)^2 with a standard deviation of 28.9 mGy(cm)^2. The DAP of 72.1 mGy(cm)^2 used in this study is very close to the mean and therefore clinically relevant. The charge-sharing correction was on for all measurements. Different tube currents were used for calibration and imaging (c.f. table 1). During calibration the detector is exposed to flatfield radiation and a higher current would induce pulse pileup in the detector application-specific integrated circuit (ASIC). Thresholds were chosen so that the low energy threshold (15 keV) captures all counts and high threshold (36 keV) has roughly half of the counts of the low threshold for the most attenuating calibration step. This was not an explicit optimization for any specific task as in [111] but it was manually found to be a working solution. The number of photon counts during calibration was of similar magnitude in this study (table 2) and a previous study [59]. However, in this study the exposure time was not increased for thick calibration measurements. The number of flatfield photon counts during imaging in this study is low (1.2×10^4). In a similar material decomposition approach [59] statistical bias starts to quickly increase below 10^3 counts, which is well below the number of flatfield counts in our study. Additionally, the use of regularization has been demonstrated to lower the bias limit [104]. However, the previous study [59] used different photon spectra and a differently sized sample, which alters the number of detected counts and affects the noise properties and the bias limit.

Table 2: Acquisition Parameters. Flatfield count values refer to the minimum number of counts per acquisition (panoramic reconstruction), as the movement speed varies. The virtual panoramic image generation for calibration data in subsection 4.2.4 explains why there is more flatfield counts in calibration than in imaging even though the tube current - exposure time product is smaller for calibration than imaging.

tube voltage	70 kVp	aluminum filtration	3.5 mm
tube current (imaging)	9 mA	thresholds	15, 36 keV
tube current (calibration)	1 mA	dose-area product	72.1 mGy(cm)^2
flatfield counts (imaging)	1.2×10^4	source to image distance	600 mm
flatfield counts (calibration)	6.5×10^6	magnification	1.4
exposure time (imaging)	18 s	frame rate	200 fps
exposure time (calibration)	25 s	field of view	6×154.1 (mm)^2
movement/frame (max)	1.2 px		

4.2.4 Material decomposition workflow in panoramic imaging

The algorithm presented in II.A takes in 2D native detector frames. However, native detector frames cannot be used to directly decompose panoramic images as described in section 4.2.2 as the native frames have different dimensions and amount of photon counts in contrast to a panoramic image. Furthermore, the photon statistics in the native frames are low. Such low statistics would introduce a significant bias in the estimation [59]. Thus, some additional steps are required to be able to get quantitative material decomposition images.

The workflow to generate spectral panoramic images is shown in fig. 18. The first step was to acquire calibration frames in the native detector size. 5000 native (64×1541) frames were acquired for each of the 25 calibration measurements. The mean of each calibration measurement is taken to suppress Poisson noise. The panoramic reconstruction in this work was done by summing 3700 partially overlapping frames. To generate a virtual panoramic image, instead of using partially overlapping individual frames, the mean frame was used as every frame. A virtual panoramic image was generated for each calibration measurement. The size of these virtual panoramic images was 3390×1541, matching the size of actual panoramic images. The calibration was then carried out for these images by fitting the polynomial coefficients according to eq. 4.4.

Panoramic images are acquired normally. These images are decomposed as any 2D image, using eq. 4.5. Regularized decomposition is done using eq. 4.6 as explained in section 4.2.1. Finally, virtual monoenergetic images are generated by multiplying the decomposition results and their respective linear attenuation coefficients and summing together these two multiplications.

4.3 Results

The accuracy of the calibration coefficients is assessed by using them to decompose a set of test points having different thicknesses of POM and titanium than those used in the calibration (c.f. table 1). The calibration coefficients were first calculated using eq. 4.4. The test points were then decomposed using eq. 4.5. The mean of each test point was taken from over the whole virtual panoramic image, excluding some bad pixels, mostly near the edges of the image. The true values versus the results of the test decomposition are shown in fig. 19. Some of the decomposition points (>0.6 cm of titanium, >14 cm of POM) in fig. 19 actually exceed the maximum thicknesses of the calibration data points in table 1. Thus, it is not feasible to expect the model to yield correct values here. For the last calibration point (14 cm POM, 6.1 mm Ti) the radiation had attenuated by a factor of 4.1×10^{-4} for bin low and 1.7×10^{-3} for bin high. During imaging the total number of counts

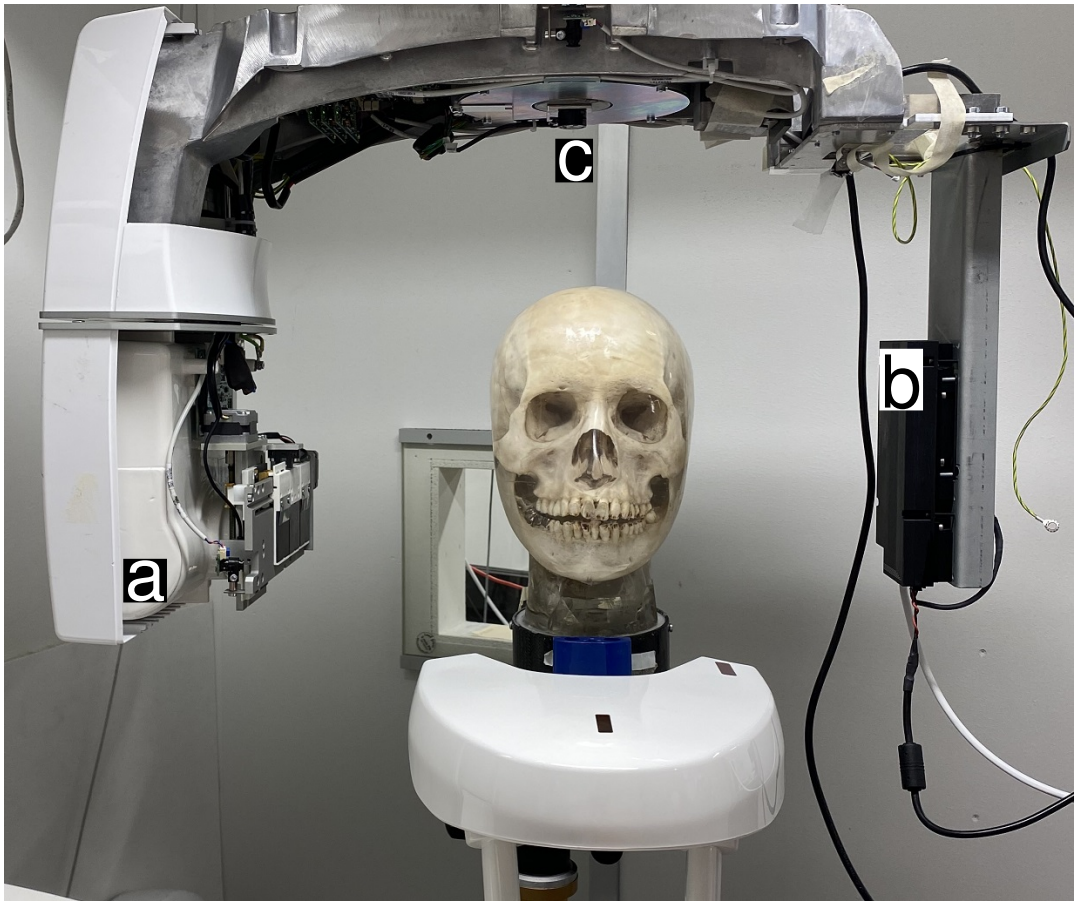

Figure 17: The experimental setup. The tube (a) is mounted on the left end of the U-arm of the unit. The detector (b) is mounted on the right end of the U-arm of the unit. The U-arm rotates around the center of rotation (c). The phantom is in the middle of the image. [Adapted from [112]]

expected for flatfield is (c.f. table 2) 1.2×10^4. Thus, only a couple of counts are expected with such attenuation. Having an attenuation which yields very small number of counts will be very noisy and suffer from rounding error due to the discrete nature of the photons. Note that this does not affect calibration test decomposition in fig. 19, as there are more flatfield counts during calibration (c.f. table 2) than during imaging.

A 2D histogram of the output of eq. 4.5 applied to the panoramic image obtained from the anthropomorphic head phantom is shown in fig. 20. The histogram has 101 bins in each direction. A Gaussian filtering with a sigma of 2 was applied to the histogram in order to the make the prominent features clearer. The test calibration points with indices from 7-9, 13-15 and 19-21 (c.f. fig. 19) span the region of the line-integral values the decomposition of the head phantom yields. In other words, the accuracy of these 9 points is relevant for the sample studied and the reliability of the decomposition of the head phantom. The maximum absolute error for this set of test decomposition

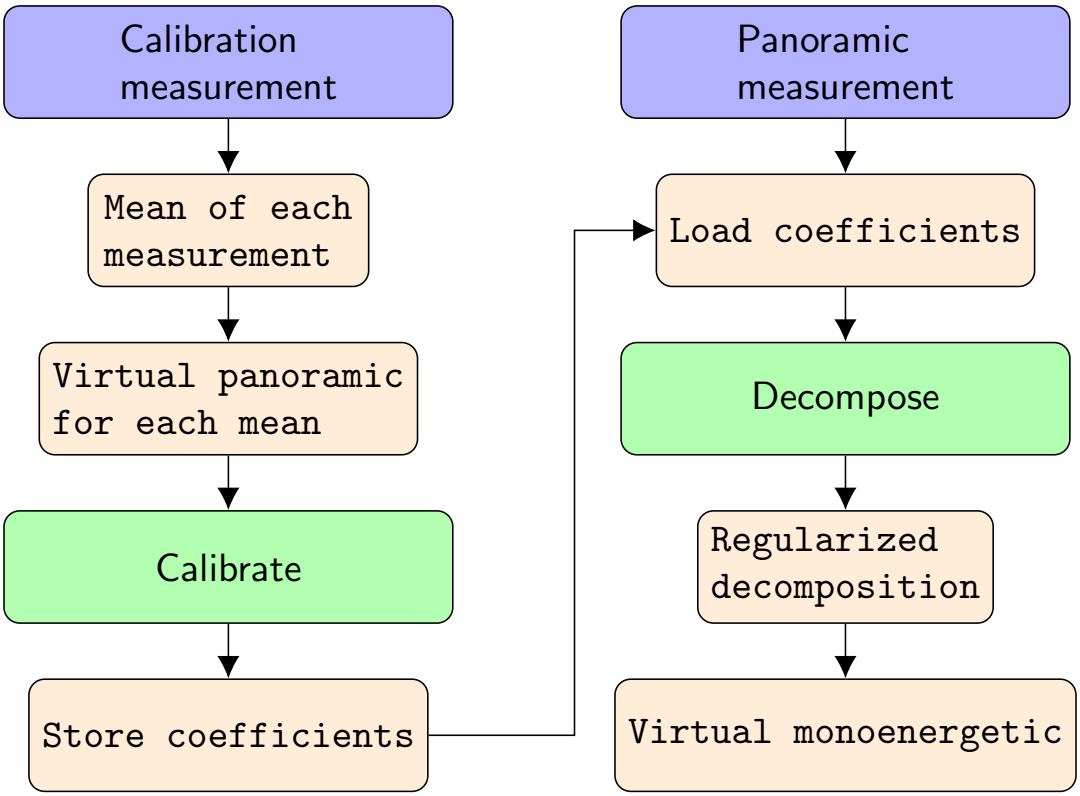

Figure 18: Spectral panoramic imaging workflow. In virtual panoramic images the detector frames are summed in similar fashion to actual panoramic. Thus, the value of each pixel in the output image of a virtual panoramic is the sum from the same pixels in the same frames as in actual panoramic i.e. both virtual and actual panoramic images have the same pixelwise spectral response. This ensures that the model works correctly for actual panoramic images. Calibration needs to be run only once and the same coefficients can be used for different panoramic measurements. [Adapted from [112]]

points is 0.028 cm of titanium (index = 8), with the rest of the errors being around 0.01 cm in fig. 19. For POM the maximum absolute error for this set is 0.55 cm (index = 21), with the rest of the errors being less than 0.4 cm.

Subsequently, a change of basis from POM and titanium was performed into dentin and soft tissue using coefficients from the EPDL97 database [18]. The output of the algorithm described in section 4.2.4 is shown in 21, where the dentin (b) and the soft tissue (c) images in fig. 21 have units of length (cm). Figure 21 also contains the flatfield corrected and linearized all counts image (a) as a reference and as an indication of the total attenuation.

Figure 22 contains the 50 keV virtual monoenergetic image which is unitless. Two regions of interest (ROIs) were chosen from the monoenergetic image in fig. 22 so that ROI 1 had considerable hard tissue component while ROI 2 had only soft tissue component. This is reflected on plots in fig. 22. More specifically, ROI 1 has considerably larger absolute values in attenuation than ROI 2 and the ratio of the absolute values decreases as the function of energy.

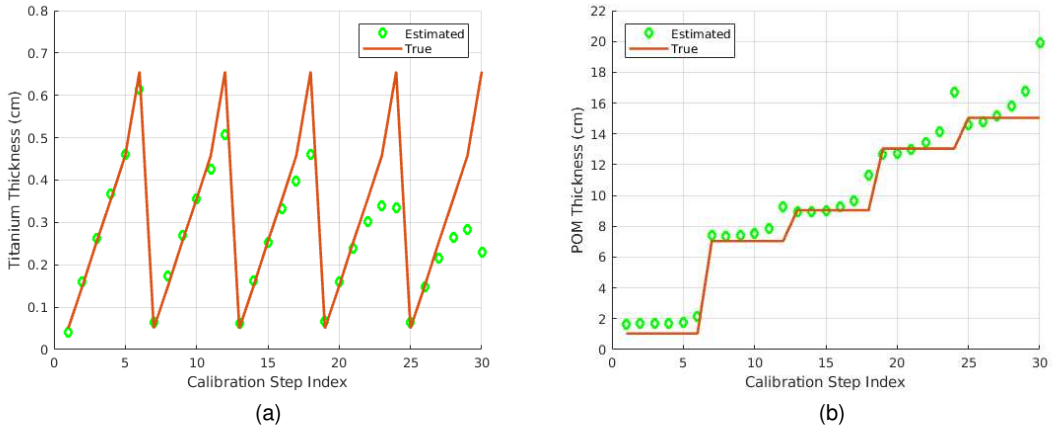

Figure 19: Test decomposition points versus the ground truth for different thicknesses of titanium and POM. Points that have 0.66 cm of titanium are underestimated for POM thicknesses <1.5 cm. Smaller thicknesses of titanium are also underestimated for POM thicknesses <13 cm. For the points which titanium is underestimated, POM is correspondingly overestimated. [Adapted from [112]]

The soft tissue component in fig. 21 is very homogeneous. The reason for this is that the phantom is a skull fully encapsulated in plastic. The skull displaces some plastic so that larger values in the dentin image (b) correspond to locally smaller values in the soft tissue image (c), compare e.g. the lower teeth in fig. 21 (b) and (c) below the red dashed ellipse. In a living human patient there would be air cavities e.g. in the mouth, the nose and the throat. The increased soft tissue values around the center of the image around the horizontal direction are a result of actually having more plastic in the beam path in these directions i.e., the increase in the values in this area is not an artefact. This increased thickness is visible in fig. 22 and in the soft tissue image in 21, but not in the dentin image in fig. 21.

A threshold was applied for inpainting very low photon statistics in the panoramic image before decomposition. Here, a threshold of 10 counts /bin/pixel was applied to the decomposition output as a very low number of counts is typically caused by a metal object in the beam path. Thick metals are not decomposed correctly when there is also a soft tissue or POM component present, e.g. test calibration points 23, 24, and 28-30 in fig. 19. Thus, the dental bridge over the bottom left molars and the implant on a bottom right molar in fig. 21 appear almost monotonously white in the dentin image (b) and black in the soft tissue image (c).

The white blob within the red dashed ellipse in the linearized all counts image (a) fig. 21 is most likely caused by an overlap of the mandible from the other side with the teeth or the maxilla. Thus, for x-ray paths in this area the attenuation is increased. However, this area is actually darker in fig. 21 in the dentin image (b) and again brighter in the soft tissue image (c). This is an indication that the estimation might not work correctly for this area as it does not make sense that the dentin component in this area is smaller than in the surrounding area. In other words, the situation is somewhat similar as in the case of metals, but the number of counts in this area is still above the threshold.

The skull and the teeth are visible and have positive values in the dentin image in fig. 21, while the values between the spine and the jaw are close to zero (e.g. ROI 2 in fig. 22), which is to be

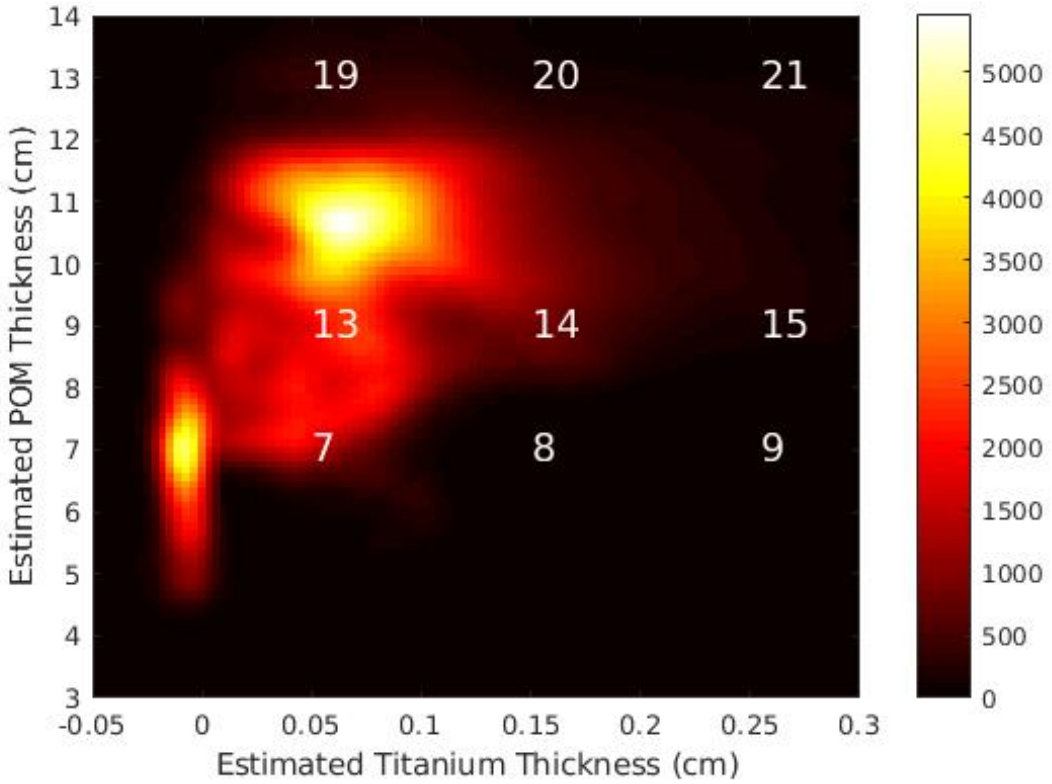

Figure 20: The 2D histogram of the decomposed values of the panoramic image. The test decomposition points which fit within the boundaries are overlaid with the corresponding step index number. The smaller peak at 0 cm titanium, 6–8 cm POM represents the areas where there is no bone. The larger and broader peak at >0.05 cm titanium, >10 cm POM represents the areas with bone. Different parts of skull and jaw have different amount of bone for different line-integrals, hence the more broader distribution. [Adapted from [112]]

expected as there is no bone along those x-ray paths. Most details, e.g. the pulps of the teeth, are still visible in the dentin component in fig. 21 similarly to the all counts image in the same figure. However, the contrast for some of the very finest details has been reduced in the dentin image in fig. 21 (b) in comparison to the linearized all counts image (c.f. the blue ellipses in (a) and (b) in fig. 21).

Areas within the orange and green dashed circles have almost the same intensity the dentin image (b) in fig. 21 but in the linearized all counts image (a) the area within the green dashed circle is darker than the within the orange circle. The latter trend is the same for the soft tissue image (c). In other words, the mandible seems to have somewhat uniform thickness in the dentin component while there is less soft tissue component (plastic in the phantom) along the line-integral paths within the green dashed circle than within the orange circle, according to the output of the algorithm. Recall that the flatfield corrected image represents the total attenuation i.e., both the dentin and the soft tissue components contribute to it. Thus, it makes sense that the mandible area in the linearized all counts image fig. 21 (a) does not have uniform intensity. The mandible area is

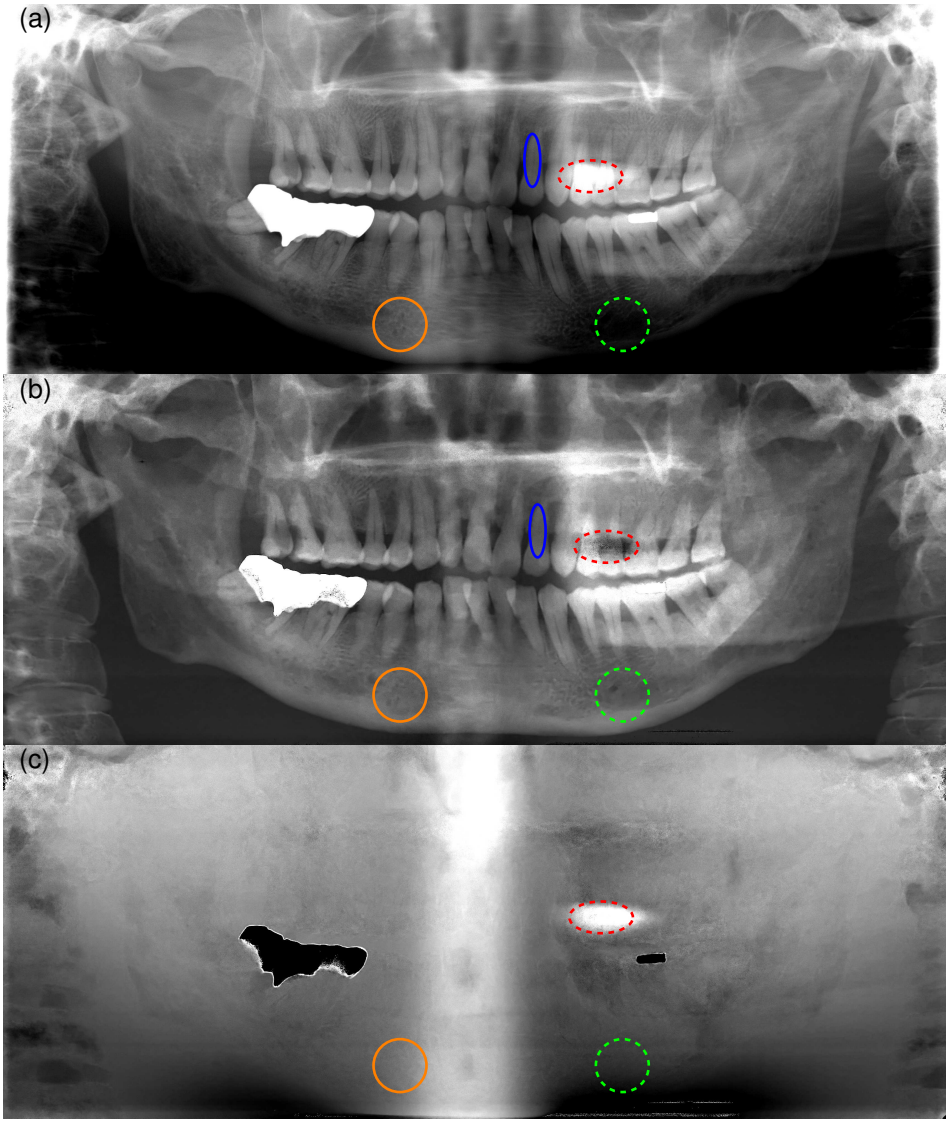

Figure 21: Flatfield corrected and linearised all counts image [7.3–9.6] (a) and the two material decomposition images, dentin [-0.4–1.5 cm] (b) and - soft tissue [7.5–18 cm] (c). Some of the root canals (c.f. blue ellipse) in (a) and (b), is clearly visible in (a), but barely visible in (b). A white blob is highlighted by a red dashed ellipse in (a) and (c). The same area appears as a darker blob in the dentin image (b). Areas within the orange and green dashed circles have roughly the same intensity in (b) but the area within the orange circle is brighter than the area within the green dashed circle in both (a) and (c). [Adapted from [112]]

mentioned as an example here, but the trend is visible over the whole image.

As the decomposition is carried out for the reconstructed panoramic image, some anatomic noise is to be expected. In other words, several frames having slightly different paths through the anatomy contribute to one column in the final panoramic image. Most of the bone (the mandible, the maxilla,

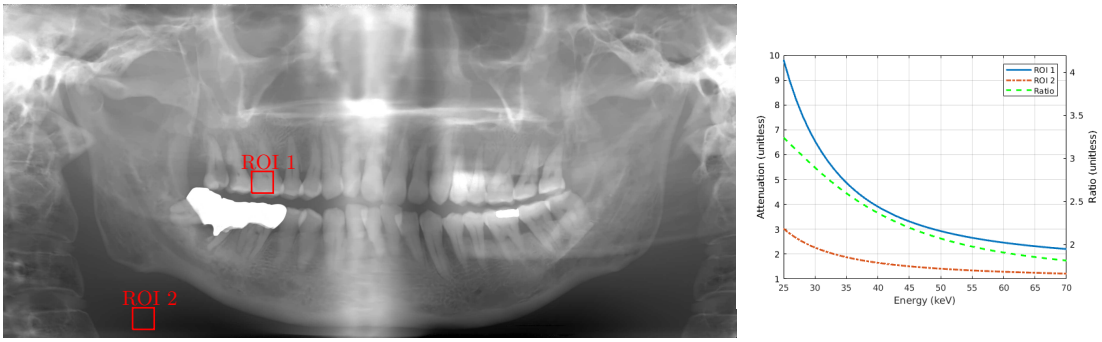

(a) (b)

Figure 22: 50 keV virtual monoenergetic image (a) [1.3-5.6 (unitless)] with energy profiles plotted based on the two ROIs (b). Attenuation is given on the left y-axis and the ratio of the two is on the right y-axis in (b). The signal ratio of the two ROIs in (b) decreases as the energy increases, which is an indication that ROI 1 contains materials with higher atomic number elements than ROI 2. The contrast of the monoenergetic image (a) is defined by the energy used, with higher energies giving more weight to the soft tissue component. [Adapted from [112]]

and the teeth) are withing the sharp layer and do not need to be considered. However, the spine is not within the sharp layer. Furthermore, sometimes the opposing mandible overlaps with the anatomy in the sharp layer and might cause an error. Finally, most of the soft tissue is expected to be outside of the sharp layer, and needs to be considered as well.

The width of the detector (64 pixels) would be an intuitive window size when measuring the horizontal change of thickness in a panoramic image. However, in reality the majority of the signal is carried in the center pixels of the frame, with the edge pixels having only a minor contribution. This is the case due to the collimator blades blocking the majority of the signal at the edges. Thus, we used the full width at half maximum of the mean flatfield frame, 30 pixels, as the width to estimate anatomical noise.

The anatomical noise of the soft tissue component was quantified by estimating the change of thickness in the soft tissue image in fig. 21. The general trend of the image along the horizontal dimension is smooth and almost constant. The strongest change is along the center area, where the maximum thickness change is around 1 cm / 30 pix.

The dentin image in fig. 21 was used to measure the change of the bone signal for spine and the opposing mandible. For the spine, the maximum change was around 0.1 cm / 30 pixels, which was measured from the narrow area below the mandible. For the opposing mandible, the change was 0.25 cm / 30 pixels for the more prominent right side of the image, and 0.05 cm / 30 pix for the left side. This was measured by plotting the edge between the teeth.

4.4 Discussion

The workflow described in subsection 4.2.4 enables the decomposition of panoramic images as 2D images at clinically relevant dose levels. However, the method does lose some spectral sensitivity by summing pixels along the horizontal dimension. Different pixels in a physical detector have slightly varying energy responses and summing them together widens spectral overlap across the energy bins.

Regarding anatomical noise, the center pixels for the soft tissue in fig. 21 were identified as an area where the noise is the highest. For bone, the border with opposing mandible and the spine were identified as having some noise. The implication here is that the neighbouring columns have also contributed to the absolute value when looking at the soft tissue or dentin images at the respective areas. Finally, details outside the sharp layer will be blurred. However, this is the case for panoramic in general, not just the spectral algorithm presented in this paper.

Even after the calibration, the model presented in subsection 4.2.1 has finite accuracy in decomposition as indicated by fig. 19. Errors get larger if the material thicknesses in imaging are larger than in the calibration. Furthermore, the model has not been designed to account for scatter. Even though the calibration materials were placed in contact with the collimator, due to the small source to image distance, some amount of scatter still reached the detector. For increasing thicknesses, more photons interact via Compton or Rayleigh scattering, while the number of unattenuated photons gets exponentially smaller. The model assumes that photons which interact with the object being imaged do not cause counts in the detector. This is strictly speaking never the case, but issues appear to arise only for the strongly attenuating test decomposition points in fig. 19. In contrast, when observing the distribution of panoramic decomposition results in fig. 20 we see that a vast majority of the points are $<12\,\mathrm{cm}$ of POM, $<0.2\,\mathrm{cm}$ titanium. As the test decomposition points in this regime are decomposed quite accurately in fig. 19, a low decomposition error can also be assumed for the sample scan. Finally, it should be noted even the more accurately test decomposed regime has larger errors than a test decomposition in a previous study [113], which also used a projection domain decomposition, although with higher kVp (more transmission) and larger source to image distance (less scatter). Transmission in the setup used in this work could be increased by using a higher kVp and/or adding more filtration. A new tube should be added for this and care should be taken so that neither the dose nor the exposure time increases.

The impact of scatter was not quantified in this study, but it is a possible cause of the bias, especially if there are thick metals in the beam as discussed above. In the case of CBCT of a head, the scatter signal can exceed the primary signal reaching the detector in the head area [8] which would lead to severe bias in eq. 4.5. However, panoramic imaging uses a very narrow collimation in the horizontal direction which means that the scatter is not as high as in CBCT. Nevertheless, a strongly attenuating metallic object, such as a dental bridge (c.f. fig. 21 (a), white object on the left side of the image, on the molars), blocks virtually all direct radiation and only the overlapping scatter background remains, introducing a strong bias to the decomposition results in that area. In the future, a kernel based scatter correction method [114] could be experimented with to mitigate scatter without needing a 3D reconstruction of the imaged object.

Despite the measures taken to minimize pileup (cf. 4.2.3), pileup still might cause some error to the final results as charge-sharing correction increases the deadtime by an order of magnitude [43].

Despite the aforementioned limitations, the algorithm is clearly able to separate the plastic and the skull from each other, as seen in the plot of ratios in fig. 22 and in fig. 21. This implies, that the limitations do not degrade neither spectral nor anatomical separation efficiency too much. A clinical study would be required to confirm if the soft and hard tissue anatomies indeed are be separated for actual human patients as well.

One implication of fig. 21 is that bone mineral density measurement using a hard tissue (e.g. dentin) basis material image might be possible. It was attempted on [106] directly from the count data, but was too unstable, one possible explanation being the soft tissue background. Our algorithm takes into account the spectral response and the material decomposition yields quantitative line-integral values which might make it more suitable for this task, but further investigation is required.

4.5 Conclusion

We have built a prototype panoramic X-ray photon counting system and developed a new algorithm which enables material decomposition for panoramic imaging. By doing the calibration from the virtual panoramic images, the calibration result is enabled to be sensible despite the very low photon statistics. The decomposition of a spectral panoramic image into soft and hard tissues might be advantageous in clinical cases where the overlap of soft and hard tissues is a problem or where having the bone mineral density information might be advantageous. This should be verified in clinical trials.

5 Generating spectral dental panoramic images from computed tomography volumes

This chapter continues from the experimental foundations of spectral panoramic imaging laid out in the previous chapter. This chapter presents simulation framework for generating synthetic panoramic images from both CT and CBCT volumes. The soft and hard tissues are segmented from the volumes and forward projected to generate a panoramic images. It possible to adjust the dental arch and method on how the panoramic image is generated. Thus, it also possible to experiment with different geometries and estimate anatomical noise.

This text and figures have been made available in preprint as:

- V Somerkivi, et al. Generating spectral dental panoramic images from single energy computed tomography volumes. arXiv:2305.10087 (2023).

Slight modifications have been made to incorporate the text and figures better into this doctoral thesis.

5.1 Introduction

Dental panoramic X-ray imaging is a common imaging modality around the world. According to United Nations Scientific Committee on the Effects of Atomic Radiation, the panoramic imaging examination frequency per 1000 population was 140 in Germany, 120 in Japan, 74 in the United Kingdom, and 64 in the United States [5]. It provides a low-dose radiographic image, which is used mainly for a high- resolution view of the maxilla, the mandible, and the teeth and any lesions in these structures [6]. A panoramic image is generated by moving and rotating the X-ray tube and the detector in parallel to the dental arch while maintaining a constant magnification of the arch, as shown in fig. 12. In the case of a digital detector, frames are captured at a high frame rate and summed with a partial overlap to generate the panoramic image [95]. Different tissue types are superimposed in conventional, transmission-based radiography, including panoramic imaging. This superimposition causes difficulties and confusion in the interpretation of panoramic images. For example, the oral cavity can be mistaken for a fracture in the mandible, even though the cavity is in the soft tissue [115].

Spectral X-ray imaging has been studied extensively in the past 15 years [63] [103] [64] [101]. These studies have demonstrated that material decomposition provides additional information on top of the normal attenuation images by revealing clinical features which would be invisible in a conventional attenuation image. Recently, spectral panoramic imaging specifically has also been investigated [105] [106] [112]. A previous work demonstrated that it is possible to achieve material decomposition in panoramic imaging for as long as there is a sufficient number of counts for calibration and decomposition [112].

Currently, no clinical studies on the feasibility of spectral panoramic imaging have been published. Preliminary results from a previous pre-clinical study have been obtained [112]. However, the confidence in the results would increase if there was a reference to compare these results to. Several approaches to generate synthetic panoramic images from CT have been described [116] [117] [118] [119]. These approaches aim at automatically or semi-automatically finding the dental arch, e.g. by using the maximum intensity projection along the axial slices followed by subsequent thresholding and morphological thinning. After the dental arch has been extracted, the panoramic image is generated by extracting voxel values along lines which are orthogonal to the dental arch. The length of lines is set so that the lines run through the mandible, the maxilla, and the teeth while

the rest of the lower head is left out. This kind of process may be suitable for generating synthetic panoramic images for reading in dental practice. However, if verification is desired, then the whole image generation process should be modeled. This includes forward projecting actual frames and summing the frames to get the panoramic image. Additionally, the generation of basis material images is required when modeling spectral imaging.

This work introduces a framework for generating spectral panoramic images from CT volumes. We use a CT image of an anthropomorphic head phantom as input and generate a set of spectral panoramic images using the framework. We then cross-compare the output of the framework against experimental spectral panoramic images.

5.2 Methods

5.2.1 Simulation framework

The framework was implemented in Python (Python Software Foundation, Wilmington, Delaware, United States). A proprietary X-AID module (MITOS GmbH, Munich, Germany) was used for the forward projection step. The main steps of the workflow are shown in fig. 23 and the detailed explanation is below.

The first part of the framework deals with preparing the input CT volume for the workflow. If the voxels are not isotropic, e.g. the input is from a helical CT, an interpolation is first carried out so that the output is isotropic. Secondly, the user has to rotate the volume along the three axes so that the volume is symmetric along the coronal and axial views, and the dental arch is horizontal in the sagittal view. The final step of the preparation is thresholding the volume to two basis materials. There are two ways to carry out the thresholding, depending on the type of the input volume.

A simple threshold is used in the segmentation if the imaging system's Hounsfield Unit (HU) values are not perfectly reliable due to scatter contamination [8]. A threshold of 1280 HU was used in this study. Both basis material images are scaled with their respective mean signals so that the mean value of the segmented volumes is 1.

If the HU values of the input volume are more reliable e.g., by reducing the scatter contamination by using an anti-scatter grid [120], then a more sophisticated thresholding is possible in the framework. The method uses a sheetness score combined with a threshold in order to better segment the bone, as bones in the skull mainly consist of sheet-like structures [121]. The sheetness score S is calculated as in [121]:

$$S = \exp\left[\frac{-R_{\text{sheet}}^2}{2\alpha^2}\right]\left(1-\exp\left[\frac{-R_{\text{tube}}^2}{2\beta^2}\right]\right)\left(1-\exp\left[\frac{-R_{\text{noise}}^2}{2\gamma^2}\right]\right), \tag{5.1}$$

where $R_{\text{sheet}} = |\lambda_2|/|\lambda_3|$, $R_{\text{tube}} = |(2|\lambda_3| - |\lambda_2|) - |\lambda_1|)|/|\lambda_3|$, and $R_{\text{noise}} = \sqrt{\lambda_1^2+\lambda_2^2+\lambda_3^2}$ with λ_i being the local Hessian eigenvalues so that $|\lambda_1| \leq |\lambda_2| \leq |\lambda_3|$. α and β are set to 0.5 here, while γ is equal to maximum of R_{noise}. The output HU values Ω are then:

$$\Omega = \begin{cases} -1000 & \text{if } (\Omega_i S \cdot 5 + \Omega_i) \leq T \\ \Omega_i S & \text{othwerwise} \end{cases}, \tag{5.2}$$

where Ω_i are the HU values of the input volume and T is the threshold value. $(\Omega_i S \cdot 5 + \Omega_i)$ was heuristically found to yield good results in the thresholding.

The next step is to trace the dental arch of the volume. The dental arch needs to be correctly registered in order for the panoramic reconstruction to succeed (c.f. fig 12). This requires the user to manually provide the coordinates of the dental arch. There are two ways to achieve this

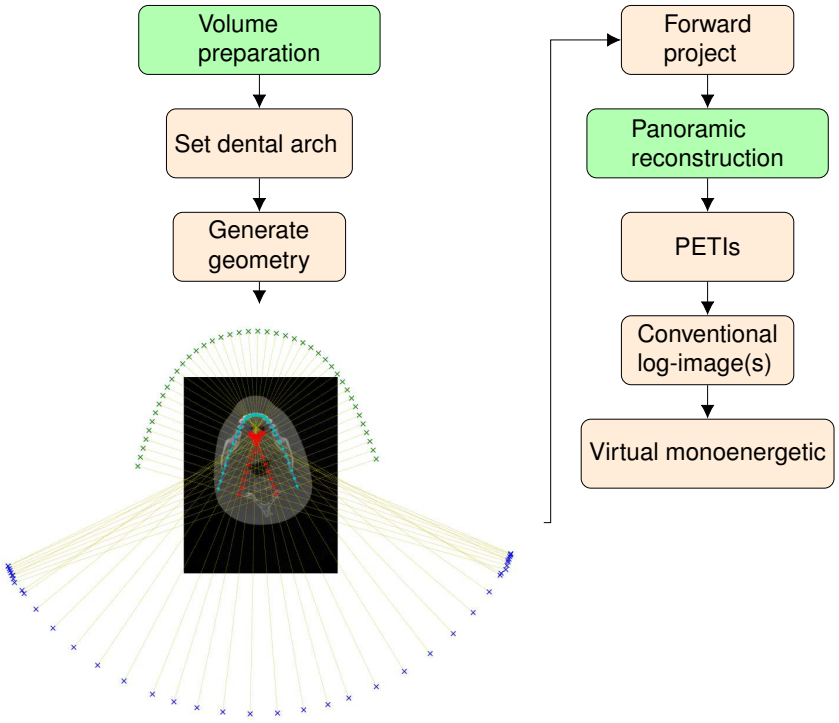

Figure 23: Main steps of the simulation framework. PETI stands for panoramic equivalent thickness image. The dental arch used and the geometry generated from the arch are shown overlaid with an axial slice of a volume on the bottom left side. Every 60th projection is shown, with green being the detector, dark blue the source, cyan the focal through, and red the rotation center. [Adapted from [80]]

in the framework: u-shaped (9 coordinates) and exact (11 coordinates) arches. The u-shaped arch generates a smoother profile with a smaller number of rotations. The u-shaped arch was used in this work (shown in fig. 23) as it corresponds better to a realistic trajectory. It is also possible to restrict the overlap of the mandible from the other side in the framework. This feature was not used for the results presented in this paper, as it was desirable to have the simulation results match the experimental results. The dental arch is created by interpolating between the user-given points by using the piecewise cubic hermite interpolating polynomial (PCHIP) algorithm. The algorithm is desirable for creating the dental arch, as it is more resistant to ringing artifacts than spline or regular polynomial-based interpolation algorithms [122].

After the dental arch is complete, the subsequent step is forward projecting the frames. The X-AID module uses a ray-driven forward projector which traces the path from the source to the target pixel and sums up everything along the path. The panoramic reconstruction is carried out by summing the frames according to the movement profile generated using the dental arch (c.f. fig. 23).

The output of the panoramic reconstruction is called a panoramic equivalent thickness image (PETI) in this framework. In this case, the volume was thresholded into soft tissue and dentin.

Thus, the output here is two PETIs of soft tissue and dentin with a unit of thickness (mm by default).

For the generation of log images, dentin and soft tissue PETIs were used as basis materials. The linear attenuation coefficients (LACs) are obtained from the XCOM database [23]. The pyXSFW framework [123] was used to model the tungsten anode spectrum. The detector was modeled as having a sensor thickness of 0.75 mm of cadmium telluride, with each absorbed photon inducing one count. With the spectrum and the LAC(s) known for both basis materials and the detector, the output signal can be calculated:

$$I = \sum_{E=1}^{\infty} I_0(E)D(E)F(E)e^{-A_{st}\mu_{st}(E)-A_d\mu_d(E)}, \tag{5.3}$$

where $I_0(E)$ is the input spectrum, $D(E)$ is the detector absorption efficiency, $F(E)$ is the spectral response of the detector, A_{st} and A_d are the respective soft tissue and dentin line integral lengths, while $\mu_{st}(E)$ and $\mu_d(E)$ are the energy-dependent soft tissue and dentin LACs, respectively.

No quantum noise was added to the images in this work, as the purpose was to evaluate the feasibility of the results in the sense that the output is as expected. While the experimental results are subject to quantum noise, it would not make the comparison easier or better to add noise to the synthetic images. If there was a need to add quantum noise, it should be added to the forward projected frames before panoramic reconstruction. This would ensure that the reconstructed image has a realistic noise distribution.

Virtual monoenergetic images (VMIs) are generated by multiplying the PETIs with their respective LACs and then summing them together.

The individual projections making up a single output pixel in a panoramic image all pass through the patient at a slightly different path. However, all overlap in the sharp layer (c.f. fig. 12). Anatomical noise in a panoramic image pixel is measured by recording all of the pixel values from the frames contributing to the pixel in the panoramic image. In other words, this indicates how different the individual line integral paths making up the final panoramic image pixel are. The mean of these values is the final PETI output value in the pixel.

5.2.2 Experimental measurements

5.2.3 CBCT acquisition

Planmeca Viso G7 (Planmeca Oy, Helsinki, Finland) was used for the CBCT acquisition. The acquisition was carried out in offset mode, and two rotations were conducted and stitched together to acquire the whole head phantom. The reconstructed volume was used as input to the simulation framework. The size of the reconstruction output grid in voxels was 1216x1193x1361 (width, lenght, height). The acquisition parameters are listed in table 3. The dose is higher than what would be used in the typical patient acquisition, as high resolution with lower noise was desired.

The anthropomorphic head phantom RANDO SK150 (Radiation Analogue Dosimetry System; The Phantom Laboratory, Salem, NY, USA) was used in this study. The phantom is a skull encapsulated in plastic. The plastic has air cavities that mimic the upper respiratory tract. A hole has been drilled into the phantom from the bottom of the jaw so that there is also a cavity in the bottom of the jaw in the plastic and in the mandible.

5.2.4 Spectral panoramic acquisition

The polynomial model and its calibration were discussed in section 4.2.1.

Table 3: CBCT acquisition parameters.

source to image distance	70 cm
acceleration voltage	120 kVp
tube current	11 mA
exposure time	11.4 s
dose-area product	4100 mGycm^2
magnification	1.5
isotropic voxel size	225 μm
field of view (width×height)	25×30 cm^2

Panoramic imaging presents a new challenge to the decomposition process, as individual frames in panoramic imaging have a very low number of counts. Directly decomposing frames would induce severe statistical bias to the decomposition [104]. On the other hand, the count statistics in the final panoramic image are sufficient for typical line integrals in the jaw area [112]. However, to decompose the final panoramic image instead of individual frames, an appropriate calibration needs to be carried out. One such way is generating virtual panoramic images for calibration. This involves taking still calibration exposures, taking the mean of each measurement, and performing a panoramic reconstruction for each mean frame by using the mean frame as every frame in the reconstruction. The final panoramic image can then be calibrated using these virtual panoramic images. Thus, the actual panoramic exposure will have the same flatfield values and pixel weights as the calibrated panoramic image. A change of basis from the calibration materials into soft tissue and dentin is carried out after the decomposition. A detailed explanation of the whole process can be found in [112].

An experimental spectral photon counting panoramic system was used to capture an image of the same phantom. The Planmeca Promax Mid (Planmeca Oy, Helsinki, Finland) system has a DC-Vela detector (Varex Imaging Corporation, Salt Lake City, USA). DC-Vela is a photon counting detector with two adjustable thresholds, a charge sharing correction, and a 0.75 mm cadmium telluride sensor layer. The acquisition parameters for the experimental panoramic system are shown in table 4.

Table 4: Panoramic acquisition parameters.

source to image distance	60 cm
acceleration voltage	70 kVp
tube current	9 mA
exposure time	18 s
dose-area product	72.1 mGycm^2
magnification	1.4
field of view (width×height)	0.6×15.41 cm^2

A decomposition process like the one described in this section was not modeled in the simulation framework. If the same forward model is used to simulate the transmission and to decompose, the output of the decomposition will be the same as the input in the absence of noise. This holds as long as the input volume is segmented into exactly two basis materials.

5.3 Results

The output of the simulation framework is shown in fig. 24. As expected, the maxilla, the mandible, and the teeth are the prominent features of the dentin image (a). The spine is also visible to the sides. The soft tissue image (b) has larger line integral thicknesses to the center. Outside of the center, there are homogeneous areas with, darker air gaps with the upper respiratory tract being the most prominent. The tract starts at the sides, next to the spine, and extends upwards until splitting into the oral and nasal tracts and arching towards the center. There are also darker areas in the soft tissue image (b) in the same places where the bone features are in the dentin image (a). For example, the spine, the mandible, and the teeth are visible as darker areas in the soft tissue image (b). The drill hole (solid orange ellipse) is visible in both images. This is expected, as the hole was indeed drilled through the bottom of the jaw and partially through the mandible. The air gaps highlighted in (b) by the larger and smaller dashed ellipses are not part of the respiratory tracts. The gaps are roughly where the maxillary sinuses would be. While darker areas are inside the ellipses, the areas are only barely visible.

The basis material images from the experimental system are shown in fig. 25. The maxilla, the mandible, and the teeth are the dominant features in the dentin image (a). The soft tissue image (b) is quite homogeneous, with the air gaps, especially the upper respiratory tract being the dominant features. The air gaps not being part of the respiratory tract are again highlighted by the dashed ellipses. In the experimental image 25, these gaps stand out more prominently, although the smaller gap overlapping with the lower nasal cavity limits its visibility.

Figure 25 is similar to what was described in a previous work [112]. The most notable difference is the presence of the upper respiratory tract in the soft tissue image. Note that the images of this work are left-right flipped, unlike the image in the previous work. Dentin was considered to be a good basis material in the previous work, so it was kept the same in this work. The calibration of the panoramic system, including the results of the test decomposition and noise considerations are discussed in detail in a previous work [112].

There are some differences in features between the bone component in figures 24 and 25. The mean line integral length of fig.3 (a) is lower than fig. 4 (a). The overlap from the mandible from the other side has locally very large values in fig. 24, however. This is why the windowing is wider in fig. 24 (a) than in fig. 25 (a). In fig. 24 (a), the contrast between the body and the base of the mandible is more prominent than in 25 (a).

The soft tissue images (b) have notable differences in 24 and 25. The soft tissue image in 25 is much more homogeneous than 24. More specifically, the bright features in the synthetic dentin image (a) in fig. 24 appear dark in the soft tissue image (b) in fig. 24. In other words, the negative correlation between the experimental basis material images in 25 is much smaller than in the synthetic images in fig. 24. On the other hand, the upper respiratory tract is clearly visible in both soft tissue images. Additionally, the drill hole can be seen in both the dentin images and both soft tissue images in figures 24 and 25.

The shape of one of the overlapping mandibles is highlighted by a blue dashed line in figures 24 and 25. But the exact location and shape of the overlap is different between the two figures. This is a result of different imaging geometries. The experimental device uses a fixed geometry, whereas the simulator uses a manually defined geometry, which is specifically tuned for each volume.

The details in fig. 26 show slices from the CBCT acquisition. The slices confirm that there are indeed air gaps in the positions highlighted in fig. 24 and fig. 25. The drill hole is inside the mandible but is visible in all of the images in figures 24 and 25.

Figure 27 displays the anatomical noise for both the soft tissue and the dentin PETIs of two pixels in fig. 24. More precisely, each histogram in fig. 27 is generated by recording the individual

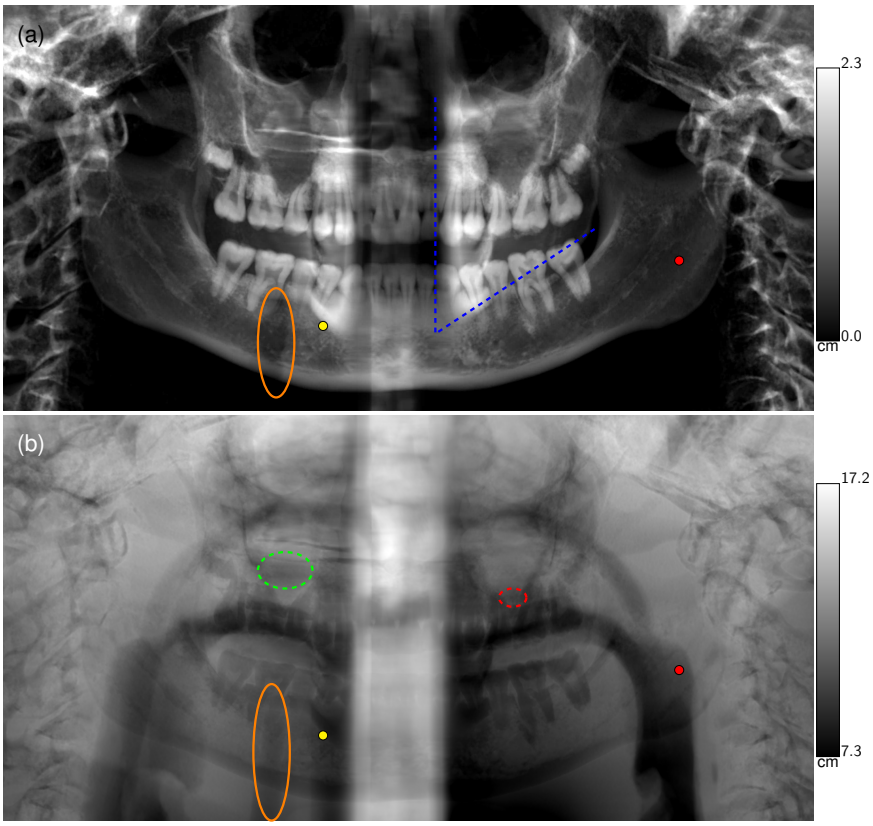

Figure 24: Synthetic pan images, generated from the CBCT scan of the RANDO SK150 phantom. A solid orange ellipse highlights the drilled hole in both images. The blue dashed lines highlight the boundary for the overlapping mandible from the other side in the bone image (a). The two dashed ellipses show small air gaps in the plastic in the soft tissue image (b). Many dark features in the soft tissue image (b) are not air but the absence of bone i.e., there is a strong negative correlation between the two images. [Adapted from [80]]

projections contributing to the panoramic image's particular pixel. These two cases were included to highlight the extremes in the anatomical noise. The upper two histograms are near the boundary of the mandible overlap. The values close to 18 mm (b) are a sum of the overlap and the actual signal, while the lower values are only from the actual signal. The lower two histograms are from a region with little anatomical noise. Thus, the values are very close to each other. Most of the panoramic image has a noise magnitude close to pixel (900, 2390), while an increase in the noise is observed for bone – soft tissue boundaries with pixel (1131, 1180) as an extreme case with the mandible overlap.

5.4 Discussion

The presented framework enables generation of panoramic images from CT and CBCT volumes. The PETIs generated this way resemble the experimental material decomposition panoramic images. The framework also enables quantitative and pixel-wise estimation of anatomical noise in panoramic

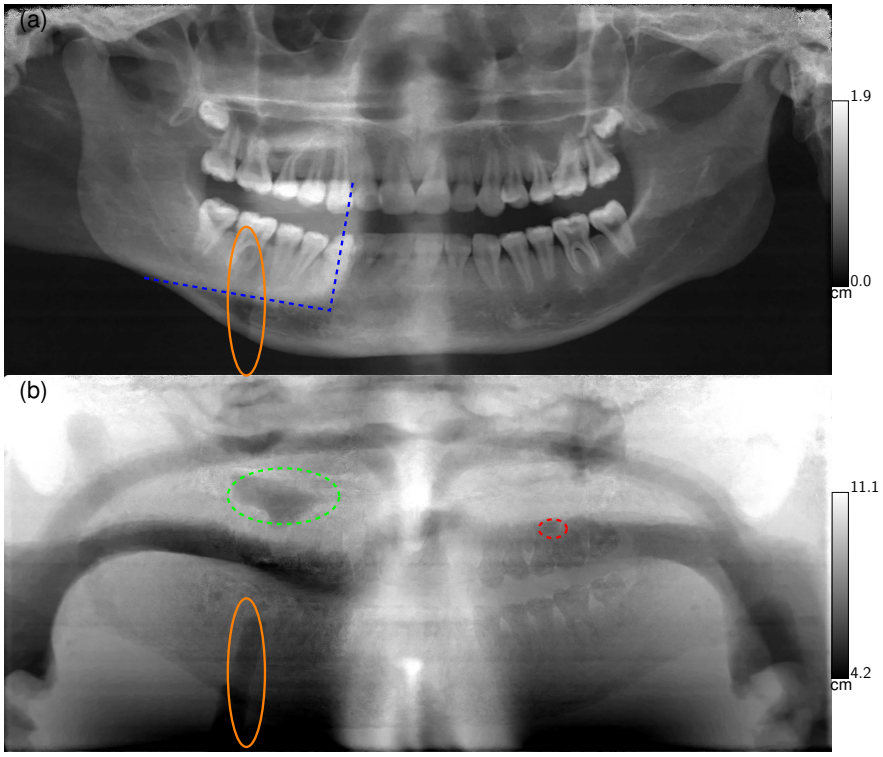

Figure 25: The experimental panoramic images. The highlighted details are the same as in fig. 24. The overlap from the mandibles is not symmetric in (a), as the overlap on the right side of the image only starts from a higher and more away from the center than the overlap on the left side. Here, the darker features in (b) are mostly air gaps in the phantom. The yellow and the red points are the anatomical noise measurement pixels.

images.

The thresholding approach for segmentation assumes that one voxel induces a signal only on the soft tissue or bone image, but not both. The assumption may be correct for voxels containing only plastic, as they should only contribute to the soft tissue image. The skull, on the other hand, consists of more than one type of tissue. For instance, cancellous bone [124], cortical bone [124], dentin [53], and enamel [53] have different effective atomic numbers and are to an extent present in the skull. Furthermore, in reality, one voxel can have more than one tissue type.

The overlap of the mandible from the other side appears different in figures 24 and 25 due to the different geometries. The difference has an impact on both location and the intensity of the overlap. Ideally, the geometry of the experimental setup should also be used in the simulation framework to mitigate these differences. However, the exact geometry of the used imaging system is not publicly available. The non-symmetrical overlap of the mandibles in the experimental image is likely caused by a sub-optimal mounting of the detector in the experimental system.

The value of a single panoramic image output pixel consists of line integrals passing through the lower head at slightly different paths. The values of the line integrals passing through the mandible

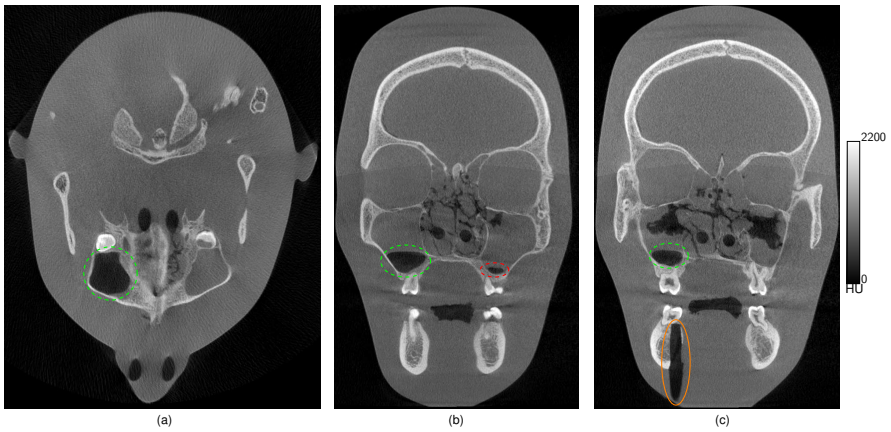

Figure 26: An axial and two coronal slices showing the same details in the CBCT image as in the two pan images. From the CBCT image, it is confirmed that there are indeed air gaps in the highlighted positions. The visible soft tissue boundary in (b) and (c) around eye sockets' upper part marks the two rotations' stitching boundary. [Adapted from [80]]

are very close to each other (bottom row of fig. 27) (excluding the opposing mandible overlap region as seen on the top row of fig. 27). This implies that a minor deviation in the angle or location of the path does not change the line integral value notably. Thus, a slight variation in the geometry should not provide notably different values, assuming the sharp layers of the two geometries mostly overlap. This assumption is satisfied in this work as details like the pulps or the mandibular canals would no longer be visible if the two geometries' sharp layers were not close to each other.

The choice of PETI materials is somewhat arbitrary when segmenting CT volumes. Dentin and soft tissue were used in this study as they are a good guess with respect to the effective atomic numbers and densities of the underlying materials. Cortical bone could have been used instead of dentin, as their attenuation profiles are close [124, 53]. The experimental setup decomposes images initially into the calibration materials, in this case, titanium and polyoxymethylene (POM). In the subsequent change of basis it has to be decided which materials and energies for low and high bins are used, which are again arbitrary to some extent. In other words, there is no single correct value for the experimental output images. Thus, it is not feasible to expect the synthetic and experimental panoramic images to match exactly.

The input volumes should ideally have both high-resolution and reliable HU values. This would enable reliable two-material segmentation while preserving bone feature visibility. Reliable HU-values would also increase the volume of segmented images, as with the system used in this study some of the cancellous bone was segmented as soft tissue. Partially missing cancellous bone is a plausible explanation as to why the contrast between the body and the base of the mandible is stronger in fig. 24 than in fig. 25. An increase in the soft tissue – bone threshold would result in soft tissue being segmented as bone. With reliable HU values, the bone could be potentially segmented into more than two basis materials, making the results even more realistic.

With the aforementioned differences in the generation of the experimental and synthetic spectral panoramic images in mind, it was expected that the two images are not exactly the same. Nevertheless, the close resemblance of the two images increases the confidence that the output of the experimental spectral panoramic imaging workflow is feasible and expected. Additionally, the

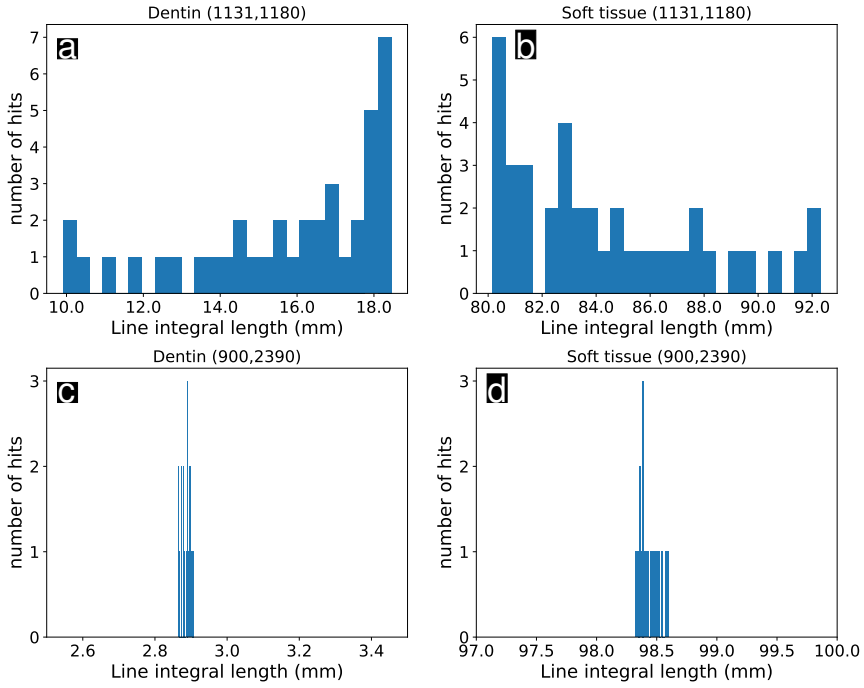

Figure 27: dentin and soft tissue anatomical noise histograms from two locations with pixel indices given in (height, width). The yellow point in fig. 24 corresponds to the top row (a) and (b) and the red point (c) and (d) to the bottom row. Observe that the x-scales are very different for the two rows (compare (a) vs (c) and (b) vs (d)). [Adapted from [80]]

developed simulation framework will be useful in further exploring spectral panoramic imaging.

The framework will be adapted for dual-energy CT (DECT) input in a future work. DECT images can be decomposed and forward projected directly without thresholding. This way, a voxel can consist of more than one material. DECT decomposed images can also be used as a reference for estimating bone mineral density (BMD) [125]. Photon counting CT (PCCT) provides the same benefits as DECT while having spatial resolution close to CBCT [32]. Thus, PCCT would be the ideal way to provide the ground truth for BMD estimation from spectral panoramic images. Another future work will explore the clinical relevance of PETIs.

5.5 Conclusion

A framework for generating synthetic spectral panoramic images from CT volumes has been successfully implemented. The synthetic panoramic images obtained using the framework support the results obtained from the experimental spectral panoramic system. The framework also provides a basis for further research.

6 Mandible bone mineral density estimation using spectral panoramic X-ray imaging

In this chapter, the feasibility of bone mineral density measurement using spectral panoramic X-ray imaging is assessed. We first expand the simulation framework to work on dual-energy data. Specifically, the input is decomposed into basis materials rather than segmented. Thus, the framework also outputs bone component images comparable to the experimental system. A clinical DECT system is used to acquire reference images of head phantoms containing real human skulls. Dedicated dual energy phantom is also used for verification. The impact of positioning errors is also assessed (see section 3 for details).

The text and figures have been published as:

- V Somerkivi, et al. Mandible bone mineral density estimation using spectral panoramic X-ray imaging. Imaging Science in Dentistry, vol. 55, no. 1. 2025.

Slight modifications have been made to incorporate the text and figures better into this doctoral thesis.

6.1 Introduction

Osteoporosis affects at least 200 million people worldwide [126], and it is responsible for over 1 million fractures annually in the United States alone [127, 128]. In addition, osteoporosis increases the risk of dental implant failure [129] and periodontal disease [130]. Early detection of osteoporosis enables treatment with dietary supplements and increased physical activity [131].

Bone mineral density (BMD) is a key indicator of osteoporosis and is most commonly measured at the lumbar spine using dedicated dual-energy X-ray absorptiometry (DXA) systems [132]. However, BMD can also be assessed at other anatomical sites, reflecting overall bone health. [130]. Mandibular BMD, in particular, correlates significantly with measurements taken at the forearms and lumbar spine [131, 133, 134], and serves as an important marker of skeletal health. Although dedicated mandibular DXA scanners have been available for several decades [130, 133], they are not widely used clinically. Instead, the health of the mandible is currently evaluated by visual assessment of panoramic images acquired via dental panoramic X-ray imaging-a low-dose and widely available modality in dental clinics [135]. BMD can also be measured from the extremities and the mandible using CBCT [136] and approximately the same number of panoramic images and CT images are acquired globally each year [5].

The newly developed technique of spectral panoramic X-ray imaging enables obtaining quantitative measurements of soft tissue and bone thickness. [112]. The resulting bone thickness images may be well-suited for estimating BMD from panoramic images. If BMD estimation can be successfully integrated into these systems, it could enable the generation of substantial, clinically relevant BMD data without increasing radiation exposure or complicating existing workflows.

This study evaluated the feasibility of spectral panoramic imaging for generating BMD maps of the mandible. Reference data were obtained from a clinical dual-energy computed tomography (DECT) scanner, and a simulation framework from previous work [80] was adapted to produce basis material panoramic images from decomposed DECT volumes. Experimental basis material images were then compared to their synthetic reference counterparts to assess the suitability of the spectral imaging approach.

6.2 Methods

6.2.1 Phantoms

A total of 3 anthropomorphic head phantoms, each containing a real human skull encased in plastic, were used in this study. Two of these were RANDO SK150 phantoms (Radiation Analogue Dosimetry System; The Phantom Laboratory, Salem, NY, USA), and the third was an X-ray Phantom Head (Erler-Zimmer GmbH, Lauf, Germany). The 2 RANDO SK150 phantoms feature air holes in the plastic that mimic the upper respiratory tract; one (labeled 1) has a drilled hole in the mandible, while the other (labeled 2) does not, as shown in Figure 28 A. The X-ray Phantom Head (labeled 3) contains no air gaps in its plastic construction.

To assess the linearity of the BMD scores, the Gammex 472 dual energy phantom (Sun Nuclear, Melbourne, FL, USA) was used. This phantom contains inserts with calcium concentrations of 50, 100, 200, 300, 400, 500, and 600 mg/mL, each with a diameter of 2.85 cm. Calcium, being the heaviest element in the bone mineral hydroxyapatite: (HAP, $Ca_5(PO_4)_3OH$) is critical for these measurements. A solid water insert served as the reference. Additionally, 10 cm of polymethyl methacrylate (PMMA) slabs were stacked in the background to simulate the soft tissue component of the head phantoms. The measurement configuration is illustrated in Figure 28 B, and a region of interest (ROI) measuring 100 pixels in height by 200 pixels in width was used to measure the aBMD over the cylindrical inserts

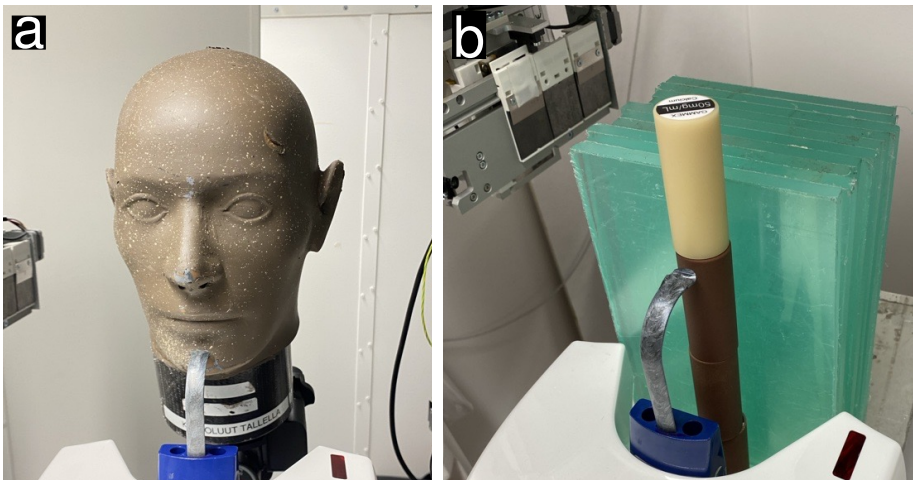

Figure 28: A. Anthropomorphic head phantom number 2: RANDO SK150 (Radiation Analogue Dosimetry System; The Phantom Laboratory, Salem, NY, USA). B. Gammex dual-energy inserts (Sun Nuclear, Melbourne, FL, USA) with the PMMA background

The most suitable area for the areal BMD (aBMD) measurement is in the mandibular body, below the molar and the canine teeth (c.f. [131] and the references therein). This site is anatomically the most stable across different patients; i.e., when comparing aBMD scores across patients is the most relevant. It also has the highest correlation of aBMD values with most other bone sites in the body [133]. More specifically, the goal was to use the whole mandible under the 2nd premolar, 1st molar, and 2nd molar to measure the aBMD score (c.f. Fig. 29). A rectangular region of interest (ROI)

was selected to cover the whole area under the teeth. The ROI size varied somewhat with anatomy, but all ROIs were roughly 300 pixels in height and 400 pixels in width.

For the head phantoms, the optimal area for areal BMD (aBMD) measurement was the mandibular body, located below the molar and canine teeth [131]. This site is anatomically stable across patients, making it particularly relevant for comparative aBMD assessments, and it exhibits the highest correlation with aBMD values at other skeletal sites [133]. Specifically, a measurement was taken from the entire mandible region beneath the second premolar, first molar, and second molar (see Fig. 29). A rectangular ROI, approximately 300 pixels in height and 400 pixels in width (with slight variations depending on anatomy), was used to encompass the area under the teeth. The aBMD score at the mandibular angle was measured in a similar manner; however, this region typically exhibits lower aBMD values than the mandibular body, [133] thus providing a broader range of values.

Panoramic imaging is sensitive to patient positioning [137]. Common errors include placing the head outside the sharp focal layer, rolling the head to the left or right, or nodding forward or backward [137, 138, 139]. To evaluate the robustness of the aBMD measurements in the presence of minor positioning errors, phantom number 2 was subjected to several adjustments: it was nodded backward by 3°, moved upward by 2 cm while simultaneously being rolled to the right by 3°, and moved backward by 1 cm. These modifications were implemented while ensuring that the panoramic image remained interpretable (e.g., pulps of the teeth and mandibular canals were still visible). A control image was acquired under optimal positioning conditions.

6.2.2 Data acquisition

An experimental spectral photon counting panoramic system was used to image the phantoms. Specifically, the Planmeca Promax Mid system (Planmeca Oy, Helsinki, Finland) equipped with a DC-Vela detector (Varex Imaging Corporation, Salt Lake City, USA) was utilized. The DC-Vela is a photon-counting detector featuring 2 adjustable thresholds, charge-sharing correction, and a 0.75 mm cadmium telluride sensor layer. The acquisition parameters for this panoramic system are provided in Table 5.

Table 5: Spectral panoramic acquisition parameters.

source to image distance	60 cm
tube voltage	70 kVp
tube current	9 mA
acquisition time	18 s
dose-area product	72.1 mGycm^2
magnification	1.4
field of view (width×height)	0.6×15.41 cm^2
detector pixel size	0.1×0.1 mm^2
detector energy thresholds	15, 36 keV

A dual-source DECT scanner (SOMATOM Force, Siemens Healthineers, Erlangen, Germany) was employed to acquire dual-energy volumes. The MonoE + protocol was used to generate virtual monoenergetic images of the scanned phantoms. Knowing the energy of the input images is critical for subsequent processing, as will be discussed in the following subsection. The acquisition parameters for the DECT system are listed in Table 6, and the Qr69 kernel was chosen to achieve the

highest available spatial resolution.

Table 6: DECT acquisition parameters.

tube voltage	80/Sn150 kVp
tube current	552/397 mA
acquisition time	1 s
CTDIvol_{16}	49 mGy
dose length product	1360 mGycm
monoE+	50/190 keV
kernel	Qr69s/2
axial voxel size	0.39 mm
slice thickness	0.6 mm

6.2.3 Data processing

An algorithm for calibrating and decomposing data from a panoramic photon counting system was previously described [112]. Briefly, stationary calibration measurements were acquired using titanium and polyoxymethylene (POM) slabs of varying thicknesses. These materials were chosen because they are available in high purity and can be easily fabricated to the desired dimensions; titanium closely approximates the atomic number of calcium (and thus HAP), while POM has an effective atomic number similar to water and soft tissue [23]. The calibration measurements were used to generate virtual panoramic calibration images that match the dimensions of the panoramic acquisitions. A polynomial forward model was then calibrated via maximum likelihood estimation of model parameters for each pixel in the panoramic image. Subsequent panoramic images could be decomposed by applying regularized maximum likelihood estimation as if the image was a standard projection domain image [59].

A simulation framework for generating synthetic spectral panoramic images from single-energy CT acquisitions was described in previous work [80]. In this approach, the initial segmentation step was replaced by an image-based material decomposition of the DECT data. Two virtual monoenergetic images served as input and were transformed into basis material images via matrix inversion. For water and dentin as basis materials, the decomposed image $\boldsymbol{A}$ is given by:

$$\boldsymbol{A} = \begin{bmatrix} \mu_{\mathrm{ld}} & \mu_{\mathrm{lw}} \\ \mu_{\mathrm{hd}} & \mu_{\mathrm{hw}} \end{bmatrix}^{-1} \boldsymbol{I}, \tag{6.1}$$

where μ represents the linear attenuation coefficients of the basis materials (d for dentin and w for water) at the monoenergetic energies (l for low and h for high), and I is a $2 \times$ i matrix (with i representing the number of voxels). The upper row of I contains the linearized voxel values from the low energy monoenergetic volume, and the lower row contains the values from the high-energy volume. The resulting 2 material-decomposed images (the rows of $\boldsymbol{A}$) were then incorporated into the previously described framework. Briefly, the dental arch was determined semi-automatically, a series of projections through the dental arch was generated for each decomposed volume, and panoramic reconstruction was subsequently performed. The resulting panoramic equivalent thickness images (PETIs) were used to calculate the aBMD scores.

Anatomical noise was estimated as described previously, [80] by recording the line-integral path lengths of each pixel in every projection that contributed to a given output pixel in the synthetic

panoramic image. These recorded path lengths were then displayed as a histogram. Note that the synthetic image projections are noise-free, aside from the inherent noise of the DECT volume (which is minimal given the DECT dose and the post-processing applied). Adding noise to match experimental levels is not meaningful, as the synthetic images serve as the ground truth.

6.2.4 aBMD score calculation

A change of basis was applied to enhance the contrast between soft tissue and bone in the experimental materialdecomposed panoramic images. Various basis material combinations were evaluated to identify the pair that minimized residual bone signal in the soft tissue image. Dentin and soft tissue emerged as the optimal combination. For synthetic panoramic images, dentin is the standard output. The aBMD values were calculated by multiplying the dentin image by the density of dentin $1.95\,\mathrm{g/cm^3}$ [140].

For each ROI measurement site, 2 mean values were calculated: 1 for the mandible (excluding any overlap) and 1 for the background. The background mean was subtracted from the mandible mean to ensure comparability across different sites, as the background area in the hard tissue image is typically nonzero. Thresholding, combined with morphological operations (opening followed by closing), was used to segment the background and mandible and to exclude overlapping areas when necessary. The aBMD score for the Gammex inserts was calculated using the same method as for the anthropomorphic phantoms.

A linear fit between the synthetic and experimental mandible aBMD scores was performed with the intercept constrained to zero, based on the expectation that no intercept should exist between the 2 sets of values. The dataset comprised nine data points from 3 phantoms (left angle and both left and right bodies of the mandible). Given the small dataset, allowing a nonzero intercept would increase the risk of overfitting, and more complex relationships cannot be reliably estimated. The resulting fitting function was used to scale the experimental values to a magnitude comparable to the synthetic values.

6.2.5 Statistical analysis

Statistical analyses were performed using Python 3. Correlation coefficients and linear fits were computed using the NumPy package, while the root mean squared error (RMSE) was calculated using the scikit-learn package. The null hypothesis ($\rho = 0$) was tested by calculating the corresponding p-value with the SciPy package. The RMSE for the anthropomorphic head phantoms was calculated to assess the deviation of the experimental values from the synthetic values, which were considered the ground truth. Pearson's correlation coefficient was computed for the anthropomorphic aBMD scores to evaluate the linearity between the synthetic and experimental measurements. Additionally, the correlation coefficient was calculated for the Gammex 472 dual-energy phantom inserts to verify the linearity of the measured aBMD values.

6.3 Results

Figure 29 presents the experimental material decomposition panoramic images for anthropomorphic phantom number 2. In the dentin image (Fig. 29 A), prominent features include the maxilla, mandible, and teeth. However, the opposing mandible partially overlaps on both sides, and on the right side this overlap covers the mandibular angle, thereby precluding aBMD measurement at that location - a limitation observed in phantoms 1 and 3 as well. In the soft tissue image (Fig. 29 B), the respiratory tract is the dominant feature, appearing as darker grooves. The dentin component

exhibits a moderate negative correlation with the soft tissue image; for instance, the teeth and mandibular base appear darker relative to the surrounding areas.

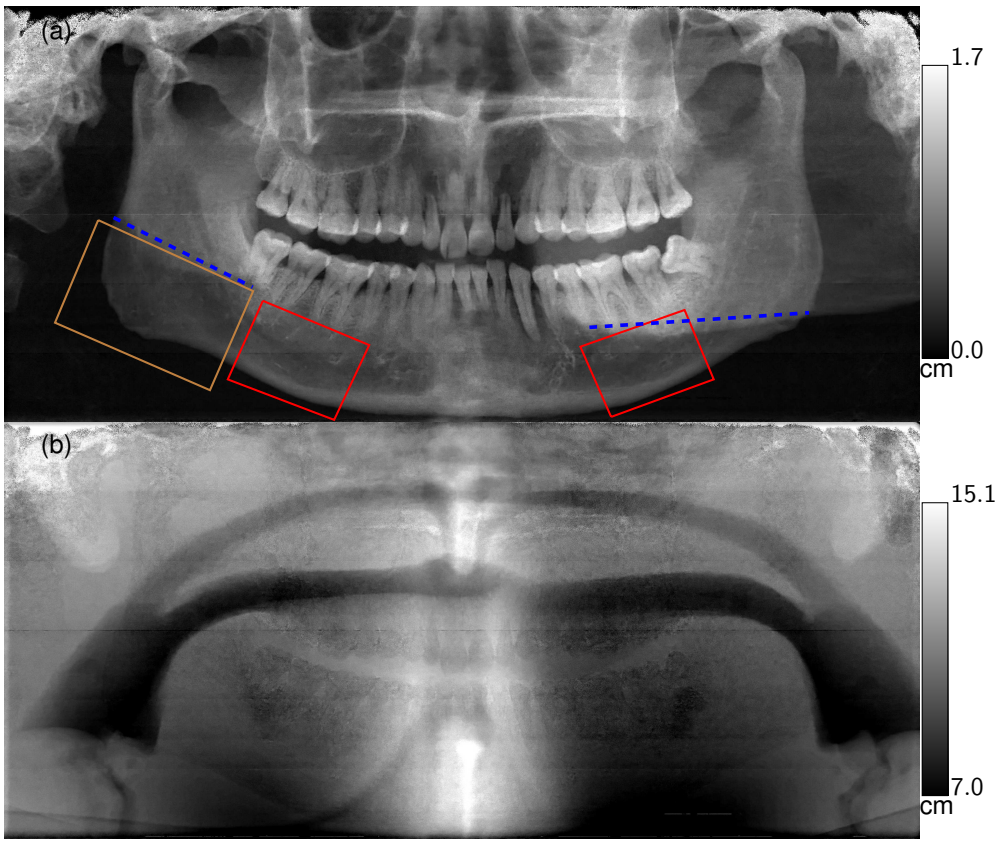

Figure 29: Fig. 2. A. Dentin component obtained from the spectral panoramic system. The rectangles highlight the area used for the aBMD measure-ment-red for the mandibular body and brown for the angle of the mandible. The blue dashed line highlights the lower border of the opposing mandible overlap region, which precludes measurement of the right mandibular angle. B. Soft tissue component obtained from the spectral panoramic system. [Adapted from [141]]

The synthetic panoramic images generated from DECT scans of anthropomorphic phantom number 2 are shown in Figure 30. As expected, the dentin component image (Fig. 30 A) is dominated by bony features, with the mandible and teeth prominently visible in the lower half. The overlapping region of the mandible appears as wedges toward the center of the image, extending to the roots of the mandibular teeth. In the soft tissue component image (Fig. 30 B), distinct features are visible: the respiratory tract appears as darker, arched lines, and the horizontal center-where more soft tissue is present-appears brighter than the edges. The dentin component imparts a very weak, inversely correlated signal to the soft tissue image (Fig. 30 B), which is subtle. Additionally, the overlap between the cervical spine and the mandibular body manifests as a high-value region in the dentin image (Fig. 30 A) and as a corresponding darker shape in the soft tissue image (Fig. 3B),

as indicated by the arrows. Similar darker regions are observed where other bony features overlap. Notably, enamel, unlike other hard tissues, induces a positively correlated signal in the soft tissue image, making it appear brighter than the surrounding tissues.

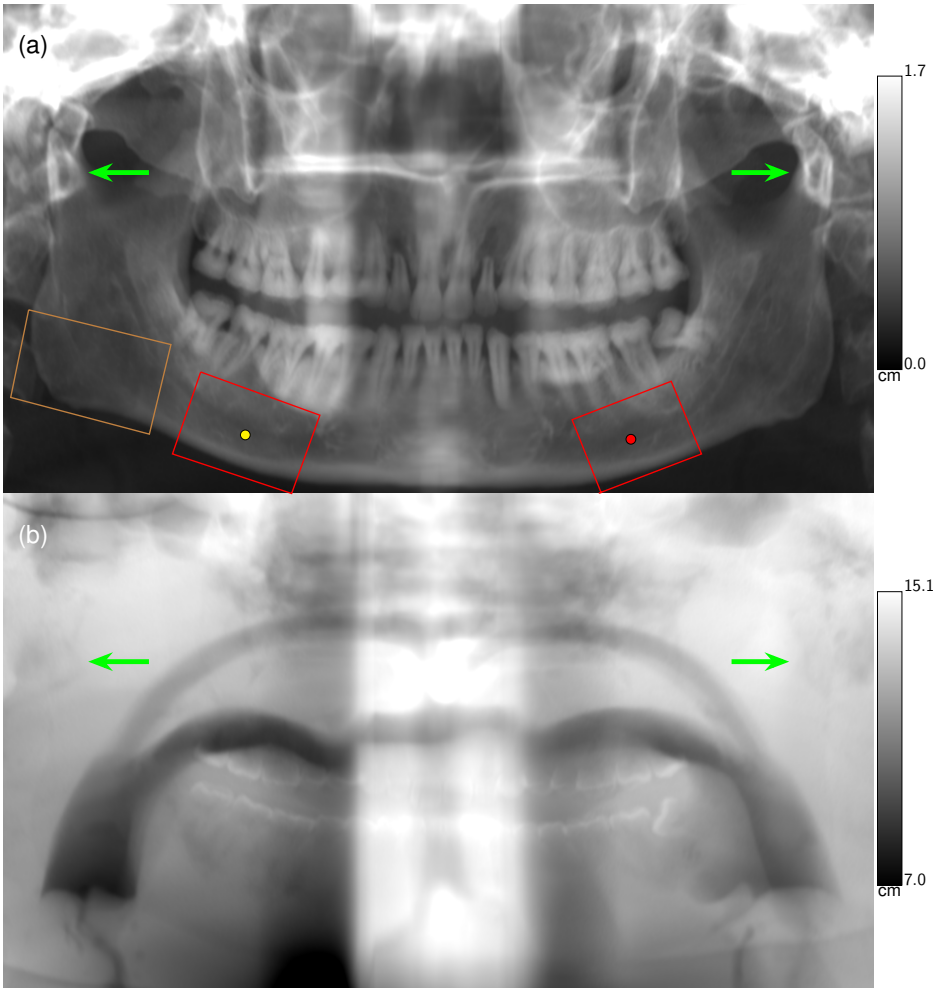

Figure 30: A. Dentin image generated from a dual-energy computed tomography (DECT) scan using the simulation framework. Rectangles denote the areas used for aBMD measurement: red for the mandibular body and brown for the mandibular angle. Yellow (left) and red (right) dots indicate the anatomical noise measurement points. B. Soft tissue image obtained from a DECT scan using the simulation framework. Two examples of the weak inversely correlated signal from the dentin component in the soft tissue image are indicated by green arrows. [Adapted from [141]]

The synthetic dentin component in Figure 30 A closely resembles its experimental counterpart in Figure 29 A in terms of feature contrast. For instance, the contrast among the mandibular base, the center of the mandibular body, and the roots of the teeth is similar in both images. However, the regions of mandibular overlap differ between the 2 images: in the synthetic image (Fig. 30A), these

areas are narrow and centrally located, whereas in the experimental image (Fig. 29 A) they are broader but less pronounced. This discrepancy likely arises from differences in the geometries used in the simulation compared to those in the experimental panoramic image generation. Nonetheless, the overall appearance of the teeth and mandible is consistent between the 2 sets of images

Figure 31 presents the aBMD measurements for the 3 anthropomorphic phantoms. The linear fit between the experimental and synthetic values yielded a slope of 0.956, indicating that the absolute values from both approaches are very similar. The largest deviation observed was 0.06 g/cm^2 (approximately 9% in relative terms), and the low RMSE indicates a strong linear correlation.

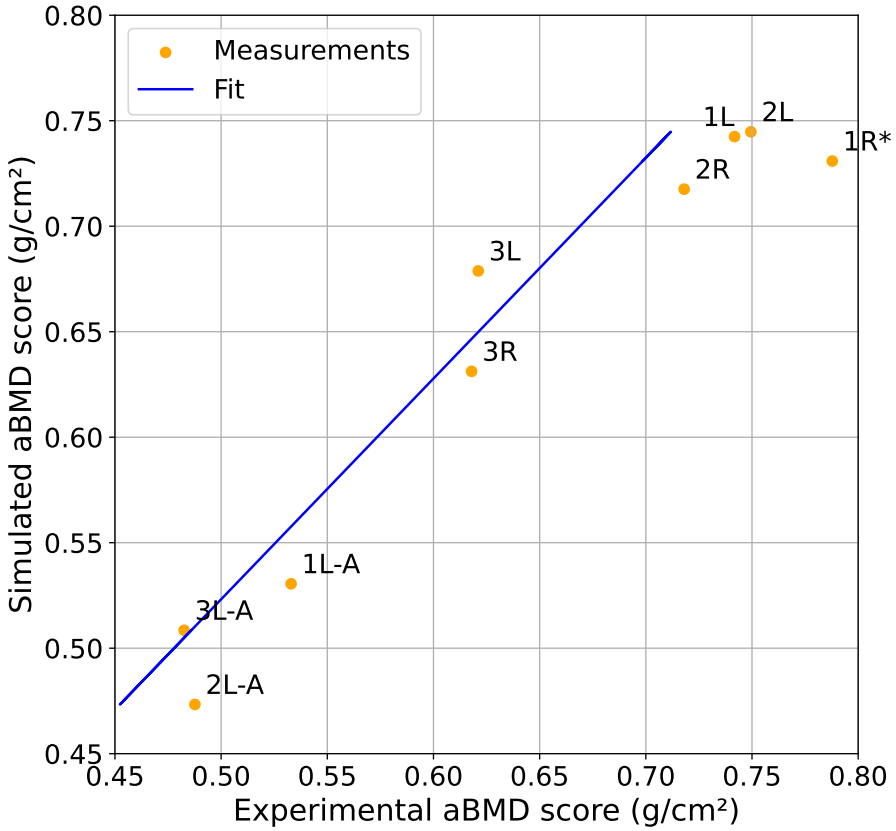

Figure 31: Areal bone mineral density (aBMD) scores for phantoms 1-3, with scores provided for both sides (left or right) of the mandibular bodies and left angles (denoted as -A) of the mandible. An asterisk (*) indicates cases with significant overlap from the opposing mandible; only the non-overlapping area was used. Pearson correlation coefficient r = 0.969($P < 0.001$) and RMSE = 0.0292 g/cm^2. [Adapted from [141]]

The aBMD scores of phantom 2 at different positions are shown in Table 7. The left side RMSE is almost equal to the RMSE of Fig. 31 i.e. the error did not increase when positioning errors were present. The RMSE of the right side is higher (versus Fig. 31) because of a single outlier, which ROI area reduction by the partial mandible overlap, in this case, could explain.

The aBMD scores of phantom 2 at different positions are shown in Table 3. The RMSE on the

left side was nearly identical to that shown in Figure 31, indicating that minor positioning errors did not increase the error. However, the RMSE on the right side was higher compared to Figure 31, which can be attributed to a single outlier-likely resulting from a reduction in the ROI area due to partial mandible overlap.

Table 7: Areal bone mineral density (aBMD) scores for the mandibular body of phantom number 2 with different positioning errors. *Denotes significant overlap from the opposing mandible. Only the non-overlapping area was used.

phantom position	left (g/cm^2)	right (g/cm^2)
simulated, optimal	0.75	0.72
control, correct	0.79	0.74
nod backwards by 5°	0.74	0.81*
moved up by 2 cm AND		
roll to the right by ≈ 3°	0.75	0.72
moved back by ≈ 1 cm	0.78	0.75
mean of experimental	0.764	0.752
RMSE vs. simulated	0.0296	0.0474

The results of the aBMD linearity test are shown in Fig. 32. The experimental aBMD scores deviate by a maximum of 0.13 g/cm^2 from what is predicted by the fit. Overall, the experimental scores follow the linear fit closely, as the correlation coefficient is close to 1. The aBMD scores covered by the linearity test range from 0.0 to 2.7 g/cm^2, while the anthropomorphic phantoms (Fig. 31 and Table 7) only range from 0.5 to 0.8 g/cm^2.

The results of the aBMD linearity test are shown in Figure 5. The experimental aBMD scores deviated by at most 0.13 g/cm^2 from the values predicted by the linear fit, and the correlation coefficient was nearly 1, indicating excellent linearity. It is noteworthy that the aBMD scores evaluated in the linearity test spanned a broader range (0.0 to 2.7 g/cm^2) compared to those from the anthropomorphic phantoms (0.5 to 0.8 g/cm^2) as shown in Fig. 31 and Table 7).

Figure 33 presents the anatomical noise histograms. The histogram counts at both measured points were very similar, indicating that the area used for aBMD measurements was anatomically stable; that is, the line-integral path lengths remained consistent regardless of angle or location within that area. Thus, the aBMD scores were not significantly affected by minor geometric variations or patient positioning errors.

6.4 Discussion & conclusion

This study demonstrated a method for generating mandibular aBMD scores using an experimental spectral panoramic imaging system. The method was validated by crossverifying the results against gold-standard DECT data using a modified panoramic simulation framework. The visual similarity, consistent contrast, low RMSE, and high correlation between experimental and synthetic results collectively indicate that the aBMD scores obtained are reliable. Furthermore, the anatomical noise histograms in Figure 33 and the aBMD scores in Table 7 suggest that the method is robust against minor positioning or orientation errors.

The main results, shown in Figures 31 and 32, exhibit very high correlation coefficients with P-values < 0.001, indicating statistical significance despite some imperfections in the regression. The

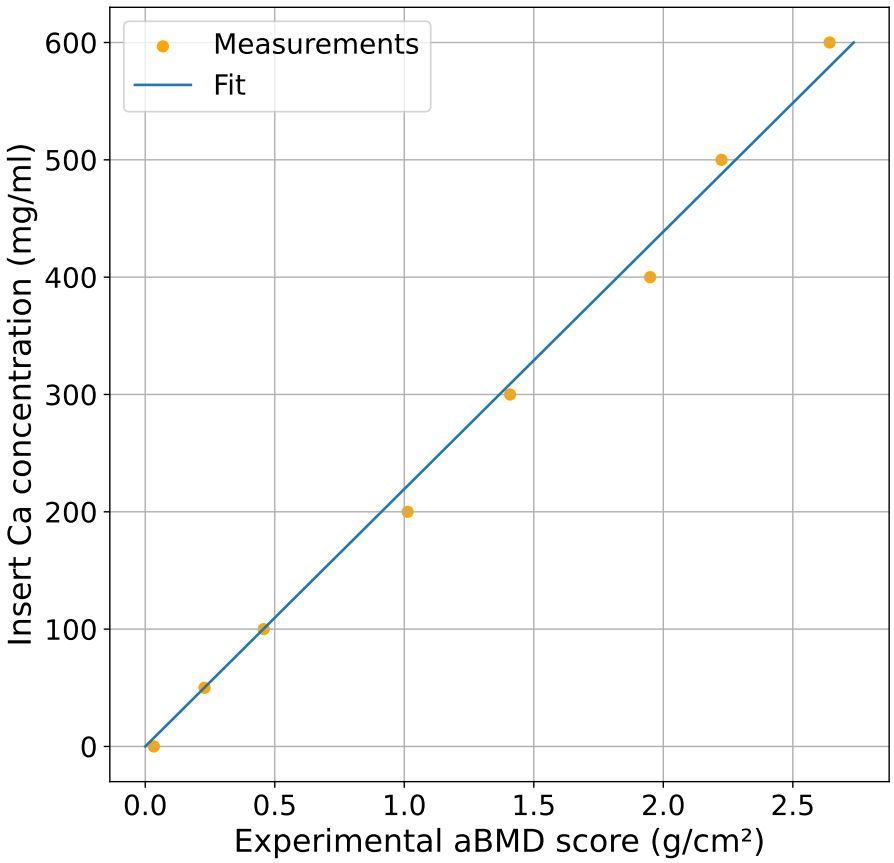

Figure 32: Gammex calcium (Ca) inserts compared to the experimental areal bone mineral density (aBMD) scores, along with a linear fit. A Ca concentration of 0mg/mL corresponds to the solid water insert. Pearson correlation coefficient r = 0.998($P < 0.001$). [Adapted from [141]]

correlation in Figure 31 is slightly lower than that in Figure 32, which can be attributed to the fact that, if the noise magnitude is similar for both datasets (due to matching dose and attenuation), the relative deviation will be more pronounced when the range of values is narrower, as seen in Figure 31.

One discrepancy between the experimental and synthetic images is that enamel produces a negatively correlated soft tissue signal in the experimental image, similar to other bony tissues, but a positively correlated signal in the synthetic image. The positive correlation observed for enamel is likely an artifact, since it is counterintuitive that the most attenuating tissue would generate a positive signal on another spectral channel. A probable explanation is a partial volume effect, whereby the thin dentin layer's attenuation is blended with the attenuation of the surrounding plastic. Confirmation of this effect would require a high-resolution spectral imaging system, such as a photon counting CT [32].

The overlap of the opposing mandible in the experimental images introduced challenges in determining aBMD scores, particularly by preventing measurements at the right mandibular angle.

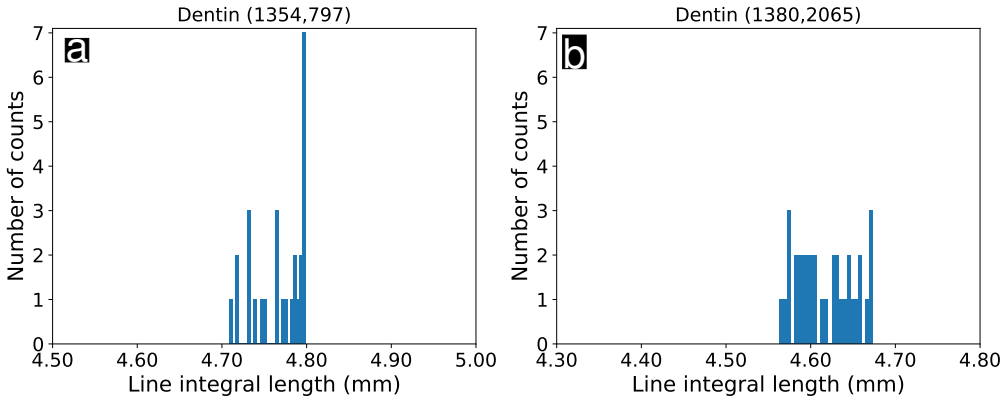

Figure 33: Anatomical noise histograms for the synthetic dentin image in Fig. 30 (a), with pixel indices in the label. The yellow point in Fig. 30 corresponds to histogram (a) and red point to histogram (b). Both histograms have counts only in a very narrow line integral length range. [Adapted from [141]]

This overlap is most likely due to suboptimal detector mounting. Future improvements in detector mounting are expected to reduce the overlap region, ensuring that it does not encroach upon the aBMD measurement area. Despite this limitation, the aBMD scores were in good agreement overall.

The ROIs used for aBMD measurements in Figure 31 and Table 7 were selected manually, which may lead to slight mismatches between the experimental and synthetic images and introduce potential errors. Automatic segmentation and registration of the mandible could mitigate this issue [142]. Additionally, quantum noise is amplified during the decomposition process [143]. Although regularization reduces this noise, it does not completely eliminate it, contributing some variance to the results.

Ideally, scaling the experimental aBMD scores to match the synthetic ones would not be necessary. However, in the experimental setup, a change of basis is required to convert calibration materials into physically meaningful materials (soft tissue and dentin). This difference in generating the synthetic and experimental dentin images is a potential source of error in comparing aBMD scores. If DECT values are accepted as the ground truth, tuning the basis vector energies might improve the match between experimental and synthetic results. Nevertheless, perfect regression between the 2 datasets is unlikely, as the imaging systems and settings differ - one employing image-domain decomposition and the other using projection-domain decomposition-and they are subject to varying degrees of scatter.

In lumbar spine DXA measurements, a reference score is established based on age, sex, and body mass index[144]. To determine whether a similar scaling approach is necessary for spectral panoramic mandibular aBMD scores, an in vivo patient study with a substantial sample size is warranted.

Despite the limitations discussed, the synthetic and experimental panoramic images show strong agreement. This suggests that it is technically feasible to employ spectral panoramic imaging for osteoporosis and periodontal disease screening via aBMD measurements without increasing patient radiation exposure. Additionally, orthodontics could benefit from the ability to measure aBMD scores of specific teeth and surrounding tissues before and after implant placement, although mandible overlap may pose challenges in certain cases. Given that panoramic imaging is the most common

extraoral dental radiological examination, [5] the clinical potential of this approach is substantial.

7 Effect of a prototype 2-dimensional antiscatter grid on image quality obtained with a dental cone-beam computed tomography scanner

In this chapter, the feasibility of improving dentomaxillofacial image quality using 2D-grid is explored. With the advancements of additive metal manufacturing, 2D-grids of suitable dimensions are now available for dental scanners. We build on a previous work on how correct the residual scatter, which is required to prevent artefacts induced by the grid. Various anthrophomorphic head and other phantoms are imaged with a dental scanner fitted with a 2D-grid.

The text and figures have been published as:

- B Li, V Somerkivi, et al. Effect of a prototype 2-dimensional antiscatter grid on image quality obtained with a dental cone-beam computed tomography scanner. Imaging Science in Dentistry, vol. 55, no. 1. 2025

Slight modifications have been made to incorporate the text and figures better into this doctoral thesis.

7.1 Introduction

Cone-beam computed tomography (CBCT) is a widely used imaging method in dentistry. In a CBCT scan, an X-ray source and a detector rotate around the patient to collect 2-dimensional (2D) X-ray projections, which are then reconstructed into high-resolution volumetric images. These images provide high diagnostic accuracy and assist in treatment planning. Despite the promise of dental CBCT, increasing image quality and quantitative accuracy remains a primary research area. In addition to qualitative improvements in tissue visualization and diagnostic performance, higher CT number accuracy is desired to extract quantitative information from dental CBCT images. Increased quantitative accuracy may expand the utility of dental CBCT in various applications, such as extracting bone density for dental implant placement, planning surgical tooth extractions, evaluating dental bone grafts, assessing trauma, and planning reconstructive or corrective jaw surgery. Another application that would benefit from improved quantitative accuracy is the generation of the 3-dimensional (3D) models used for surgical planning and fabrication of surgical guides based on CBCT images, which rely on accurate representation of tissue-specific CT numbers. [145, 146, 3, 147, 148]

To improve CBCT image quality, numerous technical challenges must be addressed, including the presence of artifacts from metallic objects, motion, beam hardening, image noise, and scatter. [3, 149] Among these issues, scattered radiation represents one of the most fundamental causes of image quality degradation in CBCT. [150, 151] Compared to a conventional multidetector CT system with a fan-shaped X-ray beam, a CBCT system employs a larger cone of X-rays in the craniocaudal direction, increasing the fluence of scattered X-rays. In turn, scatter degrades contrast, increases image artifacts, and reduces CT number accuracy, which compromises the representation of tissue densities in CBCT images. Numerous methods have been investigated to address the scatter problem. The most common approach is algorithmic scatter correction, in which the scatter signal bias is corrected after the X-ray detector has captured scatter. Most scatter correction methods employ a model to estimate and correct the scatter bias from the CBCT raw data and subsequently compensate for the scatter signal. [152, 153, 154] However, suboptimal modeling of scatter conditions may lead to misestimation of scatter intensity and incomplete scatter correction. Another approach for scatter suppression is the use of scatter rejection devices such as antiscatter grids, which prevent

scattered X-rays from reaching the detector. Conventional radiographic antiscatter grids employ a 1-dimensional array of radiopaque septa that absorb incident scattered X-rays. Although conventional antiscatter grids reduce scatter intensity, their performance is insufficient to achieve highly accurate CT numbers in CBCT images. [155, 156] In addition to physics-based scatter correction and rejection techniques, image restoration methods have also been investigated, in which the effects of scatter are removed from CBCT images via heuristic and machine learning approaches. [155, 157, 158, 159]

In the present work, a novel scatter suppression approach was investigated for dental CBCT systems. A prototype 2D antiscatter grid (hereafter termed the " 2 D grid") was developed, composed of a 2D array of tungsten septa placed on the X-ray detector, with each septum aligned toward the X-ray source. Compared to conventional radiographic antiscatter grids with a 1-dimensional (1D) array of radiopaque septa, 2D grids can provide significantly improved scatter rejection performance and superior primary X-ray transmission. [160, 161] While 2D grids have been shown to improve CBCT image quality in human torsos, they have not been investigated in the context of dental CBCT imaging. [162, 163, 164] Due to the smaller X-ray field of view (FOV), shorter source-to-detector distance, and smaller anatomical regions imaged with dental CBCT systems, the scatter characteristics and resulting image quality improvements may differ from those in CBCT systems designed for imaging the torso. Hence, this study investigated the effect of 2D grid-based scatter suppression on dental CBCT image quality.

7.2 Materials and Methods

7.2.1 2D grid prototype

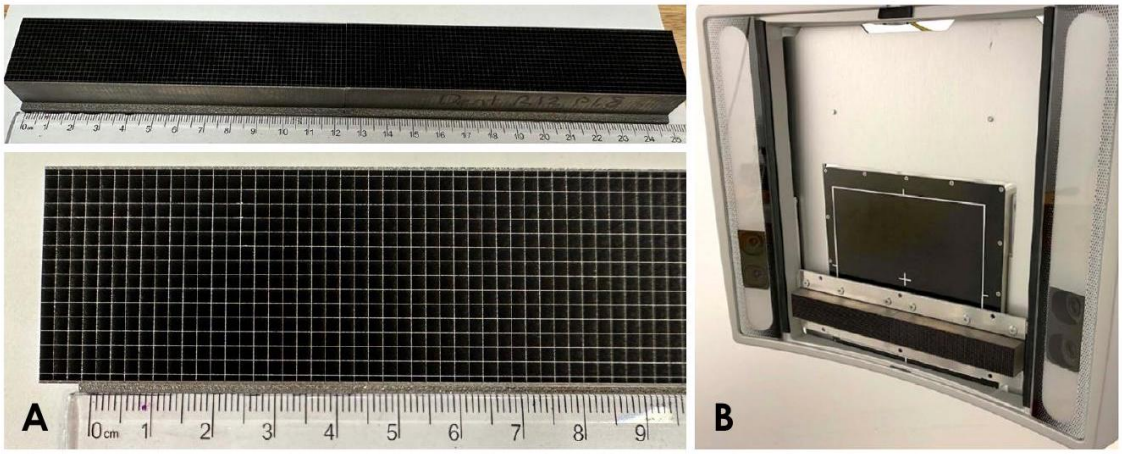

Figure 34: A. Photo of the tungsten 2-dimensional (2D) antiscatter grid used in the experiments. B. 2D grid prototype as mounted on the X-ray detector. [Adapted from [165]]

The prototype 2D grid (M2 Technologies, Denver, CO, USA) had a grid pitch of 1.8 mm , a grid ratio of 12 , and a wall thickness of 0.1 mm (Fig. 34 A). It was 3 cm wide in the axial direction and 25 cm long in the transverse direction of the CBCT system. Its grid walls were aligned towards the X-ray source in the source-detector geometry of the Planmeca Viso G5 CBCT system (Planmeca Oy, Helsinki, Finland). The grid was directly mounted on the X-ray detector (Fig. 34 B). The prototype was manufactured from pure tungsten using a powder bed laser melting process, with air

in the spaces between the tungsten. Tungsten was chosen for its structural rigidity and superior X-ray attenuation properties compared to lead. Moreover, tungsten is well-suited for the powder bed laser melting process, which enables the fabrication of 2 D grid structures with 0.1 mm-thick walls. Although lead is commonly used in conventional antiscatter grids, it is suboptimal for fabricating 2D grid structures using laser sintering-based additive manufacturing processes.

While the 2D grid rejects the vast majority of scattered X-rays, a small fraction still passes through and adversely affects image quality. This residual scatter was corrected using a measurement-based scatter correction method, termed Grid-based Scatter Sampling (GSS).[163, 166, 167] The GSS method utilizes the 2D grid itself as a scatter measurement device to directly measure and correct the remaining scatter in raw projections. Prior reports have demonstrated that the GSS method can accurately measure and correct residual scatter transmitted through the 2D grid. [163, 166, 167] In this work, the GSS method was optimized and adapted for the 2 D grid prototype and the dental CBCT system under investigation.

7.2.2 CBCT imaging experiments

The CBCT experiments were performed using a Planmeca Viso G5 dental CBCT system. While the 2D grid covered only a small section of the detector (Fig. 34 B), the X-ray FOV covered the full active area of the detector to mimic scatter conditions in a dental CBCT scan. CBCT system and scan parameters are summarized in Table 7.2.3. The jaw protocol was used to acquire the data. The frames were acquired in an offset geometry setting (Fig. 35 A). With this setting, the detector and the tube are offset toward the same side and rotate 360° around the object, such that one side at a time is visible to the detector. This allows a larger object to be reconstructed than under a symmetric geometry setting.

The effect of the 2D grid on CBCT image quality was evaluated in numerous phantom experiments, with the phantoms summarized in Table 7.2.3. For each phantom, 2 sets of experiments were performed: with and without the 2 D grid. The no-grid and 2D-grid CBCT scans were acquired using identical dose and scan parameters, as summarized in Table 7.2.3. Projections acquired with the 2 D grid were corrected for residual scatter using the GSS method. The system's default software-based scatter correction was applied to all datasets without the 2D grid. The correction algorithm attempts to remove smooth, low-frequency signal, also called cupping, from the soft tissue part of an image volume after reconstruction. Water-equivalent beam hardening correction was applied to both the 2D-grid and no-grid CBCT scans, and the images were subsequently reconstructed using the CBCT system software. Filtered back projection was applied to reconstruct all images.

7.2.3 Effect of the 2D grid on scatter suppression and CBCT image quality

Scatter intensity reduction performance was evaluated in CBCT projections of an anthropomorphic dental phan-

Table 7.2.3: Summary of imaging acquisition parameters

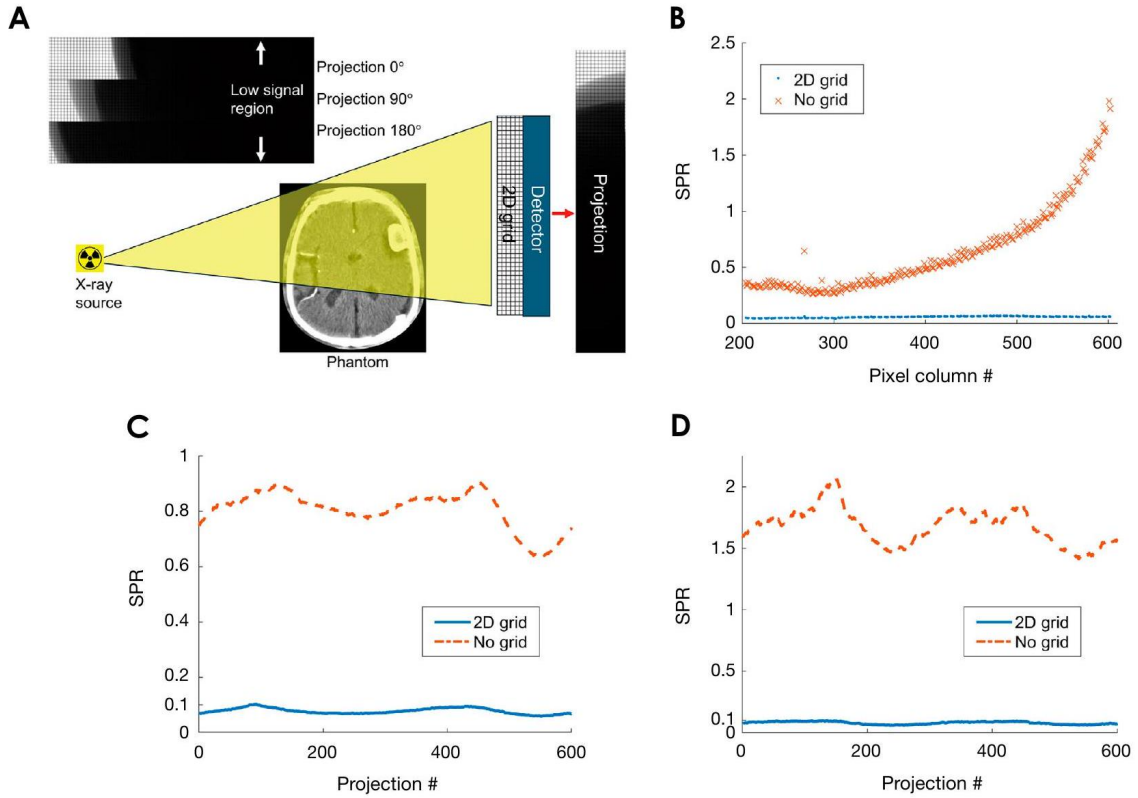

Figure 35: A. Diagram of the imaging system with the 2-dimensional (2D) grid and 3 sample projections of the anthropomorphic dental phantom used for scatter-to-primary ratio (SPR) calculations. B. SPR in CBCT projections acquired with the 2D grid in place. The average SPR of each pixel column in one of the projections is shown. C. Average SPR of the full phantom region. D. Average SPR in the low signal, or highly attenuating, region of each projection. [Adapted from [165]]

Parameter name	Value
Tube voltage (kV)	100
Exposure (mAs)	160
Dose-area product $\left(\text{mGycm}^2\right)$	289
Voxel size, dental $\left(\text{mm}^3\right)$	$0.15 \times 0.15 \times 0.15$
Voxel size, brain $\left(\text{mm}^3\right)$	$0.5 \times 0.5 \times 0.5$
Frame field of view $\left(\text{cm}^2\right)$	16×16
Detector pixel pitch $\left(\text{mm}^2\right)$	0.139
Pixel binning	2×2
Source-to-imager distance (cm)	70
Source-to-object distance (cm)	48.6

tom. The reduction in scatter intensity was characterized by the scatter-to-primary ratio (SPR) in projections acquired with and without the 2D grid. Raw CBCT projections of a phantom, Projphan , contain both primary and scattered X-rays. When CBCT projections are acquired with

a 2D grid, a primary-only projection, Proj_{GSS}, was computed by correcting for scatter using the GSS method. Hence, scatter intensity (S) and SPR were calculated as follows:

$$S = \text{Proj}_{phan} - \text{Proj}_{GSS} \tag{1}$$

$$SPR = \frac{\text{Proj}_{phan} - \text{Proj}_{GSS}}{\text{Proj}_{GSS}} \tag{2}$$

This approach was also used to estimate SPR in CBCT projections acquired without a 2 D grid, since the primary signal intensity was the same in the 2 D -grid and no-grid CBCT scans.

CBCT image quality was evaluated both qualitatively and quantitatively. The qualitative assessments focused on the image artifact reduction performance of the 2 D grid, and they complemented and confirmed the quantitative analyses. For the quantitative evaluations, CBCT scans of each phantom acquired with and without the 2D grid were first rigidly co-registered; subsequently, Hounsfield unit (HU) consistency and contrast were analyzed. Image contrast was calculated by determining the difference between the target and background ROIs.

The image reconstruction process yielded a 3D map of linear attenuation coefficients. The attenuation coefficient for each voxel was converted to an HU value using the standard HU calculation method: [168, 169]

$$HU(i,j,k) = \frac{(\mu(i,j,k) - \mu_{water})}{\mu_{\text{water}}} \times 1000 \tag{3}$$

where μ is the attenuation coefficient of a voxel located at i, j, k in the 3D volume and μ_{water} is the attenuation coefficient of water obtained from a calibration phantom. With this linear transformation, air corresponds to -1000 HU and water to 0 HU . The same HU calculation method was used for all imaging experiments.

Table 7.2.3. Summary of phantoms used in imaging experiments

Phantom #	Phantom description
1	Dental portion of the head X-ray phantom (Erler-Zimmer GmbH, Lauf, Germany)
2	Sedentex image quality evaluation phantom, with calcium-containing inserts (Leeds Test Objects, North Yorkshire, UK)
3	Gammex DE calcium inserts (Sun Nuclear, FL, USA)
4	Brain portion of the CT Torso Phantom CTU41 (Kyoto Kagaku, Kyoto, Japan)

First, HU uniformity performance was evaluated in CBCT images of a dental-focused anthropomorphic dental phantom (Erler-Zimmer GmbH, Lauf, Germany). Fourteen teeth were segmented from the co-registered images with and without the 2D grid using the MATLAB Image Segmenter (MathWorks, Natick, MA, USA). The ROIs for image analysis were the entire segmented teeth. An HU histogram of each segmented tooth was calculated, and the mean HU was analyzed to assess tooth-to-tooth HU variation. Bony anatomy contrast was evaluated using the Sedentex CT IQ phantom (Leeds Test Objects, North Yorkshire, UK) with 4 calcium-containing cylinder modules from the Gammex 472 phantom (Sun Nuclear, Melbourne, FL, USA) inserted in an acrylic cylinder 160 mm in diameter. The signal difference between the high-contrast inserts and the acrylic background was computed to compare the bony anatomy contrast in 2D-grid and no-grid CBCT images.

The ROIs for the calcium cylinders were circular, with a diameter equal to half the diameter of the cylinders (approximately 17 mm). A similarly sized circular ROI was used for the acrylic background near the calcium contrast inserts.Due to the lack of soft tissue contrast in the other dental phantoms available at the time of this study, soft tissue contrast performance was evaluated using the brain portion of the CT Torso Phantom CTU41 (Kyoto Kagaku, Kyoto, Japan). For simplicity, this phantom will be referred to as the "brain phantom" for the remainder of this paper. ROIs were selected to calculate signal differences for the gray matter/ventricle and gray matter/hemorrhage regions. HU uniformity was also evaluated in the brain phantom. The skull and brain regions of the phantom were segmented by thresholding. HU uniformity in soft tissues was evaluated by placing 9 ROIs across the brain soft tissue region, while HU uniformity in bony tissues was evaluated by placing 16 ROIs across the brain skull region. The standard deviation and maximum deviation with respect to the mean HU across all ROIs were investigated. The shape and location of the ROIs are shown in the figures in the Results section.

7.3 Results

7.3.1 Scatter-to-primary ratio

Example CBCT projections of the anthropomorphic dental phantom acquired with the 2D grid, along with the 2D

grid imaging diagrams, are presented in Fig. 35 A. Without the 2 D grid, SPR values varied between 0.5 and 2 , with the highest values observed in the central section of the phantom where the X-ray beam exhibited the greatest attenuation. With the 2 D grid in place, SPR values fell below 0.1 across the entire phantom projection (Fig. 35 B). On average, the 2 D grid reduced SPR by a factor of 10 in each projection (Fig. 35 C). In highly attenuating regions of the projections, SPR was reduced by up to a factor of 20 on average (Fig. 35 D).

7.3.2 HU uniformity and image contrast improvements

Images of the dental phantom acquired with and without the 2D grid are provided in Figures 36 A and 36 B. While both images appear qualitatively similar, the CT numbers for dentin were substantially higher in images acquired with the 2D grid due to X-ray scatter suppression. The mean HU values of all teeth were 1718 HU with the 2D grid and 1227 HU without it. HU values also varied as a function of tooth location, as seen in segmented images (Figs. 36 C and 36 D). HU histograms of teeth #2 (maxillary right second molar), #6 (maxillary right cuspid), and #9 (maxillary right central incisor) under the Universal Numbering System are shown in Figure 37. In images acquired without the 2D grid, the HU histograms exhibited large differences among teeth. With the 2D grid, these differences were significantly reduced due to robust scatter suppression. Specifically, the standard deviation of HU values among teeth decreased from 166 to 43 HU , the maximum deviation from the mean decreased from 275 to 116 HU , and the maximum difference among teeth decreased from 510 to 146 HU .

Bony anatomy contrast was evaluated using calciumcontaining inserts placed in the Sedentex phantom. Contrast increased linearly as a function of calcium concentration for both 2D-grid and no-grid configurations (Fig. 40). For a 600 mg/mL calcium insert, the measured contrast was 1782± 143 HU in images acquired with the 2D grid and 1345± 117 HU in images acquired without it.

Figure 39 shows images of the brain phantom captured with the dental CBCT system. The contrast between structures such as ventricles and hemorrhage, relative to the background brain parenchyma, appeared noticeably greater in images acquired with the 2 D grid. CT number line

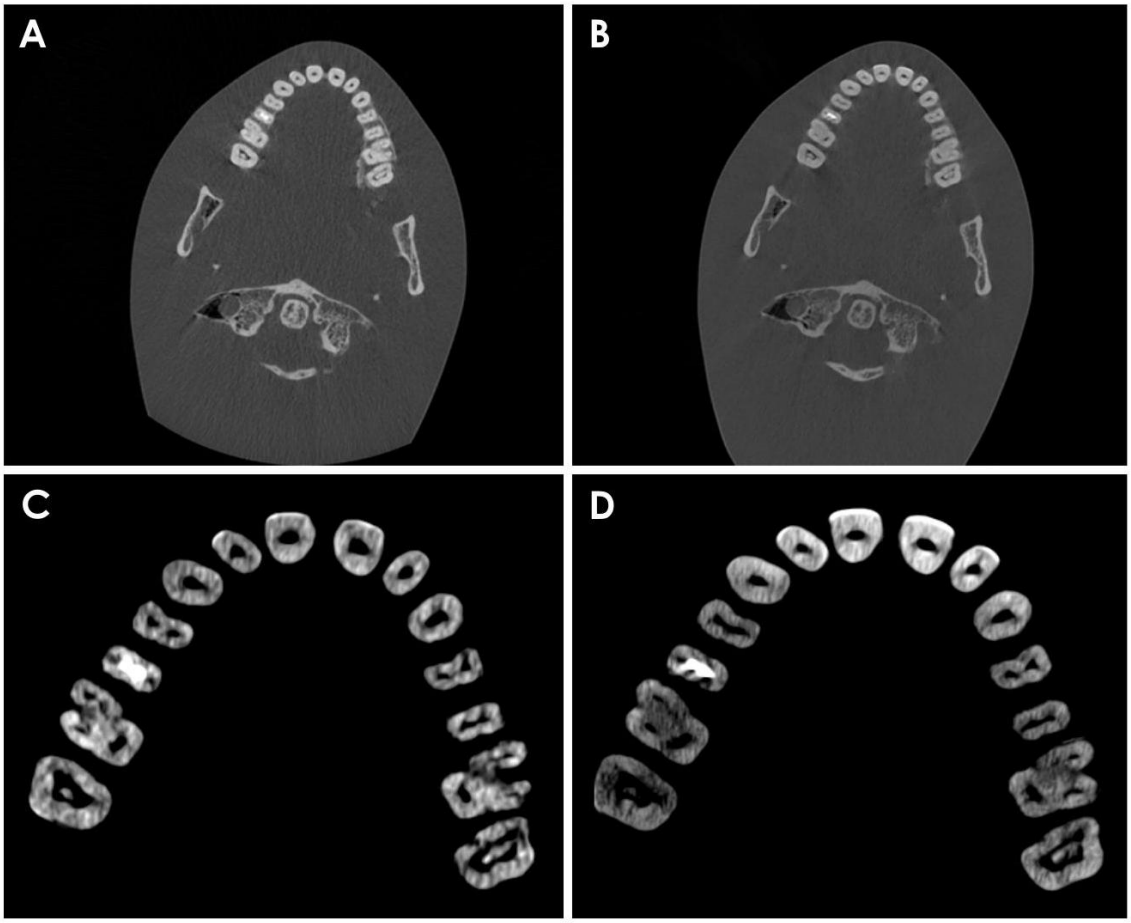

Figure 36: A. Axial image with the 2-dimensional (2D) grid (window width/level=4000/1000). B. Axial image without the grid (window width/ level = 4000/1000). C. Magnified section of teeth with the 2 D grid (window width/level = 1000/1800). D. Magnified section of teeth without the grid (window width/level = 1000/1300). [Adapted from [165]]

profiles in Figure 7 also demonstrate superior soft tissue contrast with the 2D grid. Quantitatively, soft tissue contrast increased from $19 - 62$HU to $27 - 89$HU, corresponding to an average increase of 48% (Table 7.4).

Figure 41 illustrates the effect of the 2D grid on shading artifacts. In the region indicated by the red box in Figure 41 A, significant shading artifacts were observed near the skull in images acquired without the 2D grid (Fig. 41 B), and these artifacts were markedly reduced in images captured with the grid (Fig. 41 C). Similar effects are also evident in another image slice (Figs. 41 D-F). These observations were further supported by the HU uniformity among ROIs placed in the brain parenchyma (Fig. 42). When the 2D grid was applied, the standard deviation of ROI mean HU values decreased from 4.8 to 2.4 HU . HU uniformity in the ROIs positioned in the skull region also improved upon application of the 2D grid (Fig. 43), with the standard deviation of ROI mean HU values decreasing from 208 to 104 HU.

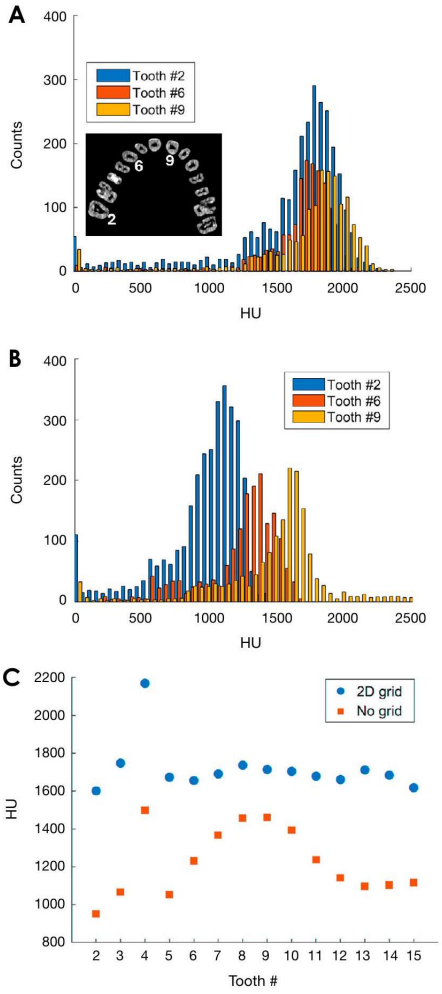

Figure 37: Sample Hounsfield unit (HU) histograms of the segmented teeth in images acquired with (A) and without (B) the 2-dimensional (2D) grid. The histograms represent the maxillary right second molar (#2), maxillary right cuspid (#6), and maxillary right central incisor (#9). C. Mean HU value of each segmented tooth based on the Universal Numbering System. [Adapted from [165]]

7.4 Discussion

This study investigated the effect of robust scatter suppression on CBCT image quality in a dental CBCT system. The prototype 2D grid demonstrated high efficacy in rejecting scattered X-rays in dental CBCT geometry, achieving a reduction in SPR by a factor of 10 to 20 in large-FOV CBCT scans.

Table 7.4. Soft tissue contrast across ventricles and hemorrhage in the anthropomorphic brain phantom (unit: Hounsfield unit)

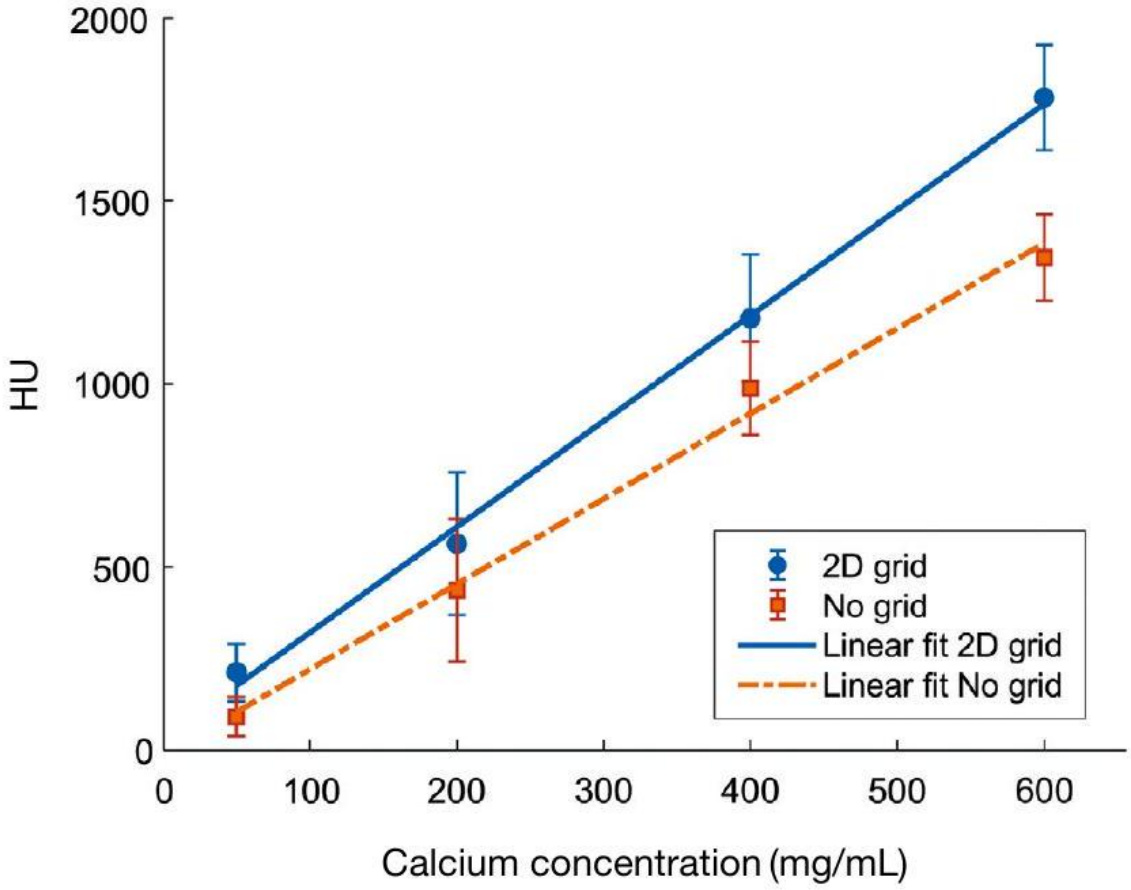

Figure 38: Hounsfield unit (HU) values of calcium-containing inserts. 2D: 2-dimensional. [Adapted from [165]]

ROI name	2D grid contrast	No grid contrast
Ventricle 1	36 ± 7	23 ± 5
Ventricle 2	27 ± 7	19 ± 5
Hemorrhage	89 ± 9	62 ± 8

ROI: region of interest, 2D: 2-dimensional

In all phantom experiments, the use of the 2 D grid resulted in consistent and uniform HU values for a given material type, and contrast was substantially improved, particularly in bony anatomy. These findings indicate that image artifacts, contrast loss, and HU degradation caused by scatter are significantly reduced by the 2 D grid under the same X-ray exposure level as scans captured without the grid. This effect occurs because in projections, bony tissue regions often exhibit a higher SPR than soft tissue regions. Bony anatomy strongly attenuates primary X-rays due to its higher atomic number and density, while the scatter signal remains relatively uniform. Consequently, the rapid reduction of primary signal in bony regions yields a higher SPR and greater

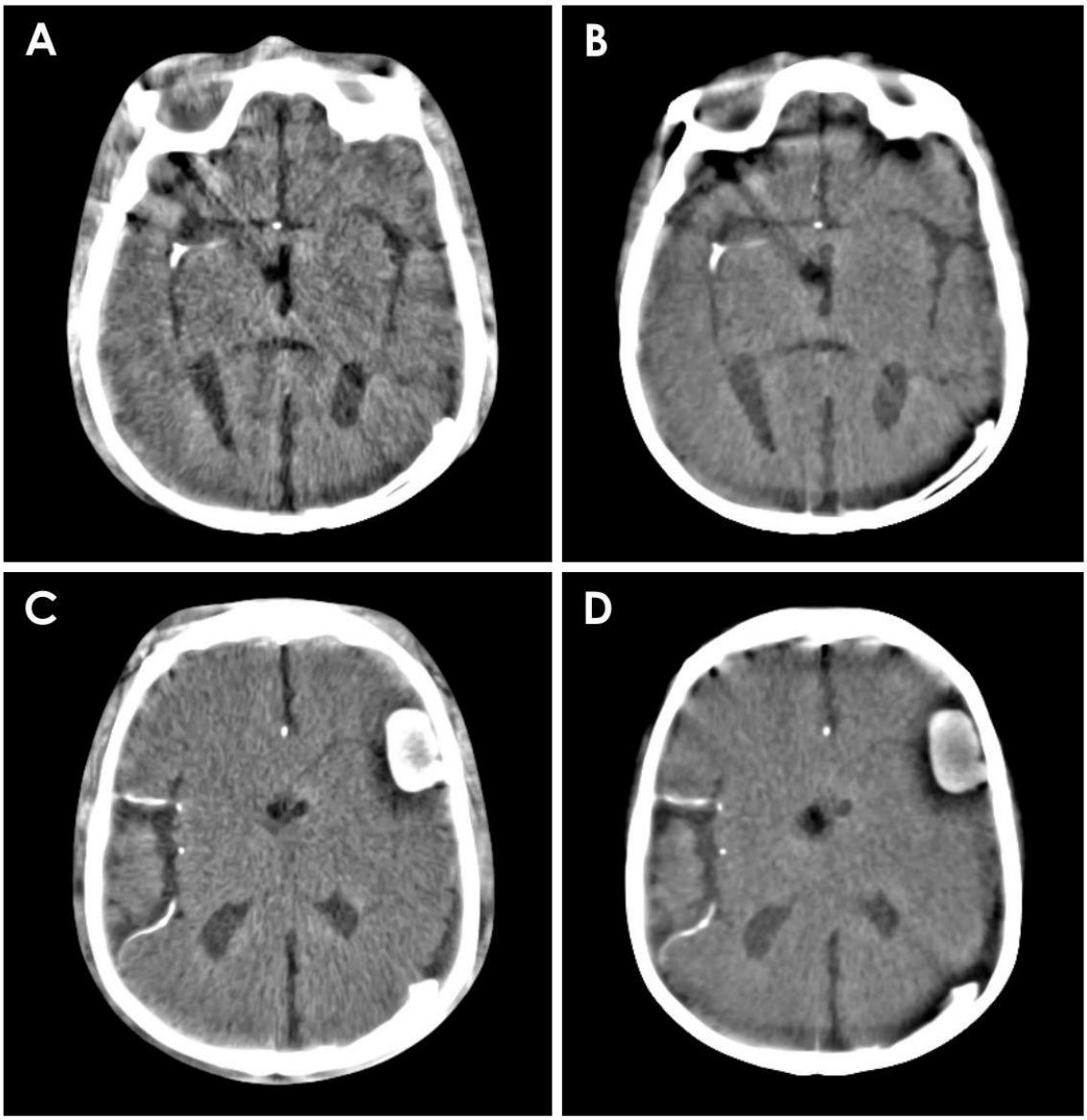

Figure 39: Brain phantom image slices acquired with (A) and without (B) the 2-dimensional (2D) grid. Image slices depict the hemorrhage acquired with (C) and without (D) the 2D grid. Display window width/level: 100/60. [Adapted from [165]]

CT number degradation. [153, 170] When scatter is effectively suppressed, improvements in CT number consistency are more pronounced. Although the scatter transmission properties of the 2 D grid do not depend on the exposure level, the rejection of scatter combined with exposure level variations may impact image noise characteristics. The removal of scatter improves contrast in CBCT images, but it also increases noise due to the reduced overall X-ray fluence reaching the detector. The interplay between increased noise resulting from reduced scatter and exposure level

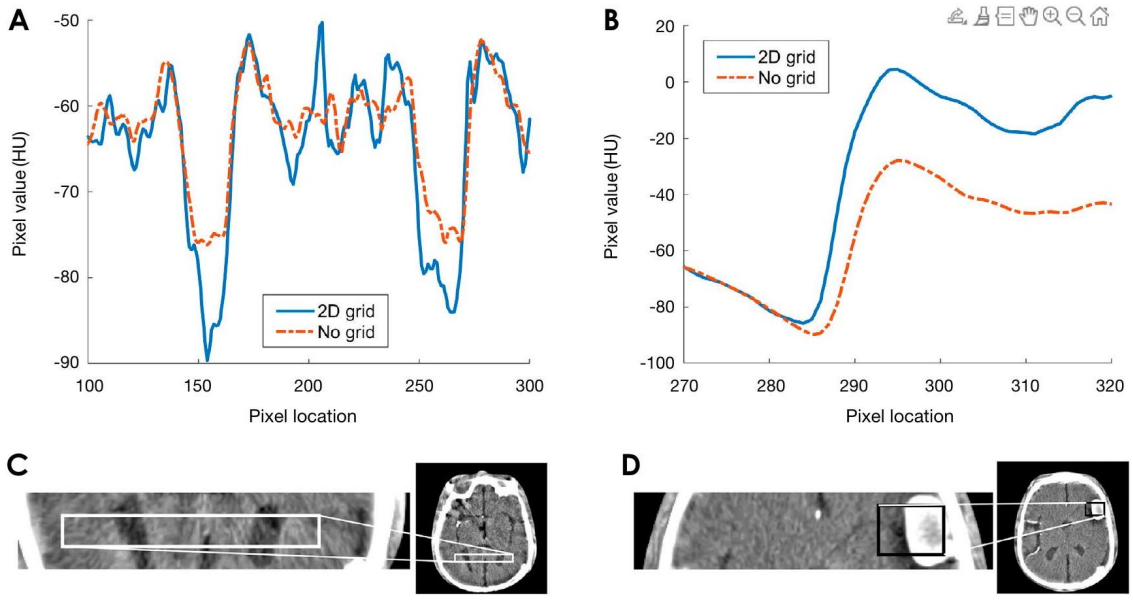

Figure 40: Line profiles drawn over ventricle (A) and hemorrhage (B) according to the regions of interests (ROIs) indicated in C and D , demonstrate soft tissue contrast in images acquired with and without the 2-dimensional (2D) grid. [Adapted from [165]]

variation remains an area for further investigation.

Another area of interest is the accuracy of HU values in high-density regions, such as dentin, after scatter suppression. However, estimating the ground truth HU values for dentin is nontrivial because HU values vary strongly as a function of X-ray energy. The mean energy of the 110 kVp X-ray spectrum used in this study was estimated at 65 keV in the absence of a phantom; however, beam hardening in dentin would likely increase the mean beam energy to between 70 and 90 keV , corresponding to a theoretical dentin HU range of $1520 - 2240$HU. The mean HU value of dentin was 1718 HU in CBCT images acquired with the 2D grid, which falls within the expected range, whereas it was 1227 HU in images without the 2D grid, indicating an underestimation of dentin density. Contrast was also improved in both soft and hard tissue regions. For example, contrast in calcium-containing regions was 27% higher (Fig. 40), and soft tissue contrast in a brain-mimicking phantom was approximately 50% higher (Fig. 39).

Improved CT number accuracy in bony anatomy and teeth has various quantitative imaging applications, including facilitating the extraction of bone density from CBCT images for dental implant placement planning, surgical tooth extractions, evaluation of dental bone grafts, and corrective jaw surgery. Virtual 3D models generated for surgical planning rely on precise segmentation of anatomical structures; improved CT number accuracy may enhance segmentation and thus yield more accurate 3D models. In implant treatment planning, better CT number accuracy can assist in quantitatively assessing bone quality at an implant site. Regarding post-implant CBCT images, more accurate r representation of bone density and morphology may improve evaluations of peri-implant bone, such as assessments of bone integration or bone loss. [148] Additionally, higher soft tissue contrast could facilitate the visualization of soft tissue lesions and gingival soft tissue thickness. [145] Although the dental CBCT system used in this work is not designed for intracranial

imaging, the observed improvement in soft tissue contrast suggests that a flat-panel detector-based CBCT system integrated with a 2 D grid could potentially be used beyond dental and maxillofacial imaging, such as for bedside imaging of hemorrhage in the brain.[171]

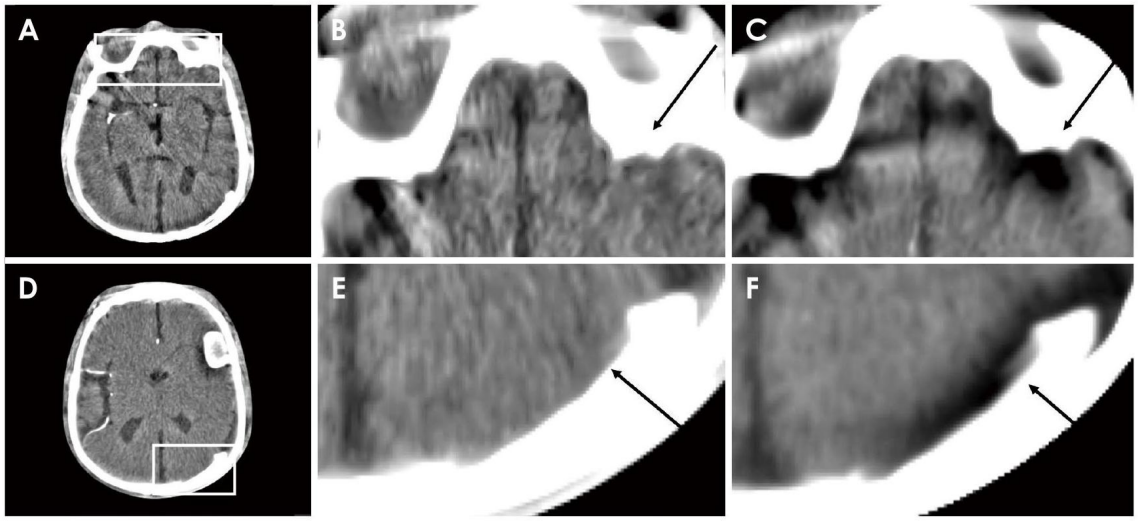

Figure 41: Magnified sections of the artifact region indicated by the white box in *A* are shown in *B* acquired with the 2D: 2-dimensional (2D) grid and *C* (without the 2 D grid). Similarly, magnified sections of the artifact region indicated by the white box in D are shown in E (acquired with the 2D grid) and F (without the 2D grid). 2D: 2-dimensional. [Adapted from [165]]

Another area of interest is the comparison of CBCT images acquired with the 2D grid prototype to those obtained using a conventional 1D antiscatter grid, which consists of a 1D array of lead lamellae. Although 1D grids are commonly used in diagnostic X-ray imaging, [172] a conventional 1D grid with a focusing geometry suitable for dental CBCT systems was not available for this study. Previous studies comparing 2D and 1 D grids in CBCT systems-primarily designed for imaging the human torso. These works demonstrated that 2D grids have a factor of 2-6 lower scatter transmission than conventional 1D grids. [160, 161] In general, 2D grids provide superior scatter suppression, CT number consistency, and contrast-to-noise ratio than 1D grids when imaging large FOVs or anatomical regions, such as the pelvis. [163] An image quality comparison of 1D and 2D grids in dental CBCT remains a subject for future investigation.

This study had several limitations. First, the 2D grid prototype was relatively small, covering only about 18% of the FOV in the cranio-caudal direction. A larger 2D grid spanning the full FOV of the CBCT system remains to be investigated. Although the grid prototype in this initial feasibility study covered only a small section of the X-ray detector, the full FOV was irradiated in all experiments, as in a full-FOV CBCT scan. This ensured that the scatter intensity generated by the imaged object was equivalent to that in a fullFOV scan, thus mimicking realistic scanning conditions. It is expected that a larger 2D grid would exhibit similar scatter transmission characteristics and a comparable trend in image quality improvement. The impact of scatter mitigation on image quality using smaller FOV protocols will be investigated in the future. Second, the image processing software was not fully optimized for 2D grid implementation. The noise properties of CBCT images acquired with the 2D grid differ substantially due to its X-ray transmission characteristics and require further research. Third, this study did not investigate the effect of robust scatter suppression on metal

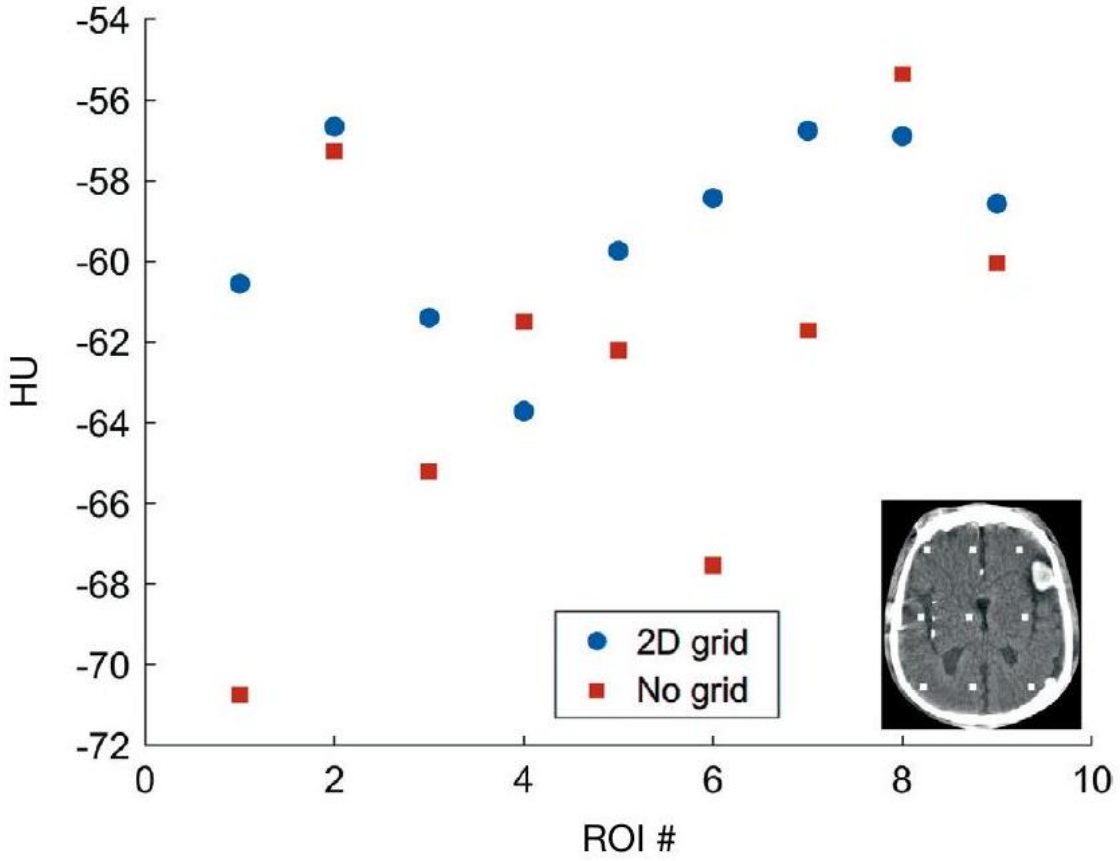

Figure 42: Mean Hounsfield unit (HU) values in 9 region of interests (ROIs) demonstrate improved HU uniformity in the brain phantom. The ROI locations are shown in the inset. With the 2-dimensional (2D) grid, the standard deviation of HU values among the ROIs was reduced from 4.8 to 2.4 HU . The maximum deviation from the mean HU of all ROIs was 8.3 HU without the 2 D grid and 4.5 HU with the grid. [Adapted from [165]]

artifacts.

In this work, a prototype 2D grid was developed and evaluated for dental CBCT systems. The prototype reduced scattered X-ray intensity and improved the fidelity of CBCT images. Notably, a significant improvement in HU value uniformity was observed in bony structures and teeth. Such improvement could enhance the utility of dental CBCT imaging for the quantitative evaluation of bone density, provide better visualization of peri-implant tissues, and enable more accurate generation of 3D models for surgical planning and surgical guides. Improved contrast and reduced artifacts in soft tissues may further expand the applications of dental CBCT systems in soft tissue imaging. Future work will focus on optimizing 2D grid properties for dental CBCT and fabricating a larger grid prototype to enable imaging of larger anatomical regions.

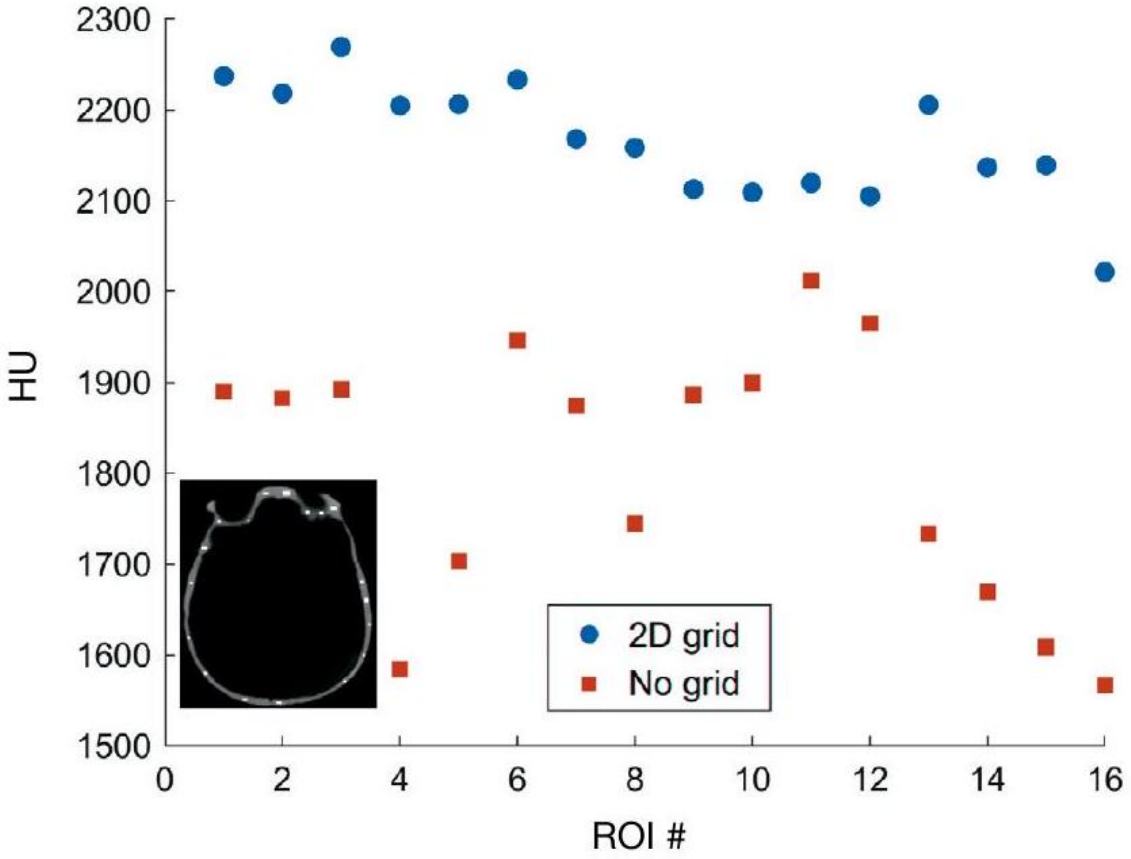

Figure 43: Mean Hounsfield unit(HU) values in 16 region of interests (ROIs) demonstrate improved HU uniformity in the skull region. The ROI locations are shown in the inset. With the 2-dimensional (2D) grid, the standard deviation of HU values among the ROIs was reduced from 208 to 104 HU . The maximum deviation from the mean HU of all ROIs was 144 HU without the 2D grid and 64 HU with the grid. [Adapted from [165]]

8 Conclusion & outlook

The aim of the thesis was to investigate the technical feasibility of obtaining quantitative data from dentomaxillofacial imaging systems and to explore the possible applications of such systems.

Summary:

The first three experimental chapters focus on the spectral panoramic imaging system.

Chapter 4 demonstrates that projection-based decomposition algorithms cannot be applied directly to panoramic projection images, as the count rates are so low that bias would be exceedingly high. An algorithm to calibrate and decompose the panoramic image as a whole is then presented as a solution. Preliminary quantitative results are then discussed. It also demonstrated that scatter sets the upper limit for the thicknesses that can be accurately decomposed and that the typical thicknesses present in dentomaxillofacial imaging are below this limit.

Chapter 5 presents a simulation framework for generating synthetic panoramic images from CT and CBCT volumes. The framework was used to cross-verify the experimental results obtained previously and was also used in a reader study [173]. Visual correlation is mostly good between the experimental and synthetic images, although some deviation is caused by the segmentation, as segmenting CT or CBCT volumes to bone and soft tissue does not yield the same result as spectral material decomposition.

Chapter 6 updates the simulation framework of Ch. 5 to work on multi-energy volumes. The spectral synthetic panoramic images generated from helical DECT scans are compared against the results of the experimental panoramic system. Specifically, the bone mineral densities from the experimental and synthetic panoramic images are compared. There is a good agreement both visually and quantitatively. Additionally, the experimental system outputs a good linear regression of BMD phantom across a broad range of clinically relevant aBMD values.

The final experimental Chapter, 7, focuses on the dental CBCT system fitted with the 2D antiscatter grid. The novelty of this research lies within exploring the benefits of scatter reduction in the context of head and neck area imaging. Both tissue contrast and homogeneity are significantly improved with the grid. These improvements apply to both soft and hard tissues.

Outlook:

Osteoporosis screening and monitoring remineralization after surgery are some possible applications of aBMD measurement in spectral panoramic imaging. Thus, chapters 4-6 present the means and the results on how spectral photon counting could enable a new application for panoramic imaging. However, the presented work is expected to mainly work for the mandible, as the maxilla will be likely to have overlapping bone structures even after the detector mount is fixed. Additionally, this approach obviously requires a hardware upgrade to be deployed in the field. A significant portion of the proposed spectral panoramic systems would be deployed in private dental clinics. An additional challenge would then be to incentivize the private clinics to participate in the opportunistic osteoporosis screening.

The simulation tools developed for the papers of this thesis might also have use on their own. Major dental CBCT vendors offer tools to generate synthetic panoramic images from CBCT volumes. Further research could focus on finding out if the tools described in this thesis could offer additional value in this case. Additionally, a standalone simulator tool could be of use to academics and clinicians for training and research purposes.

Improved tissue contrast and consistency enabled by the ASG in ch. 7 could enable new applications in head and neck CBCT. Enhanced hard tissue contrast and consistency would improve existing workflows, as dental CBCTs are used for surgical planning and monitoring in oral and maxillofacial surgeries. Enhanced soft tissue contrast could be useful in mobile head and neck imaging applications, such as diagnosing intracranial hemorrhage.

The proposed anti-scatter grid design requires some consideration as well. Covering full detector requires modules, and are applications relevant enough for dental clinics. The CBCT system design would need to have a different layout for emergency applications. A supine position would be required. The active area of the detector depends on the application. A smaller detector would be sufficient for a purely brain imaging system [4]. For a whole body system, a larger detector is required. An example of such a system would be Planmed XFI.

Dual layer flat panels could be an intermediate step on the way towards photon counting CBCT, as the technological roadmap for photon counting flat panels remains uncertain. Alternatively, slow kVp switching could be realized with existing hardware. Movement artefacts would then have to be addressed.

Conclusion:

Two separate pipelines of hardware-based image quality enhancement in dentomaxillofacial imaging have been investigated: the spectral panoramic pipeline yielded an algorithm enabling spectral imaging in the experimental setup as well as simulation tools for cross verification and potential for use elsewhere. The 2D ASG study demonstrated the improvement of tissue contrast and consistency, enabling possible new applications. Thus, there are no fundamental technical limitations in going from engineering prototypes to clinical trials with these systems.

Appendix: Scientific contributions

Publications with significant contribution (peer-reviewed)

V Somerkivi, T Sellerer, T Pantsar, H Lohman, and F Pfeiffer. Spectral photon counting for panoramic dental imaging. Biomedical Physics & Engineering Express, vol. 9, no. 3. 2023.

V Somerkivi, T Sellerer, D Berthe, Y Haemisch, T Pantsar, H Lohman, T Kaasalainen, and F Pfeiffer. Mandible bone mineral density estimation using spectral panoramic X-ray imaging. Imaging Science in Dentistry, vol. 55, no. 1. 2025.

B Li, V Somerkivi, F Bayat, C Huynh, and C Altunbas. Effect of a prototype 2-dimensional antiscatter grid on image quality obtained with a dental cone-beam computed tomography scanner. Imaging Science in Dentistry, vol. 55, no. 1. 2025.

Other work with significant contribution

V Somerkivi, A Kolb, R Sellerer, D Berthe, Y Haemisch, T Pantsar, H Lohman, and F Pfeiffer. Generating spectral dental panoramic images from single energy computed tomography volumes. arXiv:2305.10087 (2023).

Publications as a contributing author (peer-reviewed)

S Hoshian, V Jokinen, V Somerkivi, AR Lokanathan, and S Franssila. Robust superhydrophobic silicon without a low surface-energy hydrophobic coating. ACS applied materials & interfaces, vol. 7, no. 1. 2015.

D Berthe, D Kolb, A Rabi, T Sellerer, V Somerkivi, GC Feuerriegel, AP Sauter, F Meurer, Y Haemisch, T Pantsar, H Lohman, D Pfeiffer, and F Pfeiffer. Evaluation of Spectral X-Ray Imaging for Panoramic Dental Images Based on a Simulation Framework. Journal of Imaging Informatics in Medicine, vol 37, no. 2, 2024.

Conference Talk

V Somerkivi, T Sellerer, T Pantsar, H Lohman, and F Pfeiffer. Spectral photon counting for panoramic dental imaging. International Symposium on Medical Applications of X-ray, Phase-contrast and Photon-counting. Munich, Germany. 2023.

References

[1] T. Kiljunen, T. Kaasalainen, A. Suomalainen, and M. Kortesniemi, "Dental cone beam ct: A review," *Physica Medica*, vol. 31, no. 8, pp. 844–860, 2015.

[2] A. Suomalainen, E. Pakbaznejad Esmaeili, and S. Robinson, "Dentomaxillofacial imaging with panoramic views and cone beam ct," *Insights into imaging*, vol. 6, pp. 1–16, 2015.

[3] T. Kaasalainen, M. Ekholm, T. Siiskonen, and M. Kortesniemi, "Dental cone beam ct: An updated review," *Physica Medica*, vol. 88, pp. 193–217, 2021.

[4] A. Sisniega, W. Zbijewski, J. Xu, H. Dang, J. W. Stayman, J. Yorkston, N. Aygun, V. Koliatsos, and J. H. Siewerdsen, "High-fidelity artifact correction for cone-beam ct imaging of the brain," *Physics in Medicine & Biology*, vol. 60, no. 4, p. 1415, 2015.

[5] U. N. S. C. on the Effects of Atomic Radiation, "Sources, effect and risks of ionizing radiation 2020/2021, volume I," United Nations, New York, US, UNSCEAR Report, 2022.

[6] J. M. Ianucci and L. J. Howerton, *Dental Radiography: Principles and Techniques*, 4th ed. St. Louis, MO, USA: Elsevier-Saunders, 2012.

[7] R. Ballabriga, J. Alozy, M. Campbell, E. Frojdh, E. Heijne, T. Koenig, X. Llopart, J. Marchal, D. Pennicard, T. Poikela, L. Tlustos, P. Valerio, W. Wong, and M. Zuber, "Review of hybrid pixel detector readout ASICs for spectroscopic X-ray imaging," *Journal of Instrumentation*, no. 01, pp. P01 007–P01 007, jan 2016.

[8] A. Sisniega, W. Zbijewski, A. Badal, I. S. Kyprianou, J. W. Stayman, J. J. Vaquero, and J. H. Siewerdsen, "Monte carlo study of the effects of system geometry and antiscatter grids on cone-beam ct scatter distributions," *Medical Physics*, vol. 40, no. 5, p. 051915, 2013. [Online]. Available: https://aapm.onlinelibrary.wiley.com/doi/abs/10.1118/1.4801895

[9] H. Dang, J. Stayman, A. Sisniega, J. Xu, W. Zbijewski, X. Wang, D. Foos, N. Aygun, V. Koliatsos, and J. Siewerdsen, "Statistical reconstruction for cone-beam ct with a post-artifact-correction noise model: application to high-quality head imaging," *Physics in Medicine & Biology*, vol. 60, no. 16, p. 6153, 2015.

[10] R. Behling and F. Grüner, "Diagnostic x-ray sources—present and future," *Nuclear Instruments and Methods in Physics Research Section A: Accelerators, Spectrometers, Detectors and Associated Equipment*, vol. 878, pp. 50–57, 2018.

[11] R. Birch and M. Marshall, "Computation of bremsstrahlung x-ray spectra and comparison with spectra measured with a ge (li) detector," *Physics in Medicine & Biology*, vol. 24, no. 3, p. 505, 1979.

[12] H. Bethe, "Bremsformel für elektronen relativistischer geschwindigkeit," *Zeitschrift für Physik*, vol. 76, no. 5, pp. 293–299, 1932.

[13] M. Berger, J. Coursey, and M. Zucker, "Estar, pstar, and astar: Computer programs for calculating stopping-power and range tables for electrons, protons, and helium ions (version 1.21)," 1999-01-01 1999.

[14] T. M. Buzug, "Computed tomography," in *Springer Handbook of Medical Technology*. Springer, 2011, pp. 311–342.

[15] H. Nikjoo, S. Uehara, and D. Emfietzoglou, *Interaction of radiation with matter*. CRC press, 2012.

[16] K. Siegbahn, *Alpha-, beta-and gamma-ray spectroscopy*. Elsevier, 2012.

[17] K. W. Fornalski, "Simple empirical correction functions to cross sections of the photoelectric effect, compton scattering, pair and triplet production for carbon radiation shields for intermediate and high photon energies," *Journal of Physics Communications*, vol. 2, no. 3, p. 035038, 2018.

[18] D. E. Cullen, J. H. Hubbell, and L. Kissel, "Epdl 97 : the evaluated photon data library '97," 1997.

[19] W. Heitler, *Quantum theory of radiation*. Oxford University Press, London, 1954, vol. 32.

[20] I. t. Waller and D. R. Hartree, "On the intensity of total scattering of x-rays," *Proceedings of the Royal Society of London. Series A, Containing Papers of a Mathematical and Physical Character*, vol. 124, no. 793, pp. 119–142, 1929.

[21] J. Hubbell, W. J. Veigele, E. Briggs, R. Brown, D. Cromer, and d. R. Howerton, "Atomic form factors, incoherent scattering functions, and photon scattering cross sections," *Journal of physical and chemical reference data*, vol. 4, no. 3, pp. 471–538, 1975.

[22] F. Salvat, J. M. Fernández-Varea, J. Sempau *et al.*, "Penelope-2006: A code system for monte carlo simulation of electron and photon transport," in *Workshop proceedings*, vol. 4, no. 6222. Citeseer, 2006, p. 7.

[23] J. H. Hubbell and S. M. Seltzer, "Tables of X-ray mass attenuation coefficients and mass energy-absorption coefficients 1 keV to 20 MeV for elements Z=1 to 92 and 48 additional substances of dosimetric interest," Tech. Rep., May 1995. [Online]. Available: http://cds.cern.ch/record/353989

[24] M. Spahn, "X-ray detectors in medical imaging," *Nuclear Instruments and Methods in Physics Research Section A: Accelerators, Spectrometers, Detectors and Associated Equipment*, vol. 731, pp. 57–63, 2013.

[25] Y. Arai, E. Tammisalo, K. Iwai, K. Hashimoto, and K. Shinoda, "Development of a compact computed tomographic apparatus for dental use," *Dentomaxillofacial radiology*, vol. 28, no. 4, pp. 245–248, 1999.

[26] M. Nikl, "Scintillation detectors for x-rays," *Measurement Science and Technology*, vol. 17, no. 4, p. R37, 2006.

[27] G. F. Knoll, *Radiation detection and measurement*. John Wiley & Sons, 2010.

[28] R. Lanier, "Recent developments in x-ray imaging technology," 2012.

[29] C. Michail, P. Liaparinos, N. Kalyvas, I. Kandarakis, G. Fountos, and I. Valais, "Radiation detectors and sensors in medical imaging," *Sensors (Basel, Switzerland)*, vol. 24, no. 19, p. 6251, 2024.

[30] H. Krüger, J. Fink, E. Kraft, N. Wermes, P. Fischer, I. Peric, C. Herrmann, M. Overdick, and W. Rütten, "Cix: a detector for spectrally enhanced x-ray imaging by simultaneous counting and integrating," in *Medical Imaging 2008: Physics of Medical Imaging*, vol. 6913. SPIE, 2008, pp. 245–256.

[31] A. Pourmorteza, R. Symons, V. Sandfort, M. Mallek, M. K. Fuld, G. Henderson, E. C. Jones, A. A. Malayeri, L. R. Folio, and D. A. Bluemke, "Abdominal imaging with contrast-enhanced photon-counting ct: first human experience," *Radiology*, vol. 279, no. 1, pp. 239–245, 2016.

[32] F. S. L. Thomsen, S. Horstmeier, J. H. Niehoff, J. A. Peña, and J. Borggrefe, "Effective spatial resolution of photon counting ct for imaging of trabecular structures is superior to conventional clinical ct and similar to high resolution peripheral ct," *Investigative Radiology*, vol. 57, no. 9, pp. 620–626, 2022.

[33] Y. Gaillandre, A. Duhamel, T. Flohr, J.-B. Faivre, S. Khung, A. Hutt, P. Felloni, J. Remy, and M. Remy-Jardin, "Ultra-high resolution ct imaging of interstitial lung disease: impact of photon-counting ct in 112 patients," *European Radiology*, vol. 33, no. 8, pp. 5528–5539, 2023.

[34] E. Cuccione, P. Chhour, S. Si-Mohamed, C. Dumot, J. Kim, V. Hubert, C. C. Da Silva, M. Vandamme, E. Chereul, J. Balegamire *et al.*, "Multicolor spectral photon counting ct monitors and quantifies therapeutic cells and their encapsulating scaffold in a model of brain damage," *Nanotheranostics*, vol. 4, no. 3, p. 129, 2020.

[35] R. Ballabriga, "The Design and Implementation in $0.13\mu m$ CMOS of an Algorithm Permitting Spectroscopic Imaging with High Spatial Resolution for Hybrid Pixel Detectors," Ph.D. dissertation, Ramon Llull U., Barcelona, 2009, presented on 24 Nov 2009. [Online]. Available: https://cds.cern.ch/record/1259673

[36] R. Ballabriga, M. Campbell, and X. Llopart, "Asic developments for radiation imaging applications: The medipix and timepix family," *Nuclear Instruments and Methods in Physics Research Section A: Accelerators, Spectrometers, Detectors and Associated Equipment*, vol. 878, pp. 10–23, 2018.

[37] L. Abbene, G. Gerardi, A. Turturici, S. Del Sordo, and F. Principato, "Experimental results from al/p-cdte/pt x-ray detectors," *Nuclear Instruments and Methods in Physics Research Section A: Accelerators, Spectrometers, Detectors and Associated Equipment*, vol. 730, pp. 135–140, 2013.

[38] F. Principato, A. Turturici, M. Gallo, and L. Abbene, "Polarization phenomena in al/p-cdte/pt x-ray detectors," *Nuclear Instruments and Methods in Physics Research Section A: Accelerators, Spectrometers, Detectors and Associated Equipment*, vol. 730, pp. 141–145, 2013.

[39] T. Schlesinger, J. Toney, H. Yoon, E. Lee, B. Brunett, L. Franks, and R. James, "Cadmium zinc telluride and its use as a nuclear radiation detector material," *Materials Science and Engineering: R: Reports*, vol. 32, no. 4-5, pp. 103–189, 2001.

[40] J. S. Iwanczyk, *Radiation detectors for medical imaging.* CRC Press, 2015, vol. 45.

[41] H. H. Barrett and K. J. Myers, *Foundations of image science.* John Wiley & Sons, 2013.

[42] K. Koughia and S. Kasap, "Density of states of a-se near the valence band," *Journal of non-crystalline solids*, vol. 352, no. 9-20, pp. 1539–1542, 2006.

[43] C. Ullberg, M. Urech, N. Weber, A. Engman, A. Redz, and F. Henckel, "Measurements of a dual-energy fast photon counting cdte detector with integrated charge sharing correction," in *Medical Imaging 2013: Physics of Medical Imaging*, vol. 8668. International Society for Optics and Photonics, 2013, p. 86680P.

[44] A. Krzyżanowska, G. Deptuch, P. Maj, P. Gryboś, and R. Szczygieł, "Characterization of the photon counting chase jr., chip built in a 40-nm cmos process with a charge sharing correction algorithm using a collimated x-ray beam," *IEEE Transactions on Nuclear Science*, vol. 64, no. 9, pp. 2561–2568, 2017.

[45] K. Spartiotis, R. Durrant, A. Leppanen, H. Lohman, O. Mannisto, T. Pantsar, J. Pyyhtia, and T. Schulman, "X-and gamma ray imaging systems based on cdte-cmos detector technology," in *2008 IEEE Nuclear Science Symposium Conference Record*. IEEE, 2008, pp. 518–522.

[46] M. Overdick, C. Baumer, K. J. Engel, J. Fink, C. Herrmann, H. Kruger, M. Simon, R. Steadman, and G. Zeitler, "Status of direct conversion detectors for medical imaging with x-rays," *IEEE Transactions on Nuclear Science*, vol. 56, no. 4, pp. 1800–1809, 2009.

[47] P. M. Queiroz, G. M. Santaella, S. L. P. de Castro Lopes, F. Haiter-Neto, and D. Q. Freitas, "Characteristics of radiographic images acquired with cdte, ccd and cmos detectors in skull radiography," *Imaging Science in Dentistry*, vol. 50, no. 4, p. 339, 2020.

[48] S. van der Sar, "Evaluating methods for a combined measurement of counts and energy with x-ray photon-counting scintillation detectors," in *IEEE Nuclear Science Symposuim & Medical Imaging Conference*. IEEE, 2020.

[49] H. W. Goo and J. M. Goo, "Dual-energy ct: new horizon in medical imaging," *Korean journal of radiology*, vol. 18, no. 4, pp. 555–569, 2017.

[50] R. E. Alvarez, "Dimensionality and noise in energy selective x-ray imaging," *Medical physics*, vol. 40, no. 11, p. 111909, 2013.

[51] K. Mechlem, "Towards low-dose spectral phase-contrast x-ray imaging," Ph.D. dissertation, Technical University of Munich, 2020.

[52] M. I. Iacono, E. Neufeld, E. Akinnagbe, K. Bower, J. Wolf, I. Vogiatzis Oikonomidis, D. Sharma, B. Lloyd, B. J. Wilm, M. Wyss *et al.*, "Mida: a multimodal imaging-based detailed anatomical model of the human head and neck," *PloS one*, vol. 10, no. 4, p. e0124126, 2015.

[53] M. A. F. Zenóbio, M. S. N. Tavares, E. G. Zenóbio, and T. A. Silva, "Elemental composition of dental biologic tissues: study by means of different analytical techniques," *Journal of Radioanalytical and Nuclear Chemistry*, vol. 289, no. 1, pp. 161–166, 2011.

[54] P. M. Joseph and R. D. Spital, "A method for correcting bone induced artifacts in computed tomography scanners," *Journal of computer assisted tomography*, vol. 2, no. 1, pp. 100–108, 1978.

[55] W. H. Press, W. T. Vetterling, S. A. Teukolsky, and B. P. Flannery, *Numerical recipes*. Citeseer, 1988.

[56] L. Condat, "Discrete total variation: New definition and minimization," *SIAM Journal on Imaging Sciences*, vol. 10, no. 3, pp. 1258–1290, 2017.

[57] L. Wasserman, *All of statistics: a concise course in statistical inference*. Springer Science & Business Media, 2013.

[58] J. A. Fessler, "Hybrid poisson/polynomial objective functions for tomographic image reconstruction from transmission scans," *IEEE Transactions on Image Processing*, vol. 4, no. 10, pp. 1439–1450, 1995.

[59] K. Mechlem, T. Sellerer, S. Ehn, D. Münzel, E. Braig, J. Herzen, P. B. Noël, and F. Pfeiffer, "Spectral angiography material decomposition using an empirical forward model and a dictionary-based regularization," *IEEE Transactions on Medical Imaging*, vol. 37, no. 10, pp. 2298–2309, 2018.

[60] R. E. Alvarez and A. Macovski, "Energy-selective reconstructions in x-ray computerised tomography," *Physics in Medicine & Biology*, vol. 21, no. 5, p. 733, 1976.

[61] G. N. Hounsfield, "Computerized transverse axial scanning (tomography): Part 1. description of system," *The British journal of radiology*, vol. 46, no. 552, pp. 1016–1022, 1973.

[62] M. H. Albrecht, T. J. Vogl, S. S. Martin, J. W. Nance, T. M. Duguay, J. L. Wichmann, C. N. De Cecco, A. Varga-Szemes, M. van Assen, C. Tesche *et al.*, "Review of clinical applications for virtual monoenergetic dual-energy ct," *Radiology*, vol. 293, no. 2, pp. 260–271, 2019.

[63] J. Schlomka, E. Roessl, R. Dorscheid, S. Dill, G. Martens, T. Istel, C. Bäumer, C. Herrmann, R. Steadman, G. Zeitler *et al.*, "Experimental feasibility of multi-energy photon-counting k-edge imaging in pre-clinical computed tomography," *Physics in medicine and biology*, vol. 53, no. 15, p. 4031, 2008.

[64] S. Ehn, T. Sellerer, K. Mechlem, A. Fehringer, M. Epple, J. Herzen, F. Pfeiffer, and P. Noël, "Basis material decomposition in spectral ct using a semi-empirical, polychromatic adaption of the beer–lambert model," *Physics in Medicine and Biology*, vol. 62, pp. N1–N17, 2017.

[65] X. Duan, J. Wang, L. Yu, S. Leng, and C. H. McCollough, "Ct scanner x-ray spectrum estimation from transmission measurements," *Medical physics*, vol. 38, no. 2, pp. 993–997, 2011.

[66] L. Zhang, G. Zhang, Z. Chen, Y. Xing, J. Cheng, and Y. Xiao, "X-ray spectrum estimation from transmission measurements using the expectation maximization method," in *Nuclear Science Symposium Conference Record, 2007. NSS'07. IEEE*, vol. 4. IEEE, 2007, pp. 3089–3093.

[67] E. Roessl, H. Daerr, and R. Proksa, "A fourier approach to pulse pile-up in photon-counting x-ray detectors," *Medical physics*, vol. 43, no. 3, pp. 1295–1298, 2016.

[68] L. A. Feldkamp, L. Davis, and J. W. Kress, "Practical cone-beam algorithm," *Josa a*, vol. 1, no. 6, pp. 612–619, 1984.

[69] S. Schaller, T. Flohr, K. Klingenbeck, J. Krause, T. Fuchs, and W. A. Kalender, "Spiral interpolation algorithm for multislice spiral ct. i. theory," *IEEE transactions on medical imaging*, vol. 19, no. 9, pp. 822–834, 2000.

[70] H. Villarraga-Gómez and S. T. Smith, "Effect of the number of projections on dimensional measurements with x-ray computed tomography," *Precision Engineering*, vol. 66, pp. 445–456, 2020.

[71] C.-M. Tang, E. Stier, K. Fischer, and H. Guckel, "Anti-scattering x-ray grid," *Microsystem technologies*, vol. 4, pp. 187–192, 1998.

[72] V. Lehmann and S. Rönnebeck, "Mems techniques applied to the fabrication of anti-scatter grids for x-ray imaging," *Sensors and Actuators A: Physical*, vol. 95, no. 2-3, pp. 202–207, 2002.

[73] G. Vogtmeier, R. Dorscheid, K. J. Engel, R. Luhta, R. Mattson, B. Harwood, M. Appleby, B. Randolph, and J. Klinger, "Two-dimensional anti-scatter grids for computed tomography detectors," in *Medical Imaging 2008: Physics of Medical Imaging*, vol. 6913. SPIE, 2008, pp. 1659–1669.

[74] W. A. Kalender, "Der einsatz von flachbilddetektoren für die ct-bildgebung," *Der Radiologe*, vol. 43, no. 5, pp. 379–387, 2003.

[75] M. S. Seyam, P. Koshy, and M. A. Elbestawi, "Laser powder bed fusion of unalloyed tungsten: a review of process, structure, and properties relationships," *Metals*, vol. 12, no. 2, p. 274, 2022.

[76] M. Jiang, Y. Yang, C. Han, J. Liu, M. Yan, C. Yang, S. Wei, H. Lu, and D. Wang, "Defect formation mechanism and suppression strategy in additively manufactured tungsten grid thin-wall structures via laser powder bed fusion," *Journal of Manufacturing Processes*, vol. 120, pp. 222–233, 2024.

[77] J. M. Ianucci and L. J. Howerton, *Dental Radiography: Principles and Techniques*, 4th ed. St. Louis, MO, USA: Elsevier-Saunders, 2012.

[78] F. Gijbels, R. Jacobs, R. Bogaerts, D. Debaveye, S. Verlinden, and G. Sanderink, "Dosimetry of digital panoramic imaging. part i: Patient exposure," *Dentomaxillofac Radiol*, vol. 34, no. 3, pp. 145–149, May 2005.

[79] R. Izzetti, M. Nisi, G. Aringhieri, L. Crocetti, F. Graziani, and C. Nardi, "Basic knowledge and new advances in panoramic radiography imaging techniques: A narrative review on what dentists and radiologists should know," *Applied Sciences*, vol. 11, no. 17, p. 7858, 2021.

[80] V. Somerkivi, A. Kolb, T. Sellerer, D. Berthe, Y. Haemisch, T. Pantsar, H. Lohman, and F. Pfeiffer, "Generating spectral dental panoramic images from computed tomography volumes," *arXiv preprint arXiv:2305.10087*, 2023.

[81] E. Hofmann, R. Fimmers, M. Schmid, U. Hirschfelder, A. Detterbeck, and K. Hertrich, "Landmarks of the frankfort horizontal plane." *Journal of Orofacial Orthopedics/Fortschritte der Kieferorthopadie*, vol. 77, no. 5, 2016.

[82] H.-G. Yeom, J.-E. Kim, K.-H. Huh, W.-J. Yi, M.-S. Heo, S.-S. Lee, S.-C. Choi, and S.-J. Lee, "Development of panorama resolution phantom for comprehensive evaluation of the horizontal and vertical resolution of panoramic radiography," *Scientific Reports*, vol. 10, no. 1, p. 16529, 2020.

[83] W. Scarfe, F. Eraso, and A. Farman, "Characteristics of the orthopantomograph op 100." *Dentomaxillofacial Radiology*, vol. 27, no. 1, pp. 51–57, 1998.

[84] D. Brüllmann and R. Schulze, "Spatial resolution in cbct machines for dental/maxillofacial applications—what do we know today?" *Dentomaxillofacial Radiology*, vol. 44, no. 1, p. 20140204, 2015.

[85] I. Rozylo-Kalinowska, *Imaging Techniques in Dental Radiology*. Springer Cham, 2020.

[86] A. Loughlin, N. Drage, C. Greenall, and D. Farnell, "An investigation in to the impact of acquisition location on error type and rate when undertaking panoramic radiography," *Radiography*, vol. 23, no. 4, pp. 305–309, 2017.

[87] A. W. K. Yeung and N. S. M. Wong, "Reject rates of radiographic images in dentomaxillofacial radiology: a literature review," *International Journal of Environmental Research and Public Health*, vol. 18, no. 15, p. 8076, 2021.

[88] H. Gaêta-Araujo, T. Alzoubi, K. d. F. Vasconcelos, K. Orhan, R. Pauwels, J. W. Casselman, and R. Jacobs, "Cone beam computed tomography in dentomaxillofacial radiology: a two-decade overview," *Dentomaxillofacial Radiology*, vol. 49, no. 8, p. 20200145, 2020.

[89] W. A. Kalender, W. Seissler, E. Klotz, and P. Vock, "Spiral volumetric ct with single-breath-hold technique, continuous transport, and continuous scanner rotation." *Radiology*, vol. 176, no. 1, pp. 181–183, 1990.

[90] Y. A. AlJehani *et al.*, "Diagnostic applications of cone-beam ct for periodontal diseases," *International journal of dentistry*, vol. 2014, 2014.

[91] Z. Abramson, S. M. Susarla, M. Lawler, C. Bouchard, M. Troulis, and L. B. Kaban, "Three-dimensional computed tomographic airway analysis of patients with obstructive sleep apnea treated by maxillomandibular advancement," *Journal of Oral and Maxillofacial Surgery*, vol. 69, no. 3, pp. 677–686, 2011.

[92] S. Patel, A. Dawood, T. P. Ford, and E. Whaites, "The potential applications of cone beam computed tomography in the management of endodontic problems," *International endodontic journal*, vol. 40, no. 10, pp. 818–830, 2007.

[93] M. Ahmad, J. Jenny, and M. Downie, "Application of cone beam computed tomography in oral and maxillofacial surgery," *Australian dental journal*, vol. 57, pp. 82–94, 2012.

[94] S. Kapila and J. Nervina, "Cbct in orthodontics: assessment of treatment outcomes and indications for its use," *Dentomaxillofacial radiology*, vol. 44, no. 1, p. 20140282, 2015.

[95] W. D. McDavid, U. Welander, S. Brent Dove, and G. Tronjje, "Digital imaging in rotational panoramic radiography," *Dentomaxillofacial Radiology*, vol. 24, no. 2, pp. 68–75, 1995.

[96] K. Kamburoglu, E. Kolsuz, S. Murat, S. Yüksel, and T. Ozen, "Proximal caries detection accuracy using intraoral bitewing radiography, extraoral bitewing radiography and panoramic radiography," *Dentomaxillofacial Radiology*, vol. 41, no. 6, pp. 450–459, 2012.

[97] C. Nardi, L. Calistri, G. Grazzini, I. Desideri, C. Lorini, M. Occhipinti, F. Mungai, and S. Colagrande, "Is panoramic radiography an accurate imaging technique for the detection of endodontically treated asymptomatic apical periodontitis?" *Journal of Endodontics*, vol. 44, no. 10, pp. 1500–1508, 2018. [Online]. Available: https://www.sciencedirect.com/science/article/pii/S0099239918304655

[98] Y. Ohashi, Y. Ariji, A. Katsumata, H. Fujita, M. Nakayama, M. Fukuda, M. Nozawa, and E. Ariji, "Utilization of computer-aided detection system in diagnosing unilateral maxillary sinusitis on panoramic radiographs," *Dentomaxillofacial Radiology*, vol. 45, no. 3, p. 20150419, 2016.

[99] K. Mechlem, T. Sellerer, M. Viermetz, J. Herzen, and F. Pfeiffer, "Spectral differential phase contrast x-ray radiography," *IEEE Trans. Med. Imaging*, vol. 39, no. 3, pp. 578–587, Mar. 2020.

[100] L. Shi, M. Lu, N. R. Bennett, E. Shapiro, J. Zhang, R. Colbeth, J. Star-Lack, and A. S. Wang, "Characterization and potential applications of a dual-layer flat-panel detector," *Medical Physics*, vol. 47, no. 8, pp. 3332–3343, 2020. [Online]. Available: https://aapm.onlinelibrary.wiley.com/doi/abs/10.1002/mp.14211

[101] T. Flohr, M. Petersilka, A. Henning, S. Ulzheimer, J. Ferda, and B. Schmidt, "Photon-counting ct review," *Physica Medica*, vol. 79, p. 126–136, Nov 2020. [Online]. Available: http://dx.doi.org/10.1016/j.ejmp.2020.10.030

[102] E. Roessl and R. Proksa, "K-edge imaging in x-ray computed tomography using multi-bin photon counting detectors," *Physics in Medicine and Biology*, vol. 52, no. 15, pp. 4679–4696, 2007.

[103] R. E. Alvarez, "Estimator for photon counting energy selective x-ray imaging with multibin pulse height analysis," *Medical physics*, vol. 38, no. 5, pp. 2324–2334, 2011.

[104] K. Mechlem, S. Ehn, T. Sellerer, E. Braig, D. Münzel, F. Pfeiffer, and P. B. Noël, "Joint statistical iterative material image reconstruction for spectral computed tomography using a semi-empirical forward model," *IEEE transactions on medical imaging*, vol. 37, no. 1, pp. 68–80, 2017.

[105] T. Fukui, A. Katsumata, K. Ogawa, and S. Fujiwara, "Usefulness of an energy-binned photon-counting x-ray detector for dental panoramic radiographs," in *Medical Imaging 2015: Physics of Medical Imaging*, vol. 9412. International Society for Optics and Photonics, 2015, p. 94125O.

[106] R. Langlais, A. Katsumata, S. Naidoo, K. Ogawa, T. Fukui, S. Shimoda, and K. Kobayashi, "The cadmium telluride photon counting sensor in panoramic radiology: gray value separation and its potential application for bone density evaluation," *Oral Surgery, Oral Medicine, Oral Pathology Oral Radiology*, vol. 120, no. 5, pp. 636–643, 2015.

[107] H. N. Cardinal and A. Fenster, "An accurate method for direct dual-energy calibration and decomposition," *Medical physics*, vol. 17, no. 3, pp. 327–341, 1990.

[108] M. Noujeim, T. Prihoda, W. D. McDavid, K. Ogawa, K. Seki, T. Okano, T. Sue, and R. P. Langlais, "Pre-clinical evaluation of a new dental panoramic radiographic system based on tomosynthesis method," *Dentomaxillofacial Radiology*, vol. 40, no. 1, pp. 42–46, 2011, pMID: 21159914. [Online]. Available: https://doi.org/10.1259/dmfr/73312141

[109] O. Gormez and H. H. Yilmaz, "Image post-processing in dental practice," *European journal of dentistry*, vol. 3, no. 4, pp. 343–347, 2009.

[110] G. Hodolli, S. Kadiri, G. Nafezi, M. Bahtijari, and N. Syla, "Diagnostic reference levels at intraoral and dental panoramic examinations," *International Journal of Radiation Research*, vol. 17, no. 1, pp. 147–150, 2019.

[111] A. S. Wang and N. J. Pelc, "Sufficient statistics as a generalization of binning in spectral x-ray imaging," *IEEE Transactions on Medical Imaging*, vol. 30, no. 1, pp. 84–93, 2011.

[112] V. Somerkivi, T. Sellerer, T. Pantsar, H. Lohman, and F. Pfeiffer, "Spectral photon counting for panoramic dental imaging," *Biomedical Physics & Engineering Express*, vol. 9, no. 3, p. 035017, mar 2023. [Online]. Available: https://dx.doi.org/10.1088/2057-1976/acc339

[113] T. Sellerer, S. Ehn, K. Mechlem, M. Duda, M. Epple, P. B. Noël, and F. Pfeiffer, "Quantitative dual-energy micro-ct with a photon-counting detector for material science and non-destructive testing," *PloS one*, vol. 14, no. 7, pp. 1–18, 2019.

[114] A. Wang, A. Maslowski, P. Messmer, M. Lehmann, A. Strzelecki, E. Yu, P. Paysan, M. Brehm, P. Munro, J. Star-Lack, and D. Seghers, "Acuros cts: A fast, linear boltzmann transport equation solver for computed tomography scatter – part ii: System modeling, scatter correction, and optimization," *Medical Physics*, vol. 45, no. 5, pp. 1914–1925, 2018. [Online]. Available: https://aapm.onlinelibrary.wiley.com/doi/abs/10.1002/mp.12849

[115] S. Perschbacher, "Interpretation of panoramic radiographs," *Australian dental journal*, vol. 57, pp. 40–45, 2012.

[116] M. Bae, J.-W. Park, and N. Kim, "Semi-automatic and robust determination of dental arch form in dental cone-beam ct with b-spline approximation," *Computer Methods and Programs in Biomedicine*, vol. 172, pp. 95–101, 2019. [Online]. Available: https://www.sciencedirect.com/science/article/pii/S0169260718317930

[117] T. Luo, C. Shi, X. Zhao, Y. Zhao, and J. Xu, "Automatic synthesis of panoramic radiographs from dental cone beam computed tomography data," *PLOS ONE*, vol. 11, no. 6, pp. 1–20, 06 2016. [Online]. Available: https://doi.org/10.1371/journal.pone.0156976

[118] T. K. Papakosta, A. D. Savva, T. L. Economopoulos, G. K. Matsopoulos, and H. Gröhndal, "An automatic panoramic image reconstruction scheme from dental computed tomography images," *Dentomaxillofacial Radiology*, vol. 46, no. 4, p. 20160225, 2017.

[119] Z. Yun, S. Yang, E. Huang, L. Zhao, W. Yang, and Q. Feng, "Automatic reconstruction method for high-contrast panoramic image from dental cone-beam ct data," *Computer Methods and Programs in Biomedicine*, vol. 175, pp. 205–214, 2019. [Online]. Available: https://www.sciencedirect.com/science/article/pii/S0169260719303384

[120] C. Altunbas, Y. Park, Z. Yu, and A. Gopal, "A unified scatter rejection and correction method for cone beam computed tomography," *Medical physics*, vol. 48, no. 3, pp. 1211–1225, 2021.

[121] O. Cuadros Linares, J. Bianchi, D. Raveli, J. Batista Neto, and B. Hamann, "Mandible and skull segmentation in cone beam computed tomography using super-voxels and graph clustering," *The Visual Computer*, vol. 35, pp. 1461–1474, 2019.

[122] L. R. Emmendorfer, "A conservative sharpening filter for interpolated images," in *2020 33rd SIBGRAPI Conference on Graphics, Patterns and Images (SIBGRAPI)*. IEEE, 2020, pp. 93–100.

[123] A. Malecki, G. Potdevin, and F. Pfeiffer, "Quantitative wave-optical numerical analysis of the dark-field signal in grating-based x-ray interferometry," *Europhysics Letters*, vol. 99, no. 4, p. 48001, 2012.

[124] P. Hasgall, F. Di Gennaro, C. Baumgartner, E. Neufeld, B. Lloyd, M. Gosselin, D. Payne, A. Klingenböck, and N. Kuster, "It'is database for thermal and electromagnetic parameters of biological tissues," Foundation for Research on Information Technologies in Society, Tech. Rep. Version 4.0, 2018.

[125] A. Laugerette, B. J. Schwaiger, K. Brown, L. C. Frerking, F. K. Kopp, K. Mei, T. Sellerer, J. Kirschke, T. Baum, A. S. Gersing *et al.*, "Dxa-equivalent quantification of bone mineral density using dual-layer spectral ct scout scans," *European Radiology*, vol. 29, pp. 4624–4634, 2019.

[126] J. T. Lin and J. M. Lane, "Osteoporosis: a review." *Clinical Orthopaedics and Related Research (1976-2007)*, vol. 425, pp. 126–134, 2004.

[127] B. L. Riggs and L. Melton Iii, "The worldwide problem of osteoporosis: insights afforded by epidemiology," *Bone*, vol. 17, no. 5, pp. S505–S511, 1995.

[128] E. Lewiecki, B. Chastek, K. Sundquist, S. Williams, R. Weiss, Y. Wang, L. Fitzpatrick, and J. Curtis, "Osteoporotic fracture trends in a population of us managed care enrollees from 2007 to 2017," *Osteoporosis International*, vol. 31, pp. 1299–1304, 2020.

[129] G. Giro, L. Chambrone, A. Goldstein, J. A. Rodrigues, E. Zenóbio, M. Feres, L. C. Figueiredo, A. Cassoni, and J. A. Shibli, "Impact of osteoporosis in dental implants: a systematic review," *World journal of orthopedics*, vol. 6, no. 2, p. 311, 2015.

[130] N. Von Wowern, B. Klausen, and G. Kollerup, "Osteoporosis: a risk factor in periodontal disease," *Journal of periodontology*, vol. 65, no. 12, pp. 1134–1138, 1994.

[131] N. von Wowern, "General and oral aspects of osteoporosis: a review," *Clin Oral Investig*, vol. 5, no. 2, pp. 71–82, Jun. 2001.

[132] G. M. Blake and I. Fogelman, "Technical principles of dual energy x-ray absorptiometry," *Seminars in nuclear medicine*, vol. 27, no. 3, pp. 210–228, 1997.

[133] K. Horner, H. Devlin, C. Alsop, I. Hodgkinson, and J. Adams, "Mandibular bone mineral density as a predictor of skeletal osteoporosis," *The British journal of radiology*, vol. 69, no. 827, pp. 1019–1025, 1996.

[134] E. Calciolari, N. Donos, J.-C. Park, A. Petrie, and N. Mardas, "A systematic review on the correlation between skeletal and jawbone mineral density in osteoporotic subjects," *Clinical Oral Implants Research*, vol. 27, no. 4, pp. 433–442, 2016.

[135] M. Bozic and N. Ihan Hren, "Osteoporosis and mandibles," *Dentomaxillofacial Radiology*, vol. 35, no. 3, pp. 178–184, 2006.

[136] R. Fahrig, D. A. Jaffray, I. Sechopoulos, and J. Webster Stayman, "Flat-panel conebeam ct in the clinic: history and current state," *Journal of Medical Imaging*, vol. 8, no. 5, pp. 052 115–052 115, 2021.

[137] R. H. N. Rondon, Y. C. L. Pereira, and G. C. do Nascimento, "Common positioning errors in panoramic radiography: A review," *Imaging science in dentistry*, vol. 44, no. 1, pp. 1–6, 2014.

[138] F. Kaviani, M. Johari, and F. Esmaeili, "Evaluation of common errors of panoramic radiographs in tabriz faculty of dentistry," *Journal of dental research, dental clinics, dental prospects*, vol. 2, no. 3, p. 99, 2008.

[139] M. Dhillon, S. M. Raju, S. Verma, D. Tomar, R. S. Mohan, M. Lakhanpal, and B. Krishnamoorthy, "Positioning errors and quality assessment in panoramic radiography," *Imaging science in dentistry*, vol. 42, no. 4, pp. 207–212, 2012.

[140] R. Gradl, I. Zanette, M. Ruiz-Yaniz, M. Dierolf, A. Rack, P. Zaslansky, and F. Pfeiffer, "Mass density measurement of mineralized tissue with grating-based x-ray phase tomography," *PloS one*, vol. 11, no. 12, p. e0167797, 2016.

[141] V. Somerkivi, T. Sellerer, D. Berthe, Y. Haemisch, T. Pantsar, H. Lohman, T. Kaasalainen, and F. Pfeiffer, "Mandible bone mineral density estimation using spectral panoramic x-ray imaging," *Imaging science in dentistry*, vol. 55, no. 1, p. 56, 2025.

[142] A. H. Abdi, S. Kasaei, and M. Mehdizadeh, "Automatic segmentation of mandible in panoramic x-ray," *Journal of Medical Imaging*, vol. 2, no. 4, pp. 044 003–044 003, 2015.

[143] K. Mechlem, S. Ehn, T. Sellerer, E. Braig, D. Münzel, F. Pfeiffer, and P. B. Noël, "Joint statistical iterative material image reconstruction for spectral computed tomography using a semi-empirical forward model," *IEEE Transactions on Medical Imaging*, vol. 37, no. 1, pp. 68–80, 2018.

[144] H. P. Dimai, "Use of dual-energy x-ray absorptiometry (dxa) for diagnosis and fracture risk assessment; who-criteria, t-and z-score, and reference databases," *Bone*, vol. 104, pp. 39–43, 2017.

[145] E. Benavides, H. F. Rios, S. D. Ganz, C. H. An, R. Resnik, G. T. Reardon, and et al., "Use of cone beam computed tomography in implant dentistry: the international congress of oral implantologists consensus report," *Implant Dent*, vol. 21, pp. 78–86, 2012.

[146] W. De Vos, J. Casselman, and G. R. Swennen, "Cone-beam computerized tomography (cbct) imaging of the oral and maxillofacial region: a systematic review of the literature," *Int J Oral Maxillofac Surg*, vol. 38, pp. 609–25, 2009.

[147] M. Cassetta, L. V. Stefanelli, A. Pacifici, L. Pacifici, and E. Barbato, "How accurate is cbct in measuring bone density? a comparative cbct - ct in vitro study," *Clin Implant Dent Relat Res*, vol. 16, pp. 471–8, 2014.

[148] R. Jacobs, B. Salmon, M. Codari, B. Hassan, and M. M. Bornstein, "Cone beam computed tomography in implant dentistry: recommendations for clinical use," *BMC Oral Health*, vol. 18, p. 88, 2018.

[149] R. Pauwels, K. Araki, J. H. Siewerdsen, and S. S. Thongvigitmanee, "Technical aspects of dental cbct: state of the art," *Dentomaxillofac Radiol*, vol. 44, p. 20140224, 2015.

[150] R. Pauwels, P. Pittayapat, P. Sinpitaksakul, and S. Panmekiate, "Scatter-to-primary ratio in dentomaxillofacial cone-beam ct: effect of field of view and beam energy," *Dentomaxillofac Radiol*, vol. 50, p. 20200597, 2021.

[151] C. Altunbas, "Image corrections for scattered radiation," in *Cone Beam Computed Tomography*, C. C. Shaw, Ed. Boca Raton, FL: CRC Press, 2014, pp. 129–147.

[152] E. P. Ruhrnschopf and K. Klingenbeck, "A general framework and review of scatter correction methods in cone beam ct. part 2: scatter estimation approaches," *Med Phys*, vol. 38, pp. 5186–5199, 2011.

[153] X. Liu, C. C. Shaw, T. Wang, L. Chen, M. C. Altunbas, and S. C. Kappadath, "An accurate scatter measurement and correction technique for cone beam breast ct imaging using scanning sampled measurement (ssm) technique," *Proc SPIE Int Soc Opt Eng*, vol. 6142, pp. 614 234–7, 2006.

[154] M. Sun and J. M. Star-Lack, "Improved scatter correction using adaptive scatter kernel superposition," *Phys Med Biol*, vol. 55, pp. 6695–720, 2010.

[155] E. P. Rührnschopf and K. Klingenbeck, "A general framework and review of scatter correction methods in x-ray cone-beam computerized tomography. part 1: scatter compensation approaches," *Med Phys*, vol. 38, pp. 4296–4311, 2011.

[156] J. H. Siewerdsen, D. J. Moseley, B. Bakhtiar, S. Richard, and D. A. Jaffray, "The influence of antiscatter grids on soft-tissue detectability in cone-beam computed tomography with flat-panel detectors," *Med Phys*, vol. 31, pp. 3506–3520, 2004.

[157] M. Bertram, J. Wiegert, and G. Rose, "Scatter correction for cone-beam computed tomography using simulated object models," in *Proceedings of Medical Imaging 2006: Physics of Medical Imaging*. San Diego, USA: SPIE, 2006, p. 61421C.

[158] D. C. Hansen, G. Landry, F. Kamp, M. Li, C. Belka, K. Parodi *et al.*, "Scatternet: a convolutional neural network for cone-beam ct intensity correction," *Med Phys*, vol. 45, pp. 4916–4926, 2018.

[159] M. C. Altunbas, C. C. Shaw, L. Chen, C. Lai, X. Liu, T. Han *et al.*, "A post-reconstruction method to correct cupping artifacts in cone beam breast computed tomography," *Med Phys*, vol. 34, pp. 3109–3118, 2007.

[160] C. Altunbas, B. Kavanagh, T. Alexeev, and M. Miften, "Transmission characteristics of a two-dimensional antiscatter grid prototype for cbct," *Med Phys*, vol. 44, pp. 3952–64, 2017.

[161] C. Altunbas, T. Alexeev, M. Miften, and B. Kavanagh, "Effect of grid geometry on the transmission properties of 2 d grids for flat detectors in cbct," *Phys Med Biol*, vol. 64, p. 225006, 2019.

[162] T. Alexeev, B. Kavanagh, M. Miften, and C. Altunbas, "Two-dimensional antiscatter grid: a novel scatter rejection device for cone-beam computed tomography," *Med Phys*, vol. 45, pp. 529–34, 2018.

[163] Y. Park, T. Alexeev, B. Miller, M. Miften, and C. Altunbas, "Evaluation of scatter rejection and correction performance of 2d antiscatter grids in cone beam computed tomography," *Med Phys*, vol. 48, pp. 1846–58, 2021.

[164] F. Bayat, D. Ruan, M. Miften, and C. Altunbas, "A quantitative cbct pipeline based on 2d antiscatter grid and grid-based scatter sampling for image-guided radiation therapy," *Med Phys*, vol. 50, pp. 7980–95, 2023.

[165] B. Li, V. Somerkivi, F. Bayat, C. Huynh, and C. Altunbas, "Effect of a prototype 2-dimensional antiscatter grid on image quality obtained with a dental cone-beam computed tomography scanner," *Imaging Science in Dentistry*, vol. 55, no. 1, p. 37, 2025.

[166] Z. Yu, Y. Park, and C. Altunbas, "Simultaneous scatter rejection and correction method using 2d antiscatter grids for cbct," in *Proc SPIE Int Soc Opt Eng*, vol. 11312, 2020, p. 113122W.

[167] C. Altunbas, Y. Park, Z. Yu, and A. Gopal, "A unified scatter rejection and correction method for cone beam computed tomography," *Med Phys*, vol. 48, pp. 1211–1225, 2020.

[168] J. Hsieh, *Computed tomography: principles, design, artifacts, and recent advances.* Bellingham, WA: SPIE Press, 2009.

[169] C. C. Shaw, *Cone beam computed tomography.* Boca Raton, FL: CRC Press, 2014.

[170] F. Bayat, M. E. Eldib, B. Kavanagh, M. Miften, and C. Altunbas, "Concurrent kilovoltage cbct imaging and megavoltage beam delivery: suppression of cross-scatter with 2d antiscatter grids and gridbased scatter sampling," *Phys Med Biol*, vol. 67, p. 165005, 2022.

[171] V. Lolli, M. Pezzullo, I. Delpierre, and N. Sadeghi, "Mdct imaging of traumatic brain injury," *Br J Radiol*, vol. 89, p. 20150849, 2016.

[172] K. A. Fetterly and B. A. Schueler, "Physical evaluation of prototype high-performance antiscatter grids: potential for improved digital radiographic image quality," *Phys Med Biol*, vol. 54, pp. N37–42, 2009.

[173] D. Berthe, A. Kolb, A. Rabi, T. Sellerer, V. Somerkivi, G. C. Feuerriegel, A. P. Sauter, F. Meurer, Y. Hämisch, T. Pantsar *et al.*, "Evaluation of spectral x-ray imaging for panoramic dental images based on a simulation framework," *Journal of Imaging Informatics in Medicine*, vol. 37, no. 2, pp. 892–898, 2024.